Velocity and anisotropy structure of the Icelandic crust

An ambient seismic noise analysis

Omry Volk

Department of Earth Sciences
University of Cambridge

This dissertation is submitted for the degree of
Doctor of Philosophy

Fitzwilliam College April 2021

Declaration

I hereby declare that except where specific reference is made to the work of others, the contents of this dissertation are original and have not been submitted in whole or in part for consideration for any other degree or qualification in this, or any other university. This dissertation is my own work and contains nothing which is the outcome of work done in collaboration with others, except as specified in the text and Acknowledgements. This dissertation contains fewer than 65,000 words including appendices, bibliography, footnotes, tables and equations and has fewer than 150 figures.

Omry Volk
April 2021

Acknowledgements

First and foremost, I would like to thank my supervisors, Nick Rawlinson and Bob White, for their guidance and support. They have been highly generous with their time and energy and were always there when I needed them. Nick, I especially thank you for allowing me to pursue my own path, your truly endless patience and support, and last but not least, for the world class fieldwork cooking. Bob, I especially thank you for giving me the opportunity to work in Iceland with which I fell in love, your endless excitement, and your ever wise directions along the way. I couldn't have asked for better supervisors.

I would also like to thank Simone Pilia who acted as unofficial supervisor during my first months and brought me in on the actual work. Keith Priestley and James Jackson, my academic friends, have provided key advice throughout my PhD which I greatly benefited from. I also want to thank John Maclennan for his thoughtful contribution to my work. My PhD would have not been the same without the student and postdoc community at Bullard so thanks to all of you. A special thanks to Conor Bacon, with whom I shared much of my time on fieldwork, for always being the first to help and for always having the best tunes.

Fieldwork would have never been possible without our collaborators overseas. I thank Sveinbjörn Steinthórsson for his help in the Icelandic highlands. A special thanks to Bryndís Brandsdóttir, whose help and contribution are hard to overstate and everything she has done to make us feel at home. I also greatly thank Felix Tongkul and Epiphanius Lasimbang for their help with fieldwork in Borneo.

A final thank you to the Trinity-Henry Barlow Charitable Trust which has generously provided my scholarship, making it possible for me to come to Cambridge.

Publications

Journal publications related to this dissertation

Volk, O., White, R.S., Pilia, S., Green, R.G., Maclennan, J. and Rawlinson, N. (2021) Oceanic crustal flow in Iceland observed using seismic anisotropy. *Nature Geoscience*, 14(3), pp.168-173.

Volk, O., White, R. S., Greenfield, T., Winder, T., Bacon, C. Rawlinson, N. (2020) Crack-induced seismic anisotropy dominates shallow crustal velocity structure beneath Askja volcano, Iceland: Implications for body and surface wave models. *Under revision - Geophysical Journal International*

Other journal publications by the author of this dissertation

Finzi, Y., Ganz, N., Dor, O., Davis, M., **Volk, O.**, Langer, S., Arromsmith, R. Tsesarsky, M. (2020) Stability analysis of fragile rock pillars and insights on fault activity in the Negev, Israel. *Journal of Geophysical Research: Solid Earth, 125, https://doi.org/10.1029/2019JB019269*

Shani-Kadmiel, S., **Volk, O.**, Gvirtzman, Z. and Tsesarsky, M., (2020). Ground motion amplification atop the complex sedimentary basin of Haifa Bay (Israel). *Bulletin of Earthquake Engineering, 18(3), pp.821-836.*

Volk, O., Shani-Kadmiel, S., Gvirtzman, Z. and Tsesarsky, M., (2017). 3D Effects of sedimentary wedges and subsurface canyons: Ground-motion amplification in the Israeli coastal plain. *Bulletin of the Seismological Society of America, 107(3), pp.1324-1335.*

Abstract

Measuring the travel times of seismic waves is one of the most important tools for uncovering Earth's structure and dynamics. In recent years, the discovery that surface wave dispersion could be estimated from ambient noise has introduced new possibilities into the field of seismic imaging, such as performing passive source tomography in regions where it was not previously possible with a dense azimuthal ray path coverage. In this work, I leverage the new possibilities introduced by this method to investigate the crust in Iceland in a number of ways, including tomographic imaging as well as azimuthal and radial anisotropy analyses in both the lower and upper crust.

Understanding accretion and deformation processes at mid-ocean ridges is crucial because they control the resulting oceanic crustal structure, which covers two-thirds of the Earth's surface. Iceland, which is uplifted by a convective mantle plume and has an active spreading ridge system exposed above sea level, offers a unique opportunity for studying this phenomenon.

I first use a dataset of Love and Rayleigh wave dispersion measurements with dense azimuthal coverage to constrain seismic anisotropy in the Icelandic crust. I show that seismic anisotropy in the lower crust is controlled by crystal preferred orientation, providing a direct observation of lower crustal flow. Furthermore, since shear is needed to align the crystals, our result reveals that crustal flow cannot be a simple translation of mass and requires internal deformation. This finding has important implications for how thick, hot oceanic crust, as found in volcanic rifted margins and near plume-ridge interactions, can accrete and deform.

Despite the growing use of ambient noise in measuring crustal properties, extensive comparisons between ambient noise results and those obtained from local earthquakes remain elusive. To address this, I measure Love and Rayleigh group velocity using ambient noise recorded around Askja, a large active volcano in central Iceland, explore its velocity structure and anisotropy and compare my findings to those from local earthquake studies. I show that crack properties estimated using surface wave anisotropy strongly correlate with local shear wave splitting and outcrop mapping, indicating the method is highly effective for such analyses. Next, I show that V_{SV} models derived from Rayleigh waves can be significantly faster than V_S extracted from body waves, which has important implications for jointly exploiting these two classes of data. Furthermore, 3D V_{SV} and V_{SH} models constrained by the data through a two-step inversion procedure resolve a shallow slow anomaly consistent with a magma chamber predicted by geodetic studies, but not imaged by local earthquake body wave tomography.

I then measure Love and Rayleigh phase velocities from ambient noise in Iceland in the period range 7 - 16 s from more than 3000 station pairs. This involves the development and use of an automatic method for extracting phase velocities from noise cross-correlation functions (NCF). The phase travel times are then inverted for phase velocity maps. I present the first Love phase velocity maps of Iceland and show that like Rayleigh phase velocities, Love phase velocities display slow anomalies along the rift zones with the lowest velocities in the neighbourhood large volcanic centres, which I attribute to the presence of partial melt.

Table of contents

List of figures

Chapter 1

Introduction

1.1 Overview and thesis structure

Chapter 1 is an introduction chapter detailing the main motivations behind the project and a brief geologic/tectonic background about Iceland and imaging using ambient noise. Chapter 2 gives an overview of the methods used throughout this work. Chapters 3, 4 and 5 are each self-contained and additional relevant background and methods information is contained within. The independent Chapters 3 - 5 are ordered by importance, as viewed by the author (most impactful first).

In chapter 3 I calculate azimuthal and radial anisotropy from period dependent Love and Rayleigh phase travel times in the lower crust. The lower crust displays positive radial anisotropy that changes with azimuth and is best explained by crystal preferred orientation, thus providing a direct observation of oceanic crustal flow ,which to the best of my knowledge has not been observed elsewhere.

In chapter 4 I calculate azimuthal and radial anisotropy from Love and Rayleigh group travel times around Askja, a large volcano in Iceland, and display a comparison between ambient noise results and those from many other methods including outcrop mapping, shear wave splitting and local earthquake tomography. I show that (1) measuring azimuthal and radial anisotropy using ambient noise is highly effective for estimating crack properties; (2) 1D V_{SV} models from ambient noise, which are commonly used for earthquake location, may underestimate velocity and lead to error in depth estimates; and (3) ambient noise tomography reveals a slow circular anomaly below the caldera, consistent with a magaa chamber modelled from InSAR data at a depth of 2 - 3 km .

In Chapter 5 I develop a method for automatic picking of phase velocity from ambient noise cross correlations and use it to pick more than 2000 Love and Rayleigh wave dispersion curves in Iceland. I then use the dataset for 2D phase velocity tomography, including the first Love phase velocity map of Iceland, and compare my results to previous works. I show that like both Rayleigh phase velocity maps, Love phase velocity maps display slow anomalies along the rift zones, with large volcanic centres exhibiting the slowest anomalies that are recovered.

1.2 Iceland

1.2.1 Motivation

Approximately two thirds of the Earth's surface is covered by oceanic crust which is formed at mid-ocean spreading ridges. Once oceanic crust has formed at the ridge, it gradually moves away from it as a result of plate motion and in most cases undergoes very little further change. Therefore, the thickness, structure and composition of much of Earth's crust is a result of spreading ridge processes. This makes studying these ridges highly important for our understanding of Earth's structure and plate tectonic processes. However, when compared to continental plate boundaries, active spreading ridges are normally highly inaccessible due to their remoteness and deep water setting. As a consequnece, the installation and recovery of seismic instruments is very difficult, resulting in poor data coverage compared to the continental plate boundaries. Additionally, while valuable data can be collected using ocean bottom seismometers, it is often of lower quality when comapred to data from onshore seismometers (Duennebier and Sutton, 1995; Mangano et al., 2011). This is exacerbated by the fact that under water instruments are usually deployed for relatively short periods of time due to limited battery life. Iceland, which sits atop the mid-Atlantic Ridge is one of the only places in the entire 60,000 km-long global spreading-ridge system (Fig 1.1) where an active mature (i.e. not in the early stages of breakup such as in East Africa) spreading ridge is exposed above sea level. Iceland therefore represents a unique opportunity for studying a spreading ridge and oceanic crustal formation using land based methods.

1.2.2 Iceland - Tectonic setting

The island of Iceland is the result of hotspot volcanism and lies at the centre of a large 2000 km wide topographic bulge (Fig 1.2). This hotspot volcanism and bulge are commonly attributed to the presence of a narrow circular convective plume (Morgan, 1971) in the underlying mantle. This hypothesis is supported by a geoid anomaly (White and McKenzie,

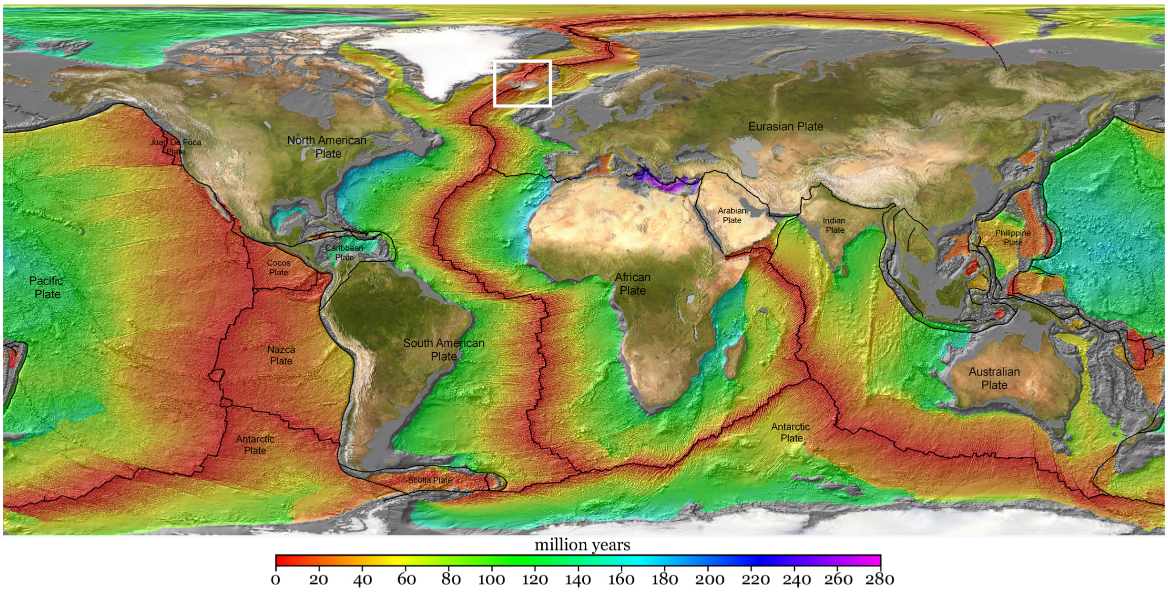

Fig. 1.1 A map of ocean sea floor age and MORs (from Müller et al. (2008)) with Iceland's location denotaed by a white box. Two third of the Earth's crust is created at MORs and Iceland is one of the only places in the world where a MOR is easily accessible. Source: NOAA

1989), an increased crustal thickness of up to 40 km (Darbyshire et al., 1998) compared to typical oceanic crust of ~7 km, and anomalies in the geochemistry of erupted volcanic products (White et al., 1992; Shorttle and Maclennan, 2011) along the ridge. Furthermore, multiple tomographic models of the mantle beneath Iceland display a cylindrical low-velocity anomaly in the upper mantle (Fig 1.4a)(Wolfe et al., 1997; Foulger et al., 2001; Allen et al., 2002). The slow seismic velocity is most likely due to higher temperature and therefore the anomaly is typically interpreted as a hot upwelling conduit. Until recently, some debate existed about whether the upwelling originates from the lower or upper mantle (Foulger et al., 2001). Furthermore, the inherent difficulty of imaging a narrow plume at depth with most receivers being directly above it, as in Iceland, generated a debate over whether it is possible to answer this question using existing seismic data (Keller et al., 2000; Wolfe, 2002). Today it is largely accepted that a narrow convective plume rooted in the lower mantle exists under Iceland, supported by evidence from interference of shear-wave phases transmitted through, and refracted at, the core-mantle boundary (Helmberger et al., 1998), and whole-mantle seismic imaging (French and Romanowicz, 2015). The location of the centre of the slow anomaly is also directly below the location of maximum crustal thickness (Darbyshire et al., 2000), and where volcanic activity is most intense under the north-western part of Vatnajökull icecap (Fig 1.4b).

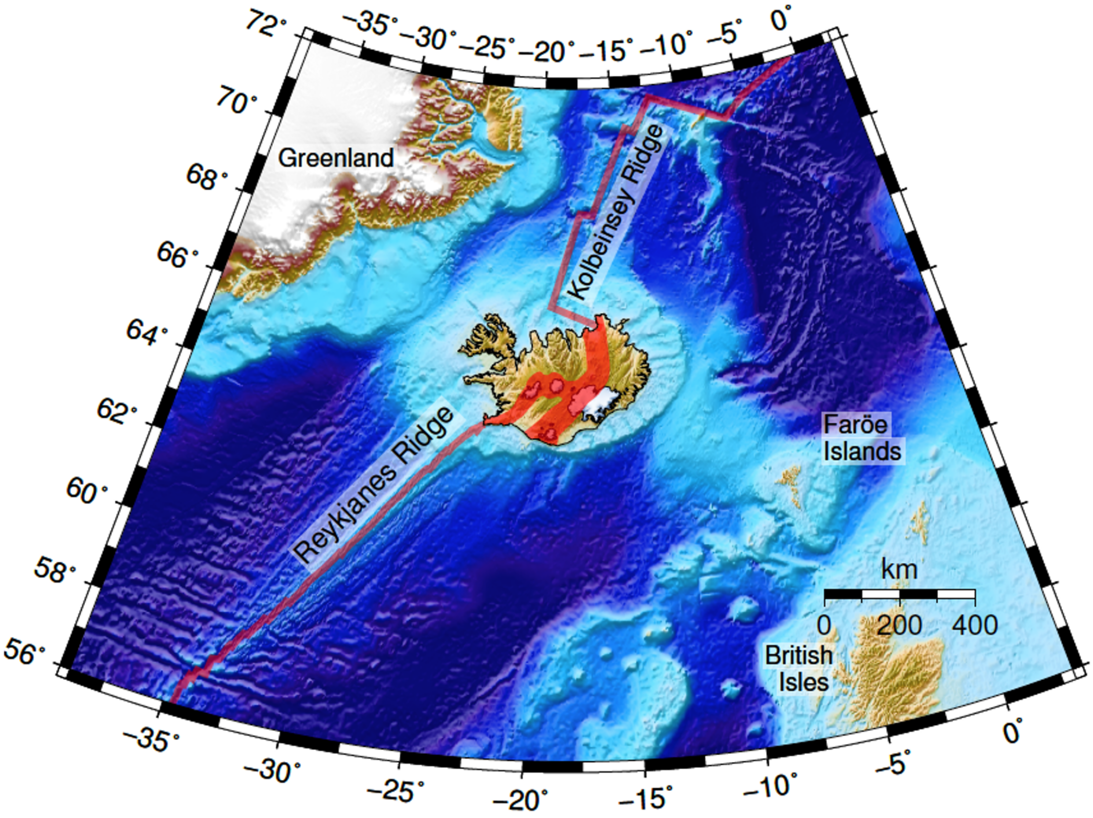

Fig. 1.2 The bathymetry in the North Atlantic Ocean around Iceland. It can be seen that Iceland lies in the centre of a large 2000 km wide topographic bulge. Reproduced from Green (2016)

The crustal structure of Iceland is not a simple Mid Ocean Ridge (MOR) structure. The on-land section of the Mid-Atlantic MOR in Iceland can be broadly divided into three separate branches. These branches are commonly known as the western, eastern and northern volcanic zones (WVZ, EVZ and NVZ, Fig 1.4b). The reason for the parallel section of the WVZ and EVZ is attributed to a ridge jump from the WVZ to the EVZ (Hardarson et al., 1997) currently in progress. Furthermore, unlike normal oceanic crust which displays a typical thickness of 5-7 km, the crust in Iceland displays large thickness variability from less than 20 km in the active rift zones to 40 km under Vatnajökull icecap. The large variability is attributed to a series of successive rift jumps and increased melting above the centre of the plume. The full spreading rate of the crust in Iceland is 18.5mm/y (DeMets et al., 2010) and the extension direction has an azimuth of 106°.

More detailed background on Iceland's crustal deformation and composition is provided in chapter 3. Further information on previous seismic imaging studies in Iceland is provided in chapter 5, where new tomographic images of the Icelandic crust are presented.

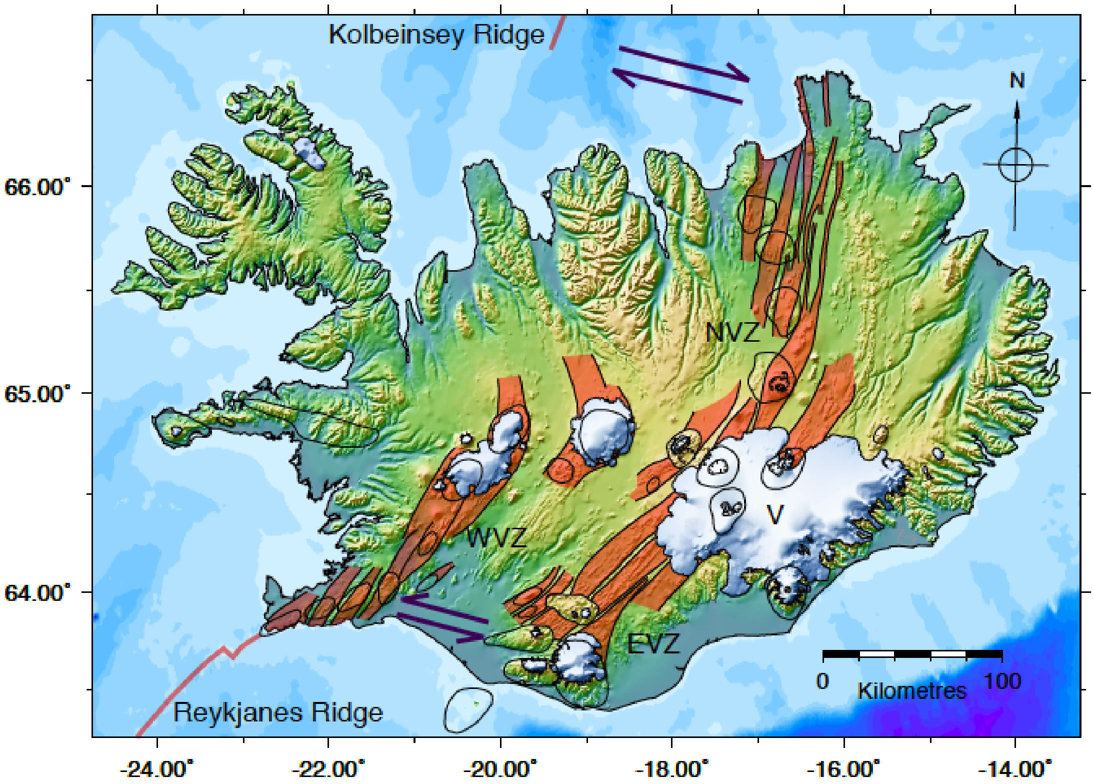

Fig. 1.3 Topography and surface features of Iceland. The location of the NVZ, EVZ and WVZ is is shown together with fissure swarms, denoted in orange, and central volcanoes, denoted using black lines. Icecaps are shown in white and Vatnajökull icecap is marked with V. Reproduced from Donaldson (2019).

1.3 Surface waves and ambient noise

1.3.1 Motivation

Measuring the travel times of seismic waves propagating through the Earth has long been a key tool for investigating its structure and dynamics. This can be done using body waves which travel through the interior of the Earth or by using surface waves which travel along the surface of the Earth. While surface waves are limited to relatively shallow depths compared to body waves, they present other advantages. First, surface waves are dispersive, meaning different periods have different depth sensitivity and therefore travel at different velocities. While this makes the data analyses more involved, it also has the advantage of simultaneously sampling across a range of depths along the ray-path, which provides valuable information. Second, unlike body waves, which change their incident angle along the path, surface waves travel approximately parallel to the surface, making them an ideal tool for exploring

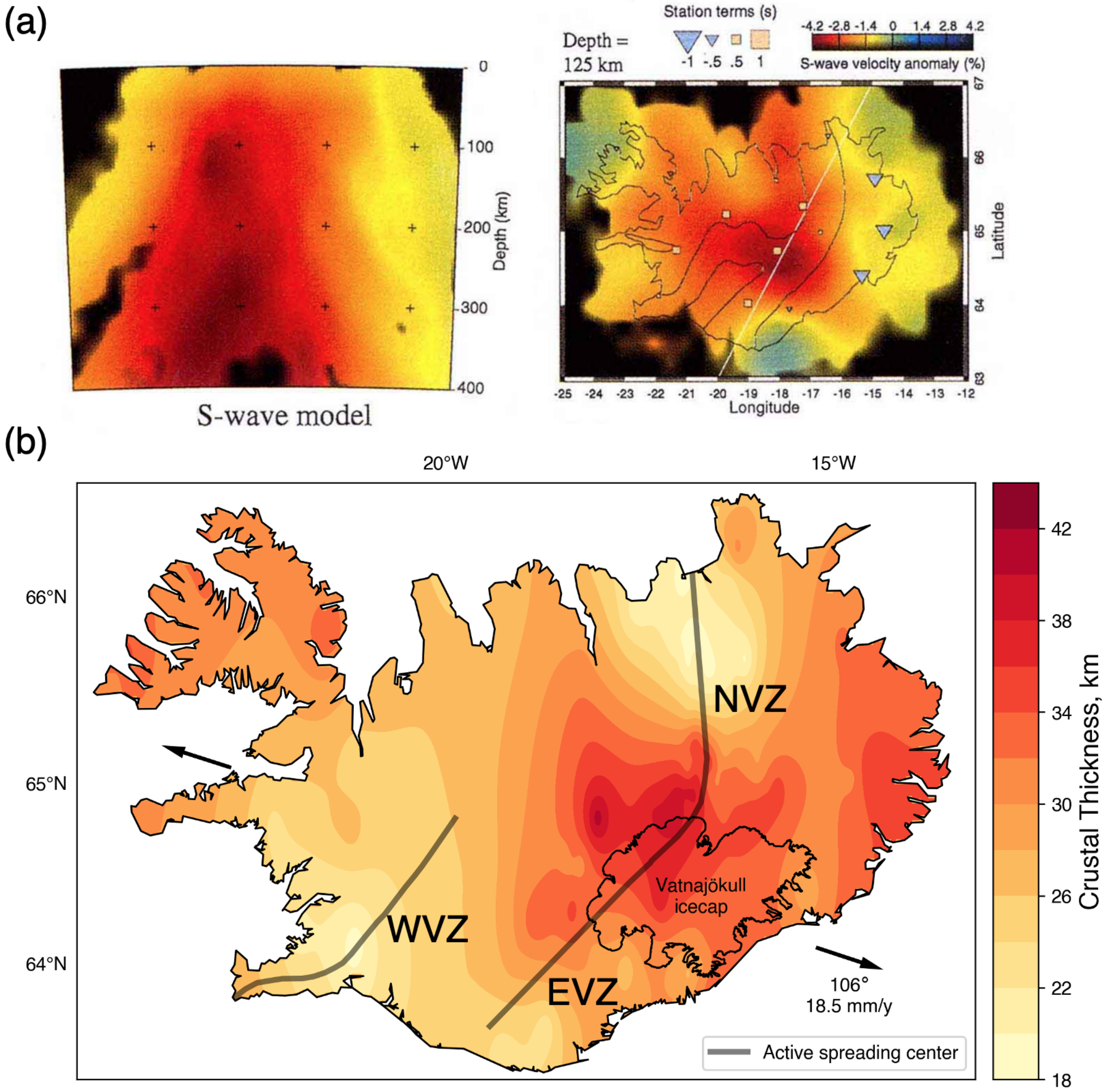

Fig. 1.4 (a) Body waves velocity model under Iceland from Wolfe et al. (1997) reveals a narrow cylindrical slow anomaly in the mantle. (b) Crustal thickness based on Jenkins et al. (2016) is shown as colored contours. Grey lines denote the location of active spreading centres. Thin black line shows the outline of Vatnajökull icecap roughly corresponding to the estimated location of the plume head. Black arrows indicate the spreading direction of 106° with a full spreading rate of 18.5 mm/yr.

azimuthal anisotropy, which is key to studying dynamic process within the Earth. Third, there are two main types of surface waves: Love and Rayleigh (Fig. 1.5). Rayleigh waves have a longitudinal (also referred to as radial) and vertical motion while Love waves have a transverse motion and as such are polarized in the vertical and horizontal planes respectively. Therefore, Rayleigh waves are mostly sensitive to the vertical shear velocity (V_{SV}) and Love waves to the horizontal shear velocity (V_{SH}). Measuring these two properties independently can provide valuable insight into velocity structure and the difference between the two can be used to obtain radial anisotropy.

Traditionally, achieving these measurements depended on the existence of a defined seismic source, usually an earthquake or more rarely an active source such as an explosion. In recent years, the discovery that surface wave velocities could be estimated from ambient noise has introduced new possibilities to the field since measurements are no longer dependent on the size, number and spatial distribution of sources. This presents several major advantages:

- Local scale tomography ($\sim$10 - 100 km) previously required a wealth of local seismicity. Since ambient noise is independent of local seismicity, this means that seismic velocities can now be measured almost anywhere on earth where a reasonable level of ambient noise is present.
- Since earthquakes are mostly concentrated around plate boundaries and not randomly distributed in space, it is difficult in many regions of the world to achieve a dense azimuthal coverage of ray-paths. When using ambient noise, it is much easier to achieve this since the available azimuths mostly depend on the network setup.
- With surface waves, different periods are sensitive to different depths. Therefore, the measured period range limits which depths can be imaged. The recoverable period range from ambient noise is usually shorter ($\sim$1 - 40 s)(Bensen et al., 2007) than that of earthquakes ($\sim$20 - 200 s). This enables the imaging of crustal structure, which is difficult with longer periods.

Despite all of the above, some disadvantages exist as well:

- A major assumption when using ambient noise is that the distribution of noise sources in space is homogeneous. If this assumption is not approximately true, waveforms may be wrongly reconstructed and careful comparison to existing data should be used when possible. However, several works (Yao and van der Hilst, 2009; Fichtner, 2014) show that the effect of this on narrow band travel times which are used in this work is mostly negligible.

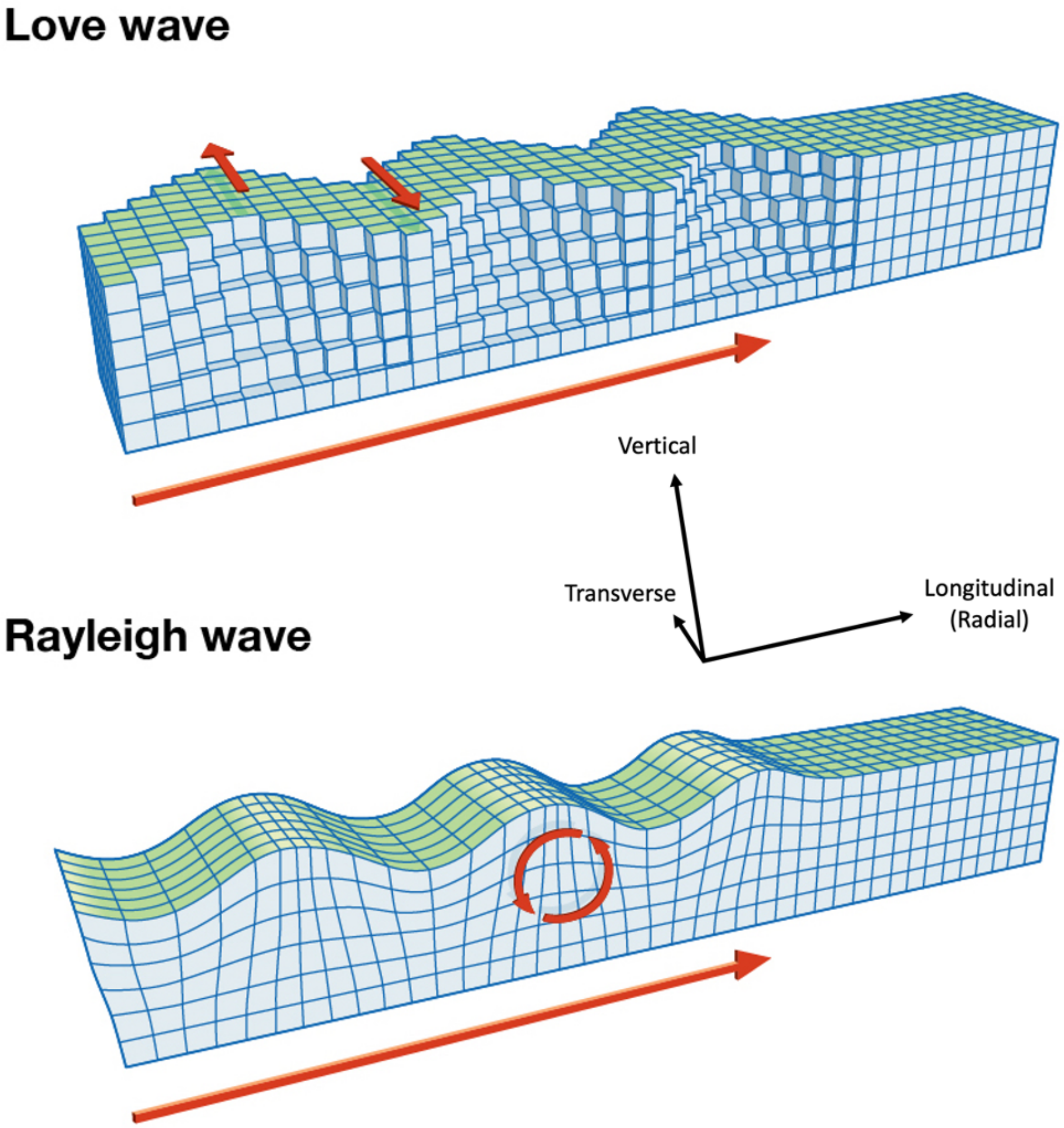

Fig. 1.5 The contrasting ground motion patterns of of Love and Rayleigh waves. Rayleigh waves have a longitudinal and vertical motion and Love waves have a transverse motion. Source: Britannica

- Using ambient noise requires processing large amounts of data and is therefore resource and time consuming when compared to earthquake tomography. For example, the dataset processed in this work consists of several tera-bytes of data, containing many years of continuous seismic recordings. In recent years, advances in modern computing power has mostly made this issue manageable.

- The relatively short usable period range ($\sim$1 - 40 s) mostly limits the investigation to crustal and upper mantle depths, although several studies have shown that the use of very long periods (100 - 300 s) is also possible (Nishida et al., 2009; Sager et al., 2020).

- The use of ambient noise is lacking wave-equation-based forward modelling of EGFs, although recent progress has been made (Lu et al., 2020; Chen et al., 2014; Liu et al., 2017). For example, Lu et al. (2020) has forward modelled the EGFs by simulating 64 point force sources with uniform distribution across the Alps and argue that they have achieved significantly better constraints compared to previous tomographic models.

As we shall see in the following chapters, thanks to the clear benefits of using surface wave velocities from ambient noise, and despite a few caveats, this method has yielded, and continues to yield, exciting new discoveries.

1.3.2 A brief history of ambient seismic noise

As mentioned, until recently surface wave dispersion could only be measured using seismic waves emitted by earthquakes or explosions. Several theoretical and laboratory studies (Lobkis and Weaver, 2001; Derode et al., 2003) have suggested that surface wave velocities could be extracted from the diffuse wave field. Shapiro and Campillo (2004) demonstrated for the first time (Fig. 1.6) that Rayleigh wave velocities between two station could be measured using a simple cross-correlation of random ambient noise and showed that the resulting dispersion curves were highly similar to those from earthquake tomography of the same region, as presented in Ritzwoller et al. (2002) . They then suggested that these data could be subsequently used in tomographic imaging. This was later demonstrated by Shapiro et al. (2005) in Southern California who produced a tomographic image using ambient noise only (Fig. 1.7). This image showed a striking resemblance to known geological features, thus proving the usefulness of the method. They further showed that where it was possible to compare, surface wave dispersion measured from ambient noise and earthquakes were highly similar. This was followed by a rapid growth in popularity of the new method since it allowed imaging in regions and at depths that were previously not possible with passive methods and a could be applied to old datasets. Examples range from tectonic scale (100s of km, e.g. Pilia et al., 2015; Green et al., 2017; Yao and van der Hilst, 2009) to local (10s of km, e.g. De Siena et al., 2018; Obermann et al., 2016; Brenguier et al., 2007; Masterlark et al., 2010) scale such as in volcano seismology and several applications at global scale (e.g. Nishida et al., 2009; Sager et al., 2020).

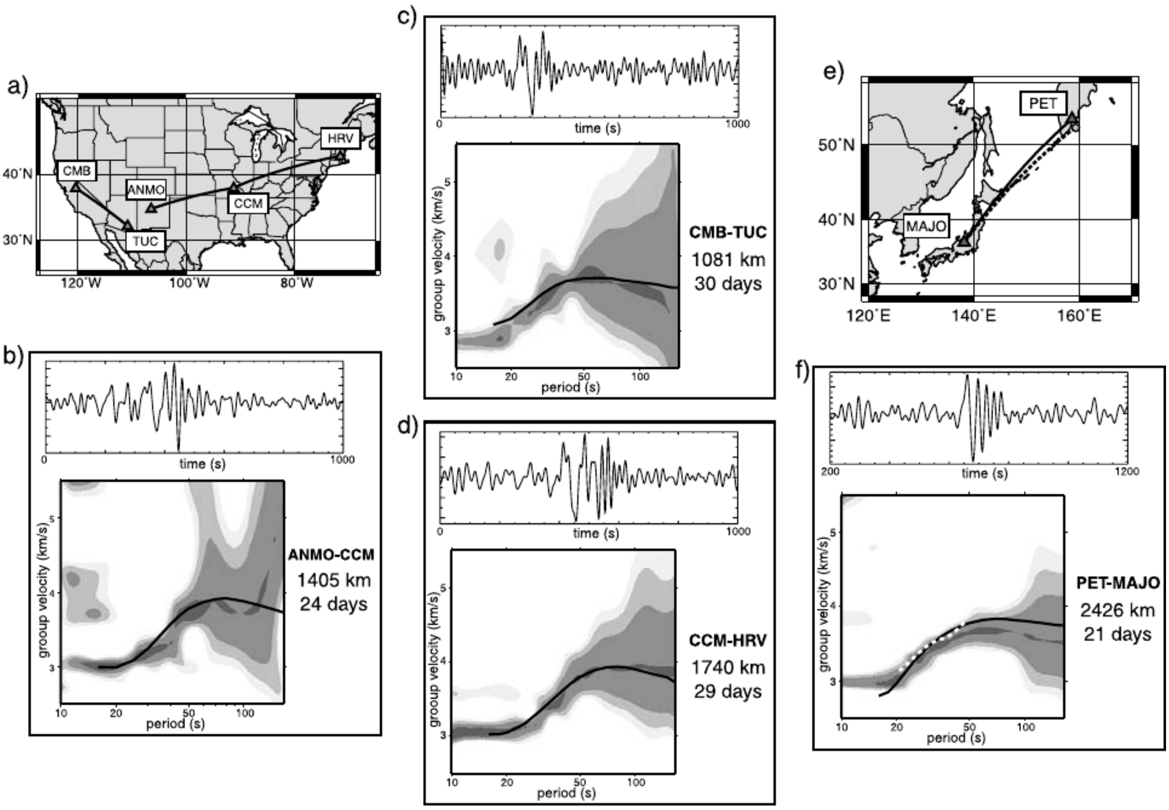

Fig. 1.6 The first demonstration of the emergence of Rayleigh waves from correlations of the ambient noise from Shapiro and Campillo (2004). Each of the panels **b-f** displays an FTAN image from noise cross-correlations with a solid line denoting the group dispersion curve extracted from teleseismic surface waves along the same path. It can be seen that the resemblance between the two is striking.

1.3.3 Ambient noise sources

Due to the growing popularity of ambient noise in various applications including seismic imaging, the sources of ambient noise are of great interest as they play an important role in the theoretical understanding of the method (i.e. measuring surface wave dispersion from ambient noise) and limit the usable period range. Spectral amplitude plots of ambient noise usually display a typical pattern as shown in Figure 1.8 (Bensen et al., 2007). The

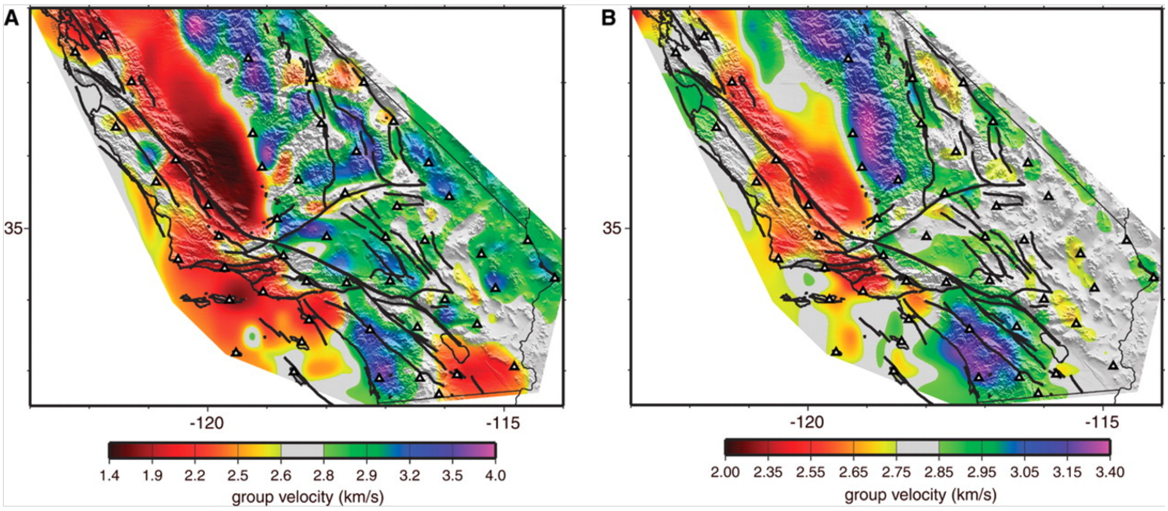

Fig. 1.7 The first demonstration of ambient noise tomography from Shapiro et al. (2005). Panels A and B show group-speed maps constructed from ambient noise at 7.5 s and 15 s periods respectively. Black solid lines show known active faults. The location of the slow anomalies correlates well with the location of known sedimentary basins.

most energetic parts of the spectrograms are usually the primary (∼14 s, 0.07 Hz) and secondary (∼7 s, 0.14 Hz) oceanic microseisms that are the result of ocean waves. This may change somewhat spatially and temporally depending on the ocean basin and weather conditions. At long periods (>50s, 0.02 Hz), a peak known as “Earth’s hum” exists, associated with the fundamental resonant spheroidal oscillations of the Earth (Rhie and Romanowics, 2004). Another smaller peak sometimes exists around 26s (0.038 Hz). Its source is not fully understood but it has been traced to the Gulf of Guinea and is thought to be associated with resonance in an ocean basin (Shapiro et al., 2006). High frequency (> 1Hz) ambient noise sources also exist and include wind, anthropogenic noise, small earthquakes and volcanic events (Hillers and Ben-Zion, 2011).

In Iceland, the ambient noise spectrum clearly displays the typical microseisms peaks (Fig. 1.9a) as well as earth’s hum. Green (2016) has analysed the distribution of noise sources in Iceland and showed that the ray paths with the strongest SNR are have back azimuths around 160° - 250° (Fig. 1.9b) which they attributed to the location of the main North Atlantic basin, where large storms generate powerful microseisms. Fortunately, noise directionality is not similar to the azimuth of spreading in Iceland (106°). This is important since we will later explore seismic anisotropy related to the spreading direction, and can use this fact to distinguish it from anisotropy related to the noise sources.

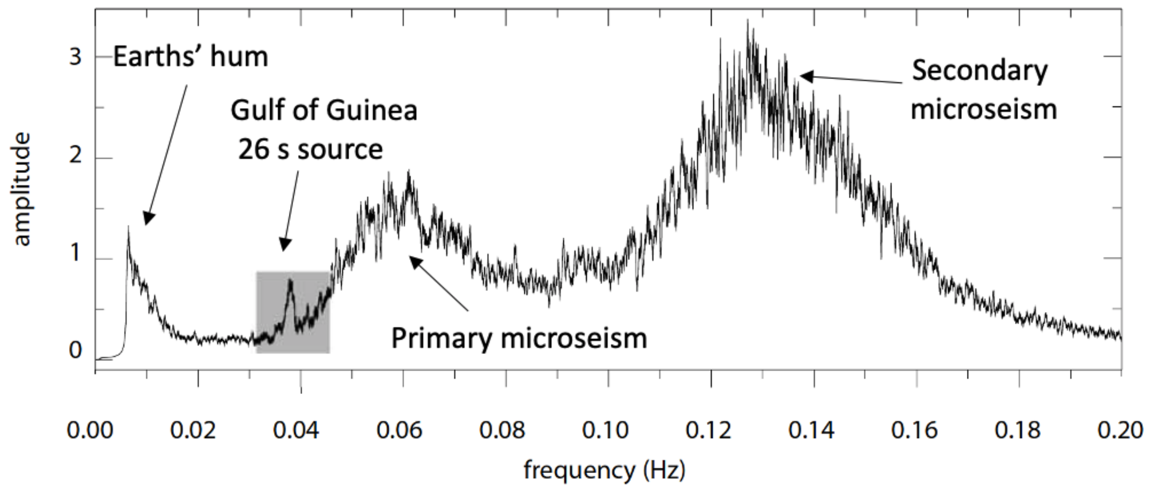

Fig. 1.8 An example of the ambient noise spectrum recorded by a Global Seismic Network station (HRV located in Harvard, Massachusetts) showing the typical energy distribution of ambient noise (from Bensen et al., 2007).

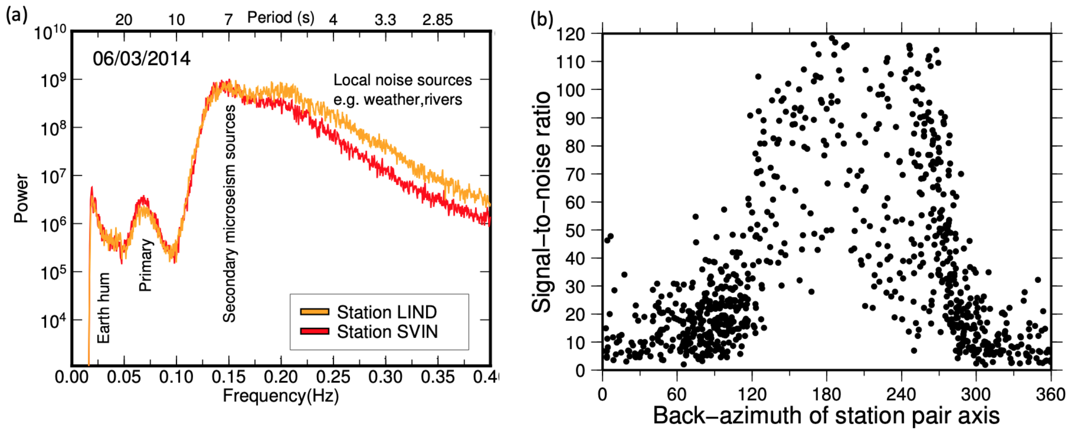

Fig. 1.9 An analysis of ambient noise characteristics in Iceland (from Green, 2016). (a) The power spectrum for seismic noise is shown for the two stations LIND and SVIN. (b) SNR versus back-azimuth of station pair.

1.3.4 Seismic anisotropy

Seismic anisotropy is the dependence of seismic wave speeds on the polarization or propagation direction of the waves. This phenomena has been observed in different parts of Earth's interior, including the crust, mantle and the inner core, and has gained much scientific interest due to its relationship to deformational and other dynamic processes (Long and Becker, 2010). One commonly cited mechanism for seismic anisotropy is lattice (or crystallographic) preferred orientation (LPO, CPO) (Long and Becker, 2010). Many common minerals (e.g. olivine, pyroxene, mica, plagioclase) exhibit seismic anisotropy at the single crystal level, a phenomenon which may manifest itself in seismic wave velocities where crystals are preferentially aligned over a sufficiently large region. The other commonly cited mechanism for seismic anisotropy is the shape preferred orientation (SPO) of features with distinct isotropic elastic properties (Backus, 1962). Examples for SPO include alternating layers in sedimentary basins (e.g. Dreiling et al., 2018), sills of different compositions (e.g. Russell et al., 2019) and oriented melt pockets (e.g. Bastow et al., 2010). Although seismic anisotropy may be arbitrarily oriented, it is often divided into azimuthal (i.e. velocity variations within the horizontal plane) and radial (i.e. velocity variations between the horizontal and vertical directions) anisotropy for simplicity.

One of the most common approaches for investigating seismic anisotropy is through the exploration of surface wave characteristics. Surface waves are effective for exploring azimuthal anisotropy (e.g. Debayle et al., 2005; Lin et al., 2016) since they travel (to first order) at a roughly constant azimuth. Surface waves are also very useful for studying radial anisotropy (e.g. Dreiling et al., 2018; Dziewonski and Anderson, 1981) which can be inferred by comparing the velocities of Love waves which are primary sensitive to V_{SH} to those of Rayleigh waves which are primary sensitive to V_{SV}.

Seismic anisotropy in the oceanic upper mantle and crust

Seismic anisotropy has been widely observed in upper oceanic mantle. Hess (1964) observed that Pn wave velocities (Raitt, 1963; Shor and Pollard, 1964) are low perpendicular to the fracture zones and high parallel to them. He then argued that this was a result of the preferred alignment of olivine crystals due to upper mantle flow (ductile deformation), an explanation which has become widely accepted. Anderson (1965) observed a discrepancy between Love and Rayleigh wave velocities in oceanic upper mantle which required radial anisotropy such that the shear velocity in the horizontal direction is greater than in the vertical direction, a phenomenon which is also attributed to olivine LPO. The alignment of olivine crystals requires the presence of internal shear which is thought to occur near oceanic spreading ridges (e.g. Blackman et al., 2002; Blackman and Kendall, 2002), where upwelling mantle undergoes corner flow. The aligned olivine crystals are then fossilized into the lithospheric mantle which moves away from the ridge with plate motion (Lin et al., 2016).

In oceanic crust, observations of anisotropy have primarily been interpreted using oriented cracks (Bacon et al., 2019; Stephen, 1981; Shearer, 1988; White and Whitmarsh, 1984) which can be observed as crack-parallel Rayleigh wave fast directions, and fast V_{SV} relative to V_{SH} (Hudson, 1981). Recently, radial anisotropy with $V_{SH} > V_{SV}$ has been observed in the Pacific crust (Russell et al., 2019) and has been interpreted using SPO in the form of layered intracrustal reflectors. In Iceland, surface wave anisotropy has been observed in the mid-lower crust (Bjarnason and Schmeling, 2009), with suggested mechanisms that include sills, dykes and LPO, but insufficient azimuthal coverage has prevented a decisive interpretation.

Chapter 2

Data and Methods

This section provides an overview of the various methods used throughout the different parts of this dissertation. Each individual chapter provides additional details regarding implementation.

2.1 Seismic data

2.1.1 Datasets

This study uses 3-component continuous broadband waveforms from five non-simultaneous seismic networks with a total of 189 stations deployed across Iceland (Fig. 2.1).

Cambridge Network

145 stations are sourced from a dense ongoing deployment operated by the University of Cambridge, mostly covering the NVZ and the EVZ. This network has been deployed in the Icelandic highlands since 2008 and has continued to operate until today, although the number and location of instruments has changed significantly throughout the years. The network was initially focused around Askja and included 16 instruments. Over time, the network size increased, peaking at 70 stations in 2014 and then decreasing to about 30 in recent years. The coverage of the network has also changed significantly and has included areas in the EVZ, Krafla volcano in the north and a number of remote back-bone stations for regional scale tomography such as SVIN, SNAE and BRUN. Today the network is largely focused on Askja and Bárðarbunga volcanoes. Despite the many changes in network setup, some stations, such as FLAT, remains operational since its initial deployment and provide long standing continuous seismic recordings which are highly valuable for investigating long term

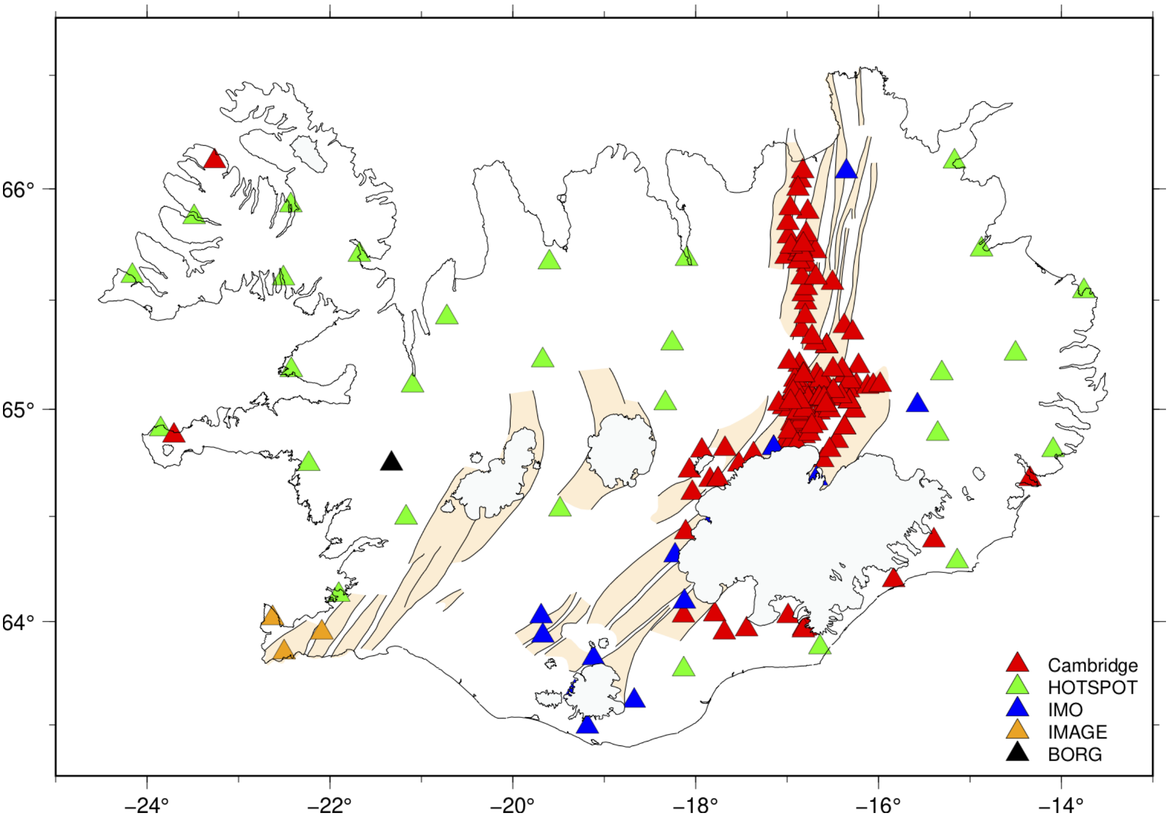

Fig. 2.1 Map of stations (denoted by triangles) used in this work. Colours indicate different networks. The HOTSPOT network (green triangles) operated from 1996 to 1998 (Allen et al., 1999). Station BORG of the GSN network (black triangle) has been recording continuously since 1994. The IMAGE project network in Reykjanes (orange triangles) operated in 2014 - 2015. The Cambridge network (red triangles) has been operational since 2008 but the location and number of stations has varied significantly. The IMO network is a permanent network but data availability is variable.

changes.The instruments used to collect this dataset are primarily Güralp 6TDs (30 s corner frequency), Güralp 3ESPCDs (60 s), and a limited number of Güralp 3Ts (120 s). This year, a number of Güralp Certimus (120 s) instruments were added to the network but the data from those are not yet recovered and therfore are not used in this work. Güralp 6TDs are mostly buried directly in the ground whereas the longer period instruments were deployed in small vaults. Data is recorded at 50 - 100 samples per second and recovery rate is normally above 80%. A detailed description of fieldwork procedures for this network is provided in a later section. The dataset is freely available from IRIS and FDSN under network code Z7: http://www.fdsn.org/networks/detail/Z7_2010/.

HOTSPOT Network

30 stations from the HOTSPOT experiment (Allen et al., 1999) which operated from 1996 to 1998 provide highly valuable backbone stations for regional coverage. The HOTSPOT instruments cover most of Iceland with a typical station spacing of 50 km. The instruments are mostly Guralp CMG3-ESPs, but include some Guralp CMG-40Ts and one Guralp CMG-3T. Data is recorded at 20 samples per second. This dataset is freely available from IRIS and FDSN under network code XD: https://www.fdsn.org/networks/detail/XD_1996/

GSN station BORG

Data from the permanent station BORG of the Global Seismic Network was also used. The station includes a Streckeisen STS-2 installed in a concrete vault and has been recording continuously since 1994. This dataset is freely available from IRIS and FDSN under network code II: https://www.fdsn.org/networks/detail/II/

Icelandic Meteorological Office Network

10 permanent stations from the Icelandic Meteorological Office (IMO) are also used in this work and add additional coverage, mostly in the volcanic zones. The types of instruments are similar to the Cambridge network with dominantly Güralp instruments installed in vaults. This dataset is available upon request from IMO at their discretion.

IMAGE project Network

3 stations from the temporary IMAGE project in the Reykjanes ridge which operated in 2014 -2015 were also used to provide coverage in the south-west of Iceland. The instruments used in this experiment were Streckeisen STS-2 with a corner frequency of 120 s. This dataset is available upon request from GFZ at their discretion.

2.1.2 Data collection

In this section I describe the details of passive seismic data acquisition for the network run by the University of Cambridge in the Icelandic highlands. During my PhD I have taken part in several trips to service the network and deploy new instruments and, in the last year, have been in charge of organizing fieldwork in Iceland. I have also contributed to the design of the seismic station set-up in the field.

Challenges

One major challenge in installing seismic instruments in the Icelandic highlands is the region's remoteness. For most of the area covered by the network, the driving distance to Reykjavik, our logistical base, is between one and three days, making frequent visits to most sites unfeasible. Therefore, station setup and power supply should be robust enough to withstand a full year without a service. Furthermore, the nearest towns where supplies can be purchased are at least a day of driving away, meaning that logistics require very careful planing. Most of the highlands are not covered by cellular towers, limiting the option to telemeter data from the instruments and further complicating fieldwork operations.

The second major challenge in operating the network is Iceland's high latitude and harsh weather conditions. For much of the year the Icelandic highlands are not accessible by car due to snow cover. Thick snow cover in some places may also prevent sunlight from reaching the solar panels. Furthermore, for many months in the year the ground is frozen. This makes digging in the ground impossible and damages lead acid batteries which are used to power the instruments. Freeze-thaw cycles may lead to damage and water penetration to instruments or other sensitive parts of the system such as regulators. Iceland also has very strong winds which sand blast the solar panels and make them less efficient. Wind may sometimes completely shear off or destroy parts of the solar panel stand. Finally, charging batteries with solar panels is a challenge in high altitudes as they receive very little sun during winter. The station setup presented below (Fig. 2.2) is therefore mainly aimed at dealing with these challenges.

Station setup

Seismometer

The most important considerations for seismometer deployment are to avoid the tilting of the instrument throughout the year, and to increase coupling with the ground. In our network seismometers are installed in one of two ways, either in a small vault or directly into the ground. Installing directly into the ground is easier but increases the risk of tilt. It is therefore only used for Guralp 6TDs which are less sensitive to tilt. The instruments buried in this way are more prone to the effects of ground freezing and thawing which can often be seen as a sharp tilt of the instrument's masses (Fig. 2.3) but mostly does not hurt the quality of data recovered. Guralp 3ESPs are only installed in vaults, which are made from plastic fish barrels and have a concrete slab at the bottom to reduce the effects of soil erosion and/or compaction. Where possible, drainage pipes are installed to allow water to escape from the vault. The instrument's internal clock is continuously synced using an external GPS antenna located on a pole. Most instruments have 16GB of storage space which means that in order to last a full year they are set to record at 50 samples per second. A few instruments only have 4GB of storage and are usually set to record on the Z component only in order to last a full year.

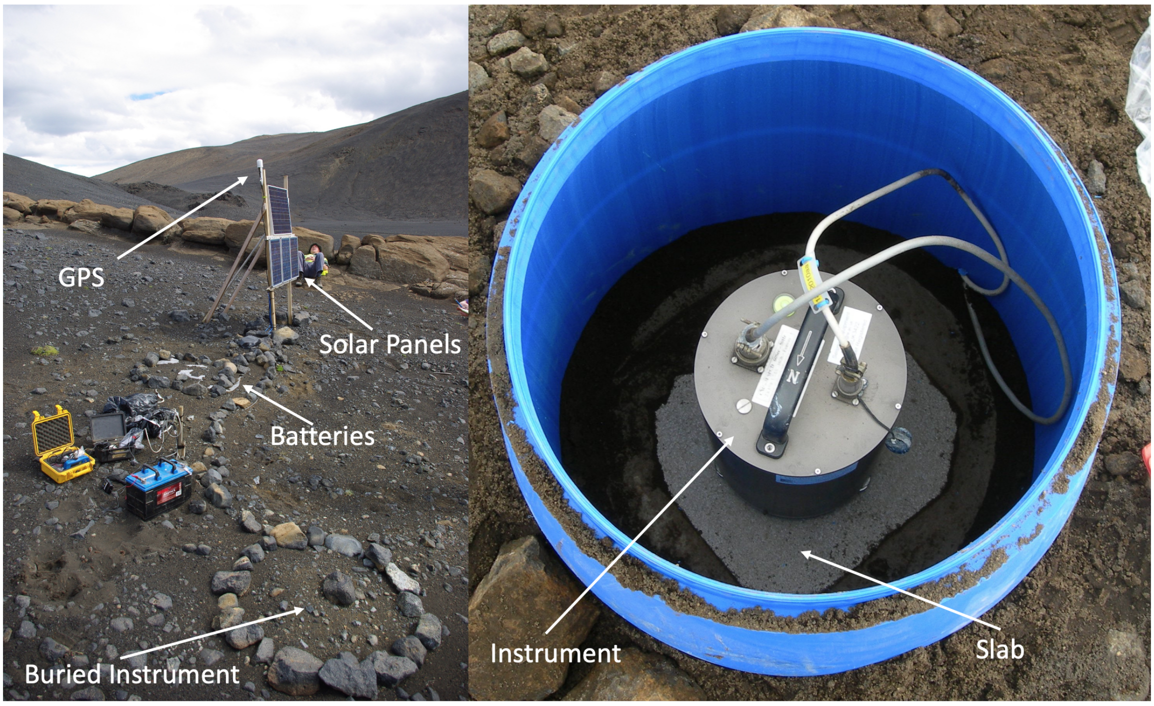

Fig. 2.2 **left** A typical station setup in the Icelandic highlands. **right** Seismometer installation in a vault.

Power system

The power system is comprised of batteries, solar panels and a regulator. We use 120Ahr lead-acid truck batteries which are usually buried in the ground next to the instrument. To last the full winter, instruments require between 2-5 such batteries depending on their condition, the instrument type and the number and state of the solar panels. Stations typically require at least 4 solar panels (depending on size and type, but usually in the range 20 - 40 W) to keep the batteries charged to a sufficient level during winter. Solar panels are mounted on wooden stands and are raised off the ground to avoid snow cover. The panels are placed at a near vertical angle in order to maximize charging when the sun is very low during winter months and reduce snow and dust accumulation. The regulator connects the different parts of the system, protects the instrument from over current using a fuse, and disconnects the instruments from the batteries to protect them when the charging level is too low.

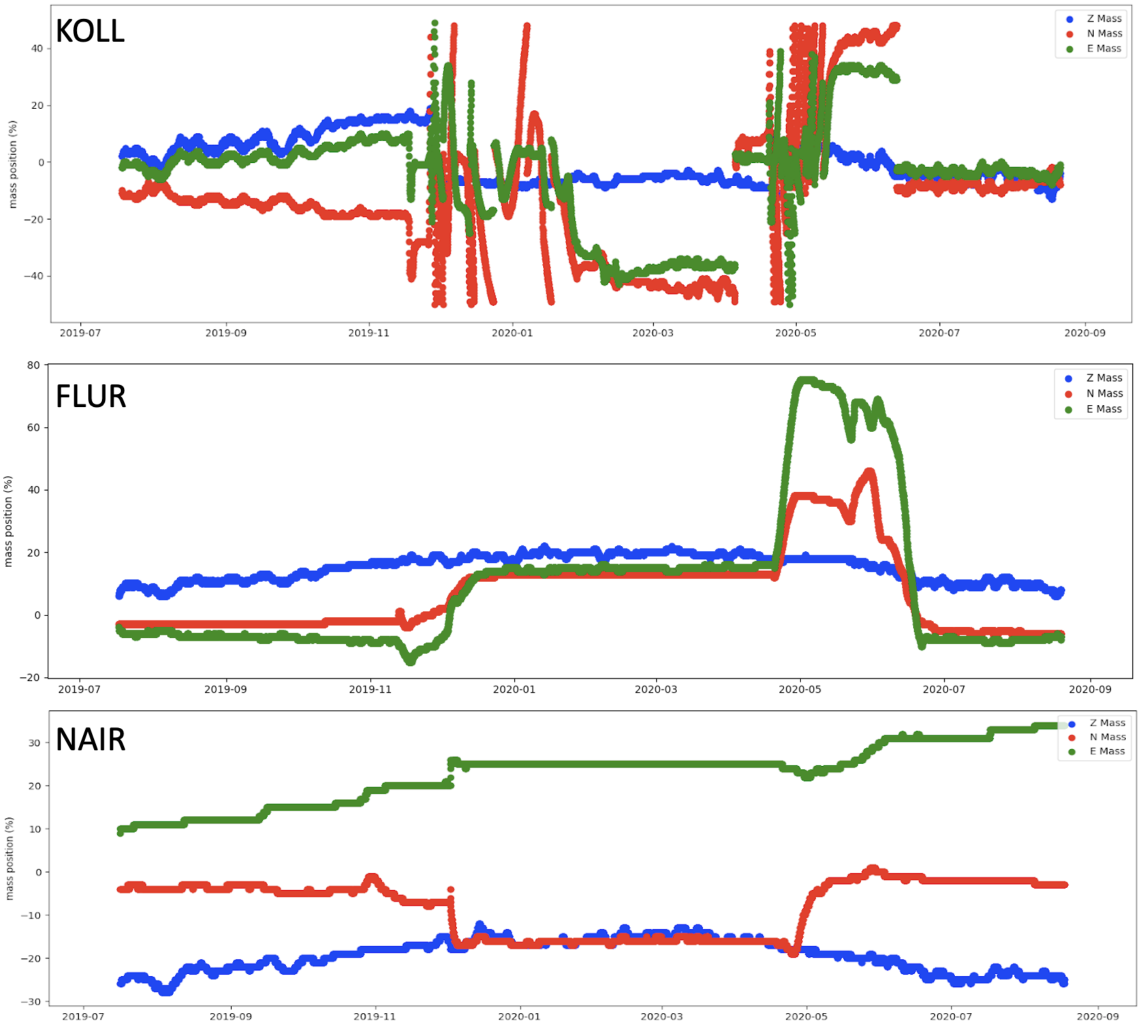

Fig. 2.3 Freeze thaw cycle effect on instrument masses at 3 station. All 3 stations show a large change in horizontal mass position around December when the ground freezes and again when it thaws in May. The instrument at KOLL (top) is an ESP and the sharp changes causes it to try and recenter its masses. The instruments at FLUR (middle) and NAIR (bottom) are 6TDs

Common failures

Despite the challenges, the recovery rate of the network is usually above 90% with many stations giving 100% routinely. Data availability for 2019 - 2020 can be seen in Figure 2.4. Some of the common causes for data loss are:

- Power loss during winter - If batteries or solar panels degrade over time due to the difficult conditions, seismometers will sometimes loose power for 1-2 months, usually around March when batteries get depleted. Power is usually restored around May. This typically happens to one or two stations every year.
- Regulator failure or fuse burn - While regulators are designed to be waterproof, water penetration does occur at times and can cause the regulator to fail. Moreover, if there is high current from the battery to the instrument, the fuse may burn. While this is intentional, the fuse may be over sensitive at times. This typically happens to two or three stations every year.
- GPS failure - For unknown reasons, GPS antennas will sometimes fail. From that point on the data is no longer timestamped correctly and is usually discarded. This is relatively rare and will happen less than once a year on average
- Instrument failure - Complete instrument failures are rare but do occur sometimes due to being exposed to harsh conditions for many years. This also happens less than once a year on average

2.2 Methods

2.2.1 Empirical Green's Functions from ambient noise

To obtain surface wave dispersion curves from ambient noise, we must first extract Empirical Green's Functions (EGFs). A (true) Green's function is defined as the domain's displacement response due to a point force impulse and can be used to measure phase/group velocity, as shown later. An EGF on the other hand, is an empirical estimation of the domain's Green's function. Previous studies have demonstrated that EGFs obtained from ambient noise are equivalent to the true Green's function except for a frequency-dependent amplitude correction (Roux et al., 2005; Weaver and Lobkis, 2004; Lobkis and Weaver, 2001; Sabra et al., 2005). This process of calculating EGFs from ambient noise is divided into two steps: single station preprocessing and pair-wise processing.

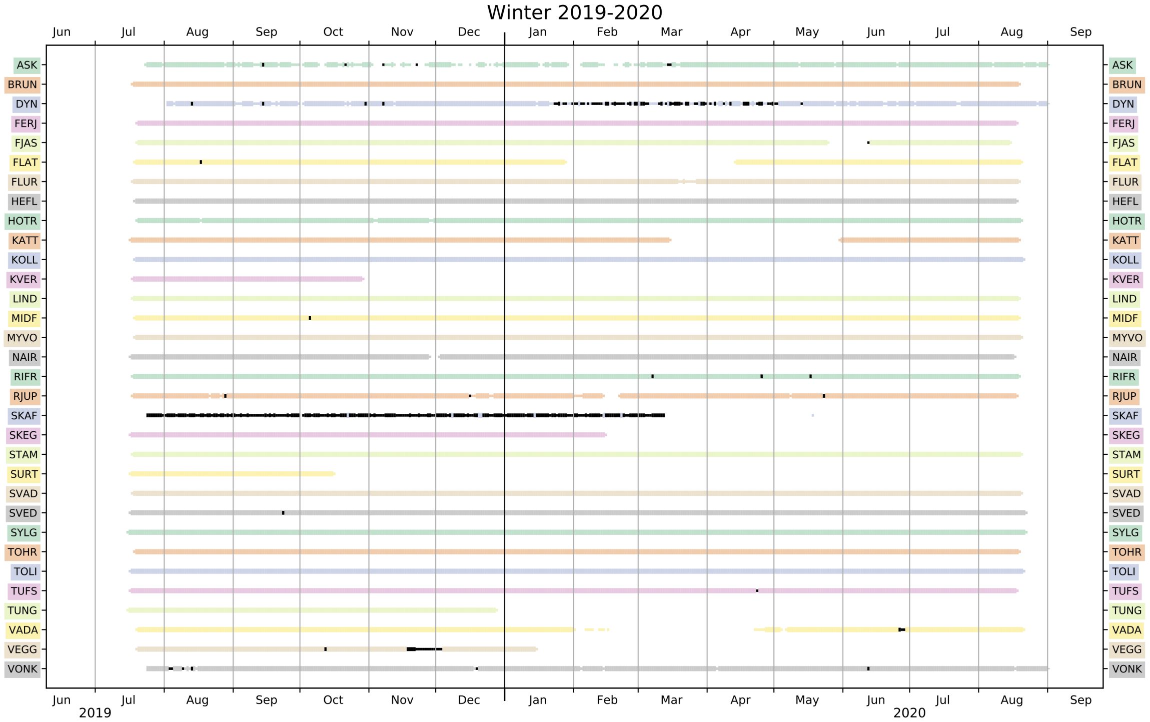

Fig. 2.4 Data availability from July 2019 to August 2020. Each line represents a station. Black colour denotes transmission gaps in stations telemetered by IMO.

Single station Preprocessing

First, the waveforms at all available stations are preprocessed following Bensen et al. (2007). The continuous waveforms are divided into 30-minute-long sections which are then demeaned, detrended, tapered and decimated to 1 Hz. Next, the instrument's response is removed using deconvolution and the resulting waveform is convolved with the response of the instrument with the narrowest period band used in the analysis. The convolution step is important in order to prevent the noise from overwhelming the signal at long periods. This is followed by winsorizing (replacing extreme values with truncated ones) at 3 RMS (Root Mean Square), which reduces the effect of large amplitude spurious arrivals, and spectral whitening. Spectral whitening is the procedure of dividing the frequency domain representation of the signal by a smoothed version of itself in order to flatten it. This helps to enhance noise at lower energy frequencies. Although widely used, it should be noted that this processing scheme may introduce an unphysical component into the noise correlations and to a lesser extent, into the dispersion information (Fichtner et al., 2020).

Pair-wise Processing

The resulting preprocessed continuous signal from all possible station pairs are cross-correlated, which is defined as:

$$C(x_{\mathrm{A}}, x_{\mathrm{B}}, t) = \int u(x_{\mathrm{A}}, \tau)\, u(x_{\mathrm{B}}, t + \tau)\, d\tau \tag{2.1}$$

where u is the signal, x_A and x_B are the stations, t is time and τ is the time shift (Fig. 2.5a). The resulting cross-correlations are then stacked to produce a Noise Cross-correlation Function (NCF) for each station pair. We use phase-weighted stacking (Ventosa et al., 2017), which applies phase coherence to attenuate incoherent noise and improves SNR (Signal to Noise Ratio) when compared to conventional linear stacking (Fig. 2.5b-c). The NCF usually displays a large amplitude signal representing the surface wave arrivals on both the causal (positive) and acausal (negative) parts. The positive and negative arrivals are the result of waves traveling in opposite directions between the two stations. A different approach than the one used here for computing cross-correlation is called Phase Cross-Correlation (PCC) (Schimmel, 1999). This approach is theoretically superior (Schimmel et al., 2011) to the simple cross correlation presented here in achieving high SNR but is rarely used due to its very high computational cost (Ventosa et al., 2019). Nonetheless, I have attempted this method on a portion of the full dataset and the improvement in SNR was practically negligible compared to simple cross correlation with phase weighted stacking as shown in Fig. 2.6.

Horizontal rotation from N-E to R-T

In order to extract dispersion data from the horizontal components, the data requires rotation from the originally recorded north and east (N-E) orientations to radial and transverse (R-T). The most intuitive way to achieve this is by rotating the single station signal before the cross-correlation step using:

$$\begin{pmatrix} R \\ T \end{pmatrix} = \begin{pmatrix} \cos\theta & \sin\theta \\ -\sin\theta & \cos\theta \end{pmatrix} \times \begin{pmatrix} N \\ E \end{pmatrix} \tag{2.2}$$

where θ is the azimuth between the two stations and R, T, N and E are the radial, transverse, north and east components respectively. After this simple rotation, it is then possible to follow up with the pair-wise processing described above. However, it is computationally much more efficient to first do the cross-correlation and then rotate the signal. To achieve

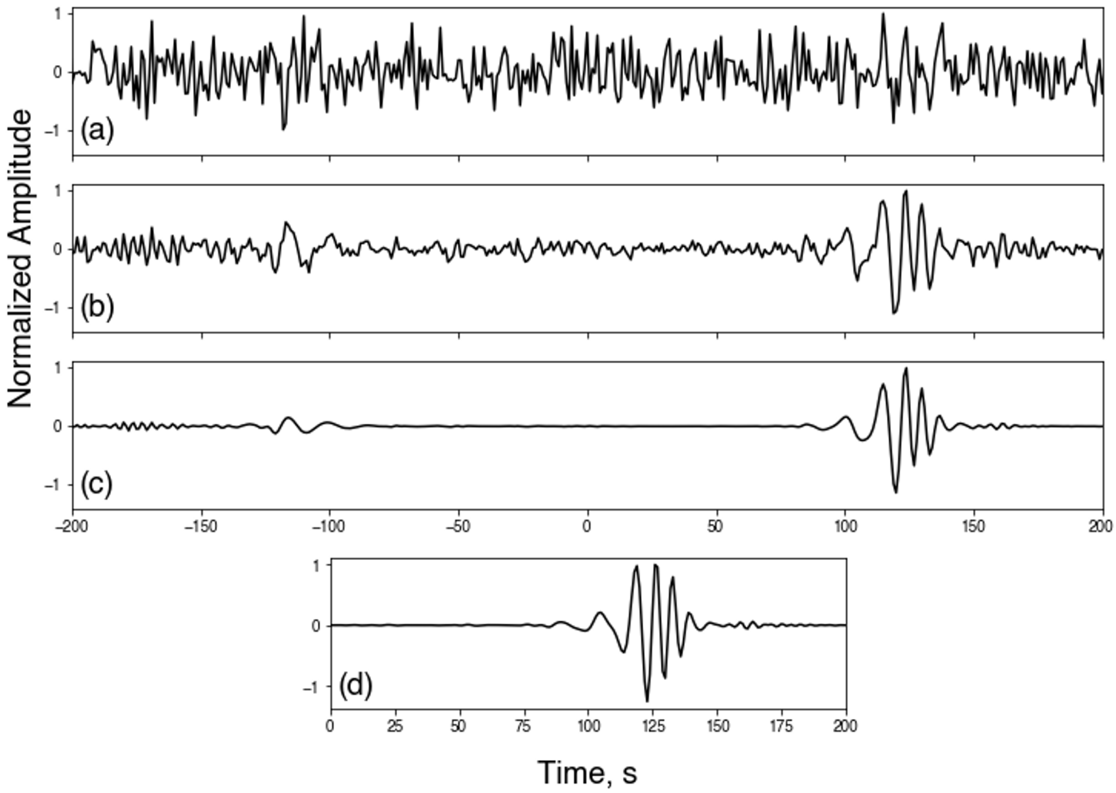

Fig. 2.5 Noise cross-correlation stacking and EGF extraction. **a** Cross-correlation of one day of continuous recordings of the vertical components of stations BORG and HOT19. **b** A linear stack of 520 days of cross-correlations for the same stations. **c** Same as **b** but using phase weighted stacking. **d** The EGF calculated from **c** by averaging the causal and acausal parts and taking the time derivative

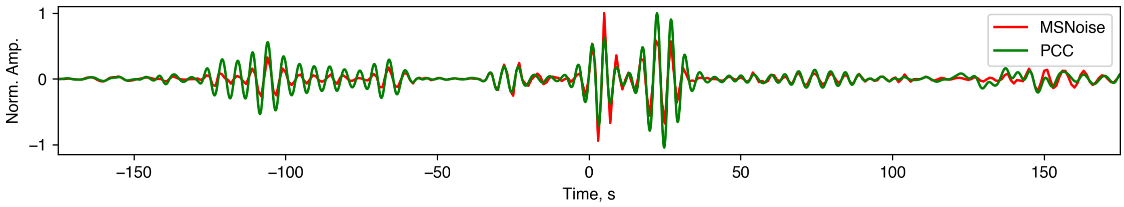

Fig. 2.6 NCFs obtained used two different methods are displayed for the station pair SBA9 - SBB2 (317 km apart). A red line denotes the NCF obtained by using a simple cross-correlation and phase weighted stacking, and a green line denotes the NCF obtained by using Phase Cross Correlation.

this we first compute the following cross-correlations: NN, EE, NE and EN, and then apply the following transform:

$$\begin{pmatrix} TT \\ RR \\ TR \\ RT \end{pmatrix} = \begin{pmatrix} -\cos\theta\cos\psi & \cos\theta\sin\psi & -\sin\theta\sin\psi & \sin\theta\cos\psi \\ -\sin\theta\sin\psi & -\sin\theta\cos\psi & -\cos\theta\cos\psi & -\cos\theta\sin\psi \\ -\cos\theta\sin\psi & -\cos\theta\cos\psi & \sin\theta\cos\psi & \sin\theta\sin\psi \\ -\sin\theta\cos\psi & \sin\theta\cos\psi & \cos\theta\cos\psi & -\cos\theta\sin\psi \end{pmatrix} \times \begin{pmatrix} EE \\ EN \\ NN \\ NE \end{pmatrix} \tag{2.3}$$

Here, θ and ψ are the azimuth and back-azimuth between the two stations. The double letter notation is used such that for example, NE represents the cross-correlation of the north component from the first station with the east component of the second station. Since all operators used in the described processing are commutative with the rotation operator, performing the rotation after the cross-correlation gives exactly the same result as doing it before.

Much of the data processing work flow that is described is preformed using MSNoise (version 1.6), a python package for ambient noise analysis (Lecocq et al., 2014), available at: http://www.msnoise.org/. ts-PWS, a software for computing the time-scale phase-weighted stack is available at: https://github.com/sergiventosa/ts-PWS. FastPCC, a computer program for efficiently computing the phase cross-correlations is available at: https://github.com/sergiventosa/FastPCC.

Plotting the NCFs as a function of station separation displays a move-out pattern as seen in Figure 2.7, indicating that the signal observed on the NCF is indeed a function of the path between the two stations. The vertical component arrivals represent Rayleigh waves and the transverse component arrivals represent Love waves.

The EGF can then be simply calculated from the NCF by taking the time derivative (Lin et al., 2008) of either the causal or acausal parts which in theory are supposed to be identical (Fig. 2.5d). However, real world NCFs are not always symmetrical due to an inhomogeneous distribution of noise sources. Some studies therefore use the side with the larger amplitude, whereas others, including this work use the average of the causal and acausal parts. The relationship between the EGF and the NCF is therefore:

$$EGF_{AB} = -\frac{d}{dt}\left[\frac{NCF_{AB}(t) + NCF_{BA}(-t)}{2}\right], \quad 0 \leq t \leq \infty \tag{2.4}$$

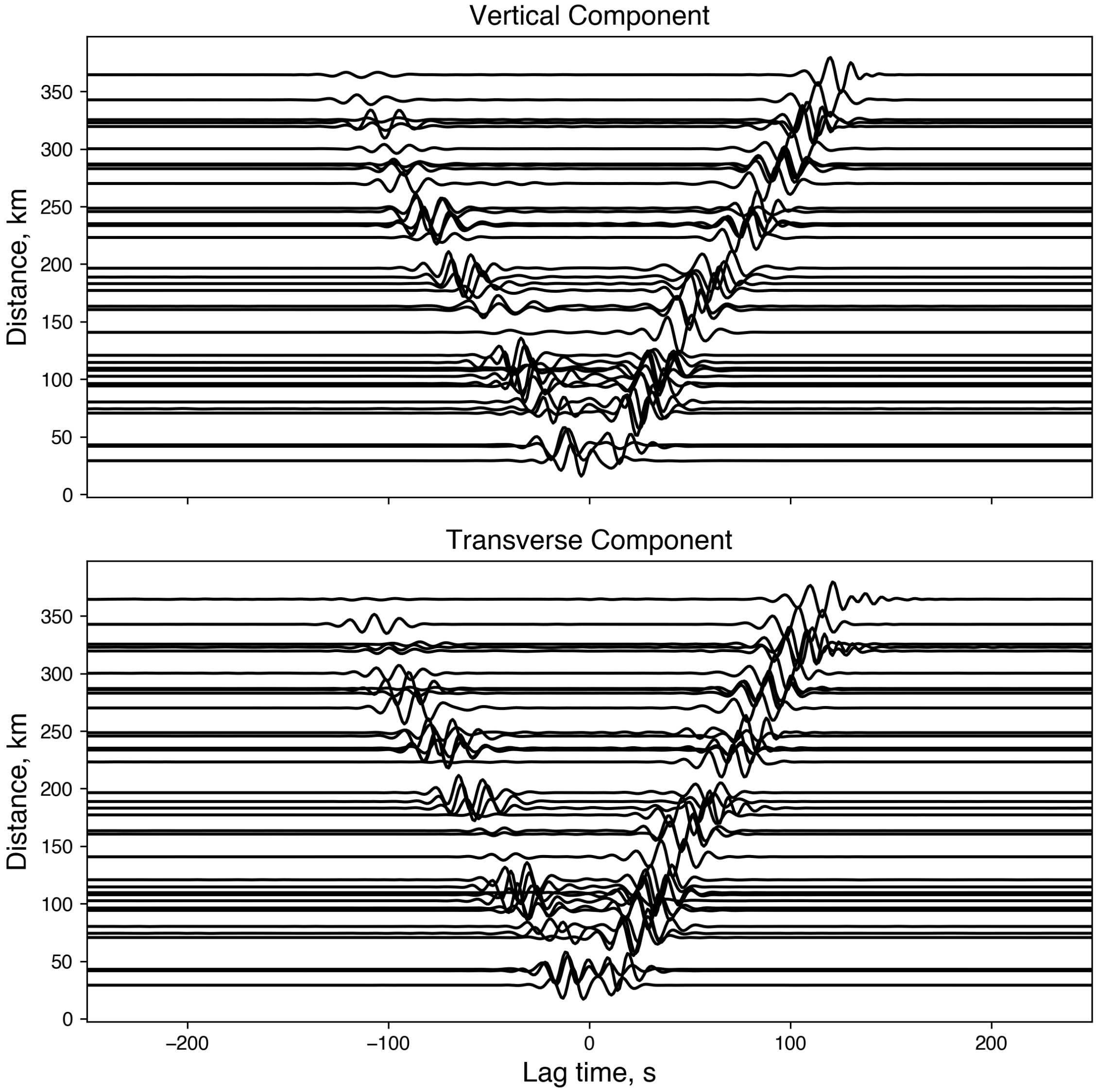

Fig. 2.7 Noise cross correlation functions extracted from the vertical and transverse components for station pairs that include station BORG display a typical move out pattern. The NCFs are bandpass-filtered between 10 - 60 s. The vertical component arrivals represent Rayleigh waves and the transverse component arrivals represent Love waves.

2.2.2 Phase dispersion data from EGFs

To measure phase dispersion data from EGFs we use the image transformation technique as described in Yao et al. (2006). The EGF (note: the EGF itself, not the envelope of the analytic signal as for group velocity) is subjected to a series of narrow band pass filters at discrete central frequencies with a width of 0.4 s. We apply a two-pass filter to avoid the phase shift introduced by filtering. The resulting signal at each period has multiple peaks, one of which corresponds to the correct phase arrival time. We then convert the filtered EGF at each frequency from a time-period domain to a velocity- period domain using the relationship:

$$c = \frac{r}{t - \frac{T}{8}} \tag{2.5}$$

where c is phase velocity, r is the station separation, t is travel time and T is the central period. This equation should not be confused with a similar equation developed by Brune et al. (1960) for extracting phase velocity which additionally includes a term for phase velocity ambiguity. In the equation of Brune et al. (1960), c and t represent exact values, whereas in equation 2.5 they represent continuous domains, thus there is no notion of ambiguity. The ambiguity is of course still present and is accounted for later, as discussed below. For the full derivation see Yao et al. (2006). Combining the separate waveforms at each central period into a matrix yields a velocity-period image as seen in Figure 2.8. The velocity-period image usually displays several possible dispersion curves, representing the built-in ambiguity in picking phase velocity mentioned earlier. This is usually solved by using a regional reference curve and picking the closest one to it. An automatic process that I developed for creating velocity - period images, calculating a reference curve, and picking phase dispersion curves is described in detail in chapter 5.

Another approach for measuring phase velocity from EGFs which is not utilized in this work, also exists. This method, sometimes known as AKI's method, was demonstrated by Ekström et al. (2009), based on early work by Aki (1957). As shown by Aki, the real part of the frequency domain representation of the cross-correlation function should resemble a Bessel function and its zero crossings can be used to calculate phase velocity from:

$$c(\omega_n) = \frac{\omega_n r}{z_n} \tag{2.6}$$

where ω_n is the frequency of the nth observed zero crossing and z_n is the nth zero of the Bessel function J_0. This approach has a theoretical advantage, since unlike the multiple filters technique by Yao et al. (2006) described earlier, it does not require the far-field assumption. However, the approach has some caveats, namely that additional or missing zero crossings may exist in real world data, giving an incorrect value of z_n in the above equation. In practice, studies (Boschi et al., 2013) have shown that results from the two methods are similar and that the far-field assumption can be relaxed to a degree (Luo et al., 2015) in the multiple filters technique.

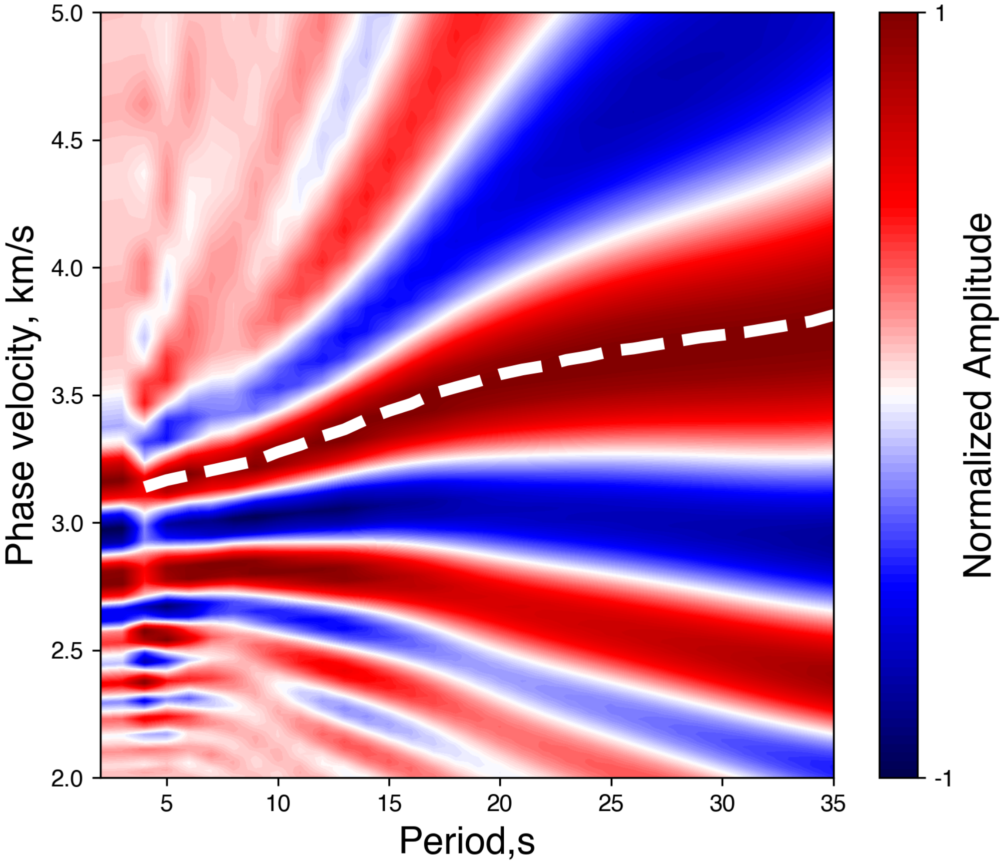

Fig. 2.8 A Velocity - Period image for stations K250 and SYLG. The phase dispersion curve denoted by the white dashed line is automatically picked using a local reference curve.

2.2.3 Group dispersion data from EGFs

Group dispersion data can be obtained from an EGF by using a Frequency Time Analysis (FTAN)(Dziewonski et al., 1969). To achieve this, we compute the envelope of the analytical signal of the EGF and subject it to a series of narrow band pass filters at discrete central frequencies. At each frequency, the path-average group velocity can be measured directly by

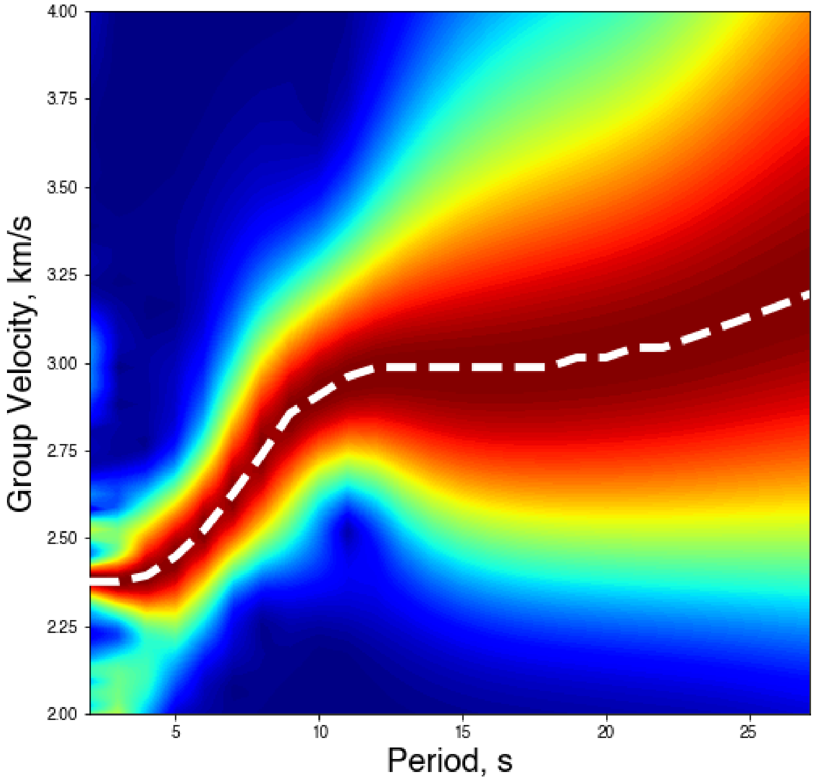

Fig. 2.9 FTAN image from ambient noise correlations for stations BORG and HOT17. The bandpassed filtered signals are combined in a matrix to yield an FTAN image. At each frequency, the travel time can be measured directly by picking the peak of the envelope. The FTAN image can help with the picking of a smooth continuous dispersion curve where several peaks exist in the envelope.

picking the peak of the envelope. The individual filtered signals can be combined in a matrix to yield an FTAN image (Fig. 2.9). This can help pick a smooth continuous dispersion curve where several peaks exist in the envelope. We use an automated code for extracting group dispersion data as described in Pilia et al. (2015).

2.2.4 1D Dispersion data to depth-velocity inversion

Both group and phase dispersion curves are a function of Earth's structure, primarily shear wave velocity. The relationship between surface wave velocities and Earth structure is given by sensitivity kernels (Fig. 2.10), which for a given velocity model, can be used to do the forward calculation to determine dispersion curves, but not the other way around.

Therefore, recovering Earth structure from observed dispersion curves requires an inversion process. The sensitivity kernels themselves are also dependent on Earth structure, making the problem non-linear. We perform the inversion using SURF96 (Herrmann, 2013) which uses a regularized iterative non-linear inversion approach. The parameter space here can be very large and is comprised of two factors, the number of layers and the number of free parameters per layer which are multiplied to give the total number of free parameters. As with any inverse problem a trade-off exists between the number of free parameters and the non uniqueness of the solution.

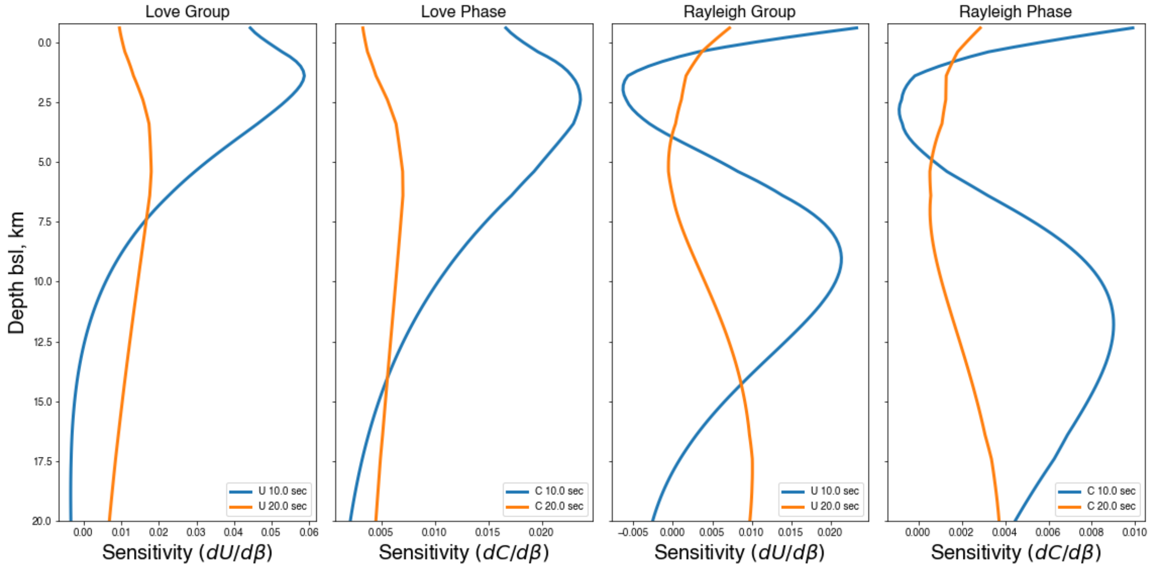

Fig. 2.10 Group and phase sensitivity kernels for Love and Rayleigh waves at periods 10 and 20 seconds calculated using a 1D regional velocity model from Mitchell et al. (2013). β is shear wave velocity. It can be seen that Rayleigh waves have deeper sensitivity than Love waves and that phase velocity has deeper sensitivity than group.

Several approaches exist for choosing the number of layers. (1) Layer thickness is determined according to prior knowledge on interface depth such as refraction data or receiver functions (e.g. Dziewonski and Anderson, 1981). Depending on the availability of such data, and the goals of the work, this approach may or may not be appropriate. (2) Layer thickness is solved for as part of the inversion (e.g. Bodin et al., 2012). While this approach is attractive it also introduces new free parameters (number and thickness of layers) (3) All layers have the same thickness (e.g. Green et al., 2017). This approach was chosen in this work thanks to its simplicity and effectiveness in practical applications.

Regarding the number of free parameters per layer, we use an approach sometimes called pseudo-isotropic inversion, which involves separate inversions of Love and Rayleigh dispersion data for V_{SV} and V_{SH} respectively. To understand the rational behind the pseudo-isotropic inversion process, we must first look into some background on elasticity theory. Surface wave velocity in a given medium is dependent on the medium's density (ρ) and its elastic properties which are given by a 4th rank stiffness tensor which has a size of $3X3X3X3$ and 81 components. For a fully anisotropic medium, the elasticity tensor has 21 independent components out of the possible 81 and can therefore be reduced to a $6X6$ symmetric matrix written as:

$$\{c_{mn}\} = \begin{bmatrix} c_{1111} & c_{1122} & c_{1133} & c_{1123} & c_{1113} & c_{1112} \\ c_{2211} & c_{2222} & c_{2233} & c_{2223} & c_{2213} & c_{2212} \\ c_{3311} & c_{3322} & c_{3333} & c_{3323} & c_{3313} & c_{3312} \\ c_{2311} & c_{2322} & c_{2333} & c_{2323} & c_{2313} & c_{2312} \\ c_{1311} & c_{1322} & c_{1333} & c_{1323} & c_{1313} & c_{1312} \\ c_{1211} & c_{1222} & c_{1233} & c_{1223} & c_{1213} & c_{1212} \end{bmatrix} \tag{2.7}$$

for simplicity this can also be written in Voigt notation as:

$$\{c_{mn}\} = \begin{bmatrix} C_{11} & C_{12} & C_{13} & C_{14} & C_{15} & C_{16} \\ C_{12} & C_{22} & C_{23} & C_{24} & C_{25} & C_{26} \\ C_{13} & C_{23} & C_{33} & C_{34} & C_{35} & C_{36} \\ C_{14} & C_{24} & C_{34} & C_{44} & C_{45} & C_{46} \\ C_{15} & C_{25} & C_{35} & C_{45} & C_{55} & C_{56} \\ C_{16} & C_{26} & C_{36} & C_{46} & C_{56} & C_{66} \end{bmatrix} \tag{2.8}$$

However, inverting for such a large parameter space (21 free components and density) is not feasible. One way to reduce the number of free parameters is to assume Vertical Transverse Isotropy (VTI), in which the material properties are identical in all horizontal directions. This assumption is reasonable since there is no notion of azimuth in the inversion of dispersion data for 1D structure. A transversely isotropic material can be characterized by only 6 free parameters (Love, 1892): ρ, A, C, F, L and N:

$$\{c_{mn}\} = \begin{bmatrix} A & A2N & F & 0 & 0 & 0 \\ A2N & A & F & 0 & 0 & 0 \\ F & F & C & 0 & 0 & 0 \\ 0 & 0 & 0 & L & 0 & 0 \\ 0 & 0 & 0 & 0 & L & 0 \\ 0 & 0 & 0 & 0 & 0 & N \end{bmatrix} \tag{2.9}$$

A, C, F, L and N can be substituted for V_{SV}, V_{SH}, V_{PV}, V_{PH} and η using:

$$A = \rho V_{PH}^2 \tag{2.10}$$

$$C = \rho V_{PV}^2 \tag{2.11}$$

$$L = \rho V_{SV}^2 \tag{2.12}$$

$$N = \rho V_{SH}^2 \tag{2.13}$$

$$F = \eta\rho\left(V_{PH}^2 - 2V_{SV}^2\right) \tag{2.14}$$

V_{PH} and V_{PV} are the horizontally and vertically traveling P waves respectively and η is used for parametrization and has no simple physical meaning. Assuming VTI therefore reduces the number of free parameters significantly to 6 (5 free components and density). However, this is still a very large parameter space when multiplied by the number of layers in the model. While some studies use this parametrization (e.g. Nishimura and Forsyth, 1989) and invert Love and Rayleigh data simultaneously, the large parameter space results in significant non-uniqueness. To resolve this, other restrictions are often imposed on the model such as prior information or using relatively thick layers (low resolution).

Another common approach, which is used in this thesis, is to invert Love and Rayleigh dispersion data independently assuming that Love is only sensitive to V_{SH} and Rayleigh is only sensitive to V_{SV}. This approach is sometimes called pseudo-isotropic inversion since for each of the two separate inversions we can use an isotropic parametrization. If we assume isotropy, the elasticity tensor can then be fully described using two free parameters, λ and μ:

$$\{c_{mn}\} = \begin{bmatrix} \lambda+2\mu & \lambda & \lambda & 0 & 0 & 0 \\ \lambda & \lambda+2\mu & \lambda & 0 & 0 & 0 \\ \lambda & \lambda & \lambda+2\mu & 0 & 0 & 0 \\ 0 & 0 & 0 & \mu & 0 & 0 \\ 0 & 0 & 0 & 0 & \mu & 0 \\ 0 & 0 & 0 & 0 & 0 & \mu \end{bmatrix} \tag{2.15}$$

λ and μ are related to V_S, V_P using the following equations:

$$\lambda = \rho \left(V_P^2 - 2V_S^2\right) \tag{2.16}$$

$$\mu = \rho V_S^2 \tag{2.17}$$

This is a more manageable parameter space (2 components + density). However, SURF96 reduces it further to one free parameter by only solving for V_S. At each iteration V_P is calculated from V_S using the initial V_P/V_S ratio and density is calculated from V_P using Nafe–Drake relation (Nafe and Drake, 1963). We are therefore left with only one free parameter per model layer. This approach is widely accepted since the sensitivity of surface waves to V_P and density is far smaller than the sensitivity to V_S.

To sum up this section so far, we use a few assumptions/simplifications in order to reduce the parameter space from 22 per model layer, to only one (V_S) per model layer:

- We assume VTI which reduces the number free parameters from 22 to 6. This is justified since we are dealing with 1D structure without a notion of azimuth
- We assume Love and Rayleigh dispersion can be inverted separately for V_{SH} and V_{SV} which reduces the number free parameters from 6 to 3 per layer but involves an additional inversion. This is justified since Love is mostly sensitive to V_{SH} and Rayleigh is mostly sensitive to V_{SV}.
- SURF96 assumes that V_P can be calculated from V_S and that ρ can be calculated from V_P which leaves us with only one free parameter. This is justified since the sensitivity of surface wave velocities to V_S is far greater than to the other parameters.

While we significantly reduce non-uniqueness using these simplifications, it nonetheless persists, as in most geophysical inverse problems. This can be mitigated by using multiple starting models for the inversion, which can provide insight into whether multiple minima are present in model space, given a reasonable range of initial models (e.g. Fishwick et al., 2005;

Russell et al., 2019; Lin et al., 2016). Specific details of the ensemble of starting models used is provided within each chapter.

Out of these three widely used simplifications the most commonly contested is the second one, since Love and Rayleigh waves are not strictly only sensitive to V_{SH} and V_{SV} respectively and that V_{PH}, V_{PV} and η and can be neglected, especially in the presence of radial P wave anisotropy (Anderson, 1965; Dziewonski and Anderson, 1981). Most importantly, this can lead to the values of S wave anisotropy being overestimated (Anderson, 1965; Dziewonski and Anderson, 1981). We further discuss this issue in greater detail in section 3.3.5 in the context of our results and how it may affect them. Another problem with this approach is that the depth sensitivity of Love and Rayleigh waves are different. As shown in Fig. 2.10, for similar periods, Rayleigh waves are sensitive to deeper structure. This means that at large depths where Love sensitivity decreases, it is possible that the resulting V_{SH} model is mostly a function of the starting model, and of the data. This is important since in the next step we use both the V_{SV} and V_{SH} models to calculate radial anisotropy. There are two ways in which we mitigate this issue. First, as mentioned above, we use an ensemble of starting models for the inversion and examine the ensemble of resulting models. If the radial anisotropy results are highly affected by the change in the starting model, this would manifest as large variability in the resulting models. Second, we avoid interpreting our results at depths where the V_{SH} models are similar to the inversion starting models - in chapter 3 for example, we avoid interpreting our results in the mantle.

2.2.5 Using Group vs Phase velocity

Phase velocity measurements are preferable to group for several reasons. First, the uncertainty in picking phase velocity dispersion curves is smaller compared to group velocity (Lin et al., 2008; Bensen et al., 2007; Luo et al., 2015). This was demonstrated by Lin et al. (2008) using a method based on analyzing thousands of nearly linearly aligned station-triplets. Luo et al. (2015) attributed the higher uncertainty of group velocity measurements to the picking of the peak of the wide waveform envelope. Second, for similar periods, phase velocity has a deeper sensitivity (Fig. 2.10) and, therefore, can constrain deeper velocity structures. Third, group velocity dispersion curves can be calculated from phase velocity dispersion curves, but not the other way around. Finally, group dispersion measurements rely on amplitude information. As mentioned earlier, the EGF's amplitude may differ from that of the real Green's function (Yao et al., 2006). Therefore we use phase velocity where possible, i.e. in chapters 3 and 5. However, group velocity has the advantage of being easier to measure at shorter periods, which are important for local shallow investigations. We therefore use group velocity in chapter 4 which deals with the shallow velocity structure and anisotropy of Askja volcano, as is commonly done in volcano seismology applications (e.g. De Siena et al., 2018; Obermann et al., 2016; Brenguier et al., 2007; Masterlark et al., 2010).

2.2.6 2D Ambient noise tomography

Measuring surface wave dispersion using ambient noise often leads to a very dense ray-path coverage of the study area. We invert the group and/or phase travel times for 2D group and/or phase velocity maps using the Fast Marching Surface Tomography (FMST) package (Rawlinson and Sambridge, 2005) which has been used widely for inverting surface waves data from ambient noise (e.g. Stankiewicz et al., 2010; Nicolson et al., 2012; Mottaghi et al., 2013). FMST is an iterative non-linear travel time tomography solver in 2D spherical coordinates. FMST has two important user-defined parameters called damping and smoothing. These are important to prevent the inversion from over fitting the data and producing a suitably parsimonious model. The objective function minimized by the inversion is:

$$S(m) = (g(m) - d_{obs})C_d^{-1}(g(m) - d_{obs})^T + \varepsilon(m - m_0)C_m^{-1}(m - m_0)^T + \eta m^T D^T D m \quad (2.18)$$

where m are the model parameters, d_{obs} are the observed traveltime residuals, $g(m)$ are the predicted traveltime residuals, m_0 is the initial model, C_d^{-1} is the *a priori* data covariance matrix, C_m^{-1} is the a priori model covariance matrix, D is the smoothness matrix, ε is the damping parameter and η is the smoothing parameter. Damping imposes a “cost” to perturbing the starting model during the inversion, so that higher damping values should result in a model that is more similar to the starting model. The reasoning behind introducing damping is to make sure that the data actually requires perturbations to be made to the prior information in order to be satisfied. Smoothing controls the level of detail or roughness of the model, with the basic principle being that the simplest model that satisfies the data is the best. These so-called regularization parameters are usually determined empirically using an L-curve process. In this process, the inversion is attempted using various values of damping or smoothing, and the value closest to the “knee” of the L is chosen as the optimum trade-off between fitting the data, the size of the model model perturbation and model smoothness. This is often done separately for damping and smoothing while keeping the other parameter constant (e.g. Rawlinson et al., 2010).

2.2.7 Pseudo 3D ambient noise tomography

Since surface waves sample the velocity structure at different depths along their path, it is possible to invert dispersion data for a 3D shear velocity where dense data coverage exists. While this would be possible to do using a single 3D model for the domain, the computation time would be very long. Montagner (1986) suggested a process to parallelize this inversion, commonly know as the two step inversion method. In the two step method the inversion process for 2D group/phase velocity maps described in the previous section is performed separately for each period. Next, pseudo dispersion curves are extracted at a predefined set of grid points that span the model and inverted for shear wave velocity as a function of depth. Finally, all the 1D velocity profiles are assembled in a pseudo 3D shear velocity model. This approach is attractive since it is can be easily parallelized (Zhang et al., 2018). Montagner (1986) demonstrated this using surface waves from earthquakes for the upper mantle in the Indian ocean (Fig. 2.11). With ambient noise, this approach has been demonstrated in various settings (e.g. Pilia et al., 2015; Green et al., 2017; Obermann et al., 2016; Brenguier et al., 2007). The disadvantage of this approach is that since different pseudo dispersion curves are inverted separately, this process does not preserve the full information about lateral spatial correlations (Zhang et al., 2018; Fang et al., 2015). Despite this drawback, the two step inversion can still be used to gain valuable information as demonstrated in numerous works. Recently, advances have been made towards the use of a single step inversion, where the predicted dispersion curves are calculated directly from a 3D shear velocity model. This approach has been demonstrated with synthetic data (Zhang et al., 2018) and applied in the imaging of a gas reservoir (Zhang et al., 2020), but has yet to gain widespread adoption .

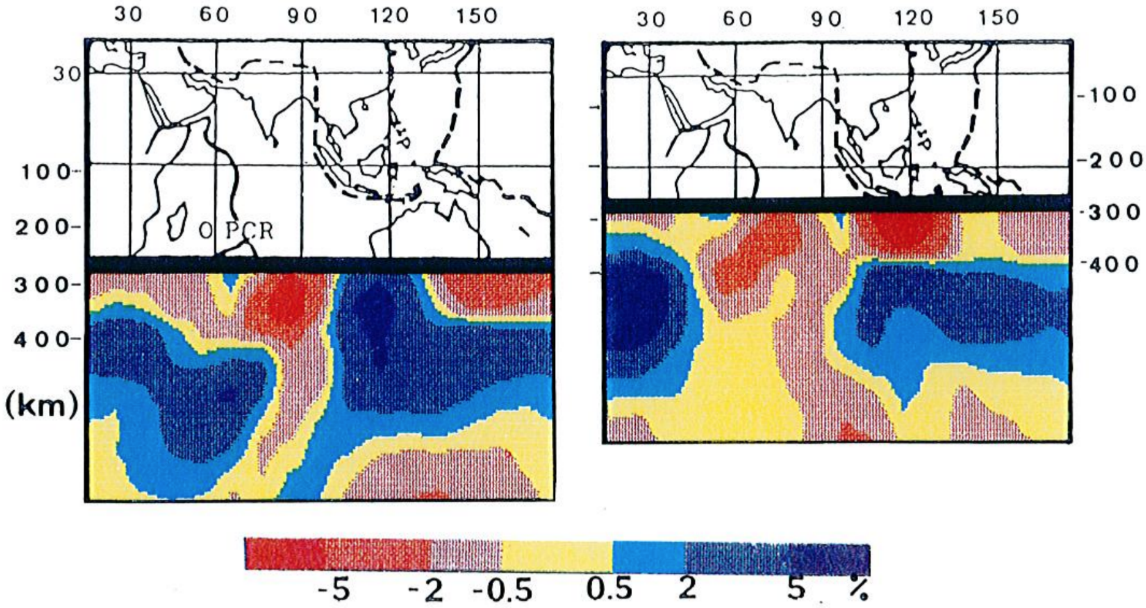

Fig. 2.11 E-W Cross sections of the shear velocity structure beneath the Indian Ocean and neighbouring areas from Montagner (1986) produced using the two-step method. Colours indicates percent perturbation to the inversion starting model.

Chapter 3

Oceanic Crustal Flow in Iceland Observed using Seismic Anisotropy

The work presented in this chapter has been published in:

Volk, O., White, R.S., Pilia, S., Green, R.G., Maclennan, J. and Rawlinson, N. (2021) Oceanic crustal flow in Iceland observed using seismic anisotropy. *Nature Geoscience*, 14(3), pp.168-173.

and is therefore presented in a nature format with methods and implementation details at the end. In terms of author contributions to this article, I conceived the study, undertook all the data processing and modelling, and wrote the manuscript. The co-authors provided various advice along the way, and made editing suggestions to the manuscript prior to submission and during the review process.

3.1 Chapter abstract

Understanding accretion and deformation processes at mid-ocean ridges is crucial as they control the resulting oceanic crustal structure, which covers two-thirds of Earth's surface. The most common tool for observing such dynamic processes within the Earth is seismic anisotropy. Iceland, which is uplifted by a convective mantle plume and has an active spreading ridge system exposed above sea level, offers a unique opportunity for studying this phenomenon. Here we use a high-resolution dataset of Love and Rayleigh wave speeds to constrain the seismic anisotropy in the Icelandic crust. We show that seismic anisotropy in the lower crust is controlled by crystal preferred orientation, providing a direct observation of

lower crustal flow. Furthermore, since shear is needed to align the crystals, our result reveal that crustal flow cannot be a simple translation of mass and requires internal deformation. This finding has important implications for how thick, hot oceanic crust, as found in volcanic rifted margins and near plume-ridge interactions, can accrete and deform.

3.2 Main

3.2.1 Introduction

The formation of oceanic crust at mid-ocean spreading ridges is one of the fundamental processes of plate tectonics. The structure of mid-ocean ridges is largely known from marine seismic experiments and from field observations of ophiolites around the world. However, since spreading ridges are usually found under deep water, data from seismic instrumentation remains limited when compared to more accessible continental plate boundaries. Furthermore, while ocean bottom seismometers can collect valuable data, the quality is sometimes lessened compared to onshore instruments (Duennebier and Sutton, 1995; Mangano et al., 2011). Iceland, which straddles the mid-Atlantic Ridge and is uplifted by a convective plume (White and McKenzie, 1989; Darbyshire et al., 1998) in the underlying mantle, has an active spreading ridge system exposed above sea level. It therefore represents a unique opportunity for studying oceanic crustal formation, spreading ridge dynamics and plume-ridge interaction.

The structure of the oceanic crust in Iceland, and of the lower crust in particular, has been debated by researchers ever since the first seismic experiments on the island. Unlike normal oceanic crust which displays a roughly uniform thickness of $\sim$7 km (White et al., 1992), crustal thickness in Iceland is highly variable (Brandsdóttir et al., 1997; Staples et al., 1997; Darbyshire et al., 1998; Allen et al., 2002; Jenkins et al., 2018) and changes from $\sim$20 km in the Northern and Western Volcanic Zones, to more than 40 km above the center of the mantle plume under the Vatnajökull icecap (Fig. 3.1). This variability is attributed to increased melt generation above the narrow (c. 100 km diameter) central stem of the upwelling mantle plume (Darbyshire et al., 1998; Jenkins et al., 2018) and to a series of successive eastward rift jumps into thick older crust (Hardarson et al., 1997; Staples et al., 1997). Additionally, active source experiments (Pálmason, 1971; Staples et al., 1997; Darbyshire et al., 1998) have constrained compressional velocities in the lower crust of $\sim$7.2 km/s, which are unusually high compared to normal oceanic crust. Recently, a study (Jenkins et al., 2018) using receiver functions and Rayleigh wave dispersion data reported a significant mid-crustal discontinuity at $\sim$20 km: petrological modelling was used to suggest that the crust is made of alternating layers of gabbroic and olivine-rich cumulates below this discontinuity and only gabbro above it. Research using gravity measurements (Gudmundsson, 2003) showed that the lower crust in Iceland is 200 kg/m^3 denser than its counterpart beneath adjacent ridges and similarly argued for an olivine enriched lower crust.

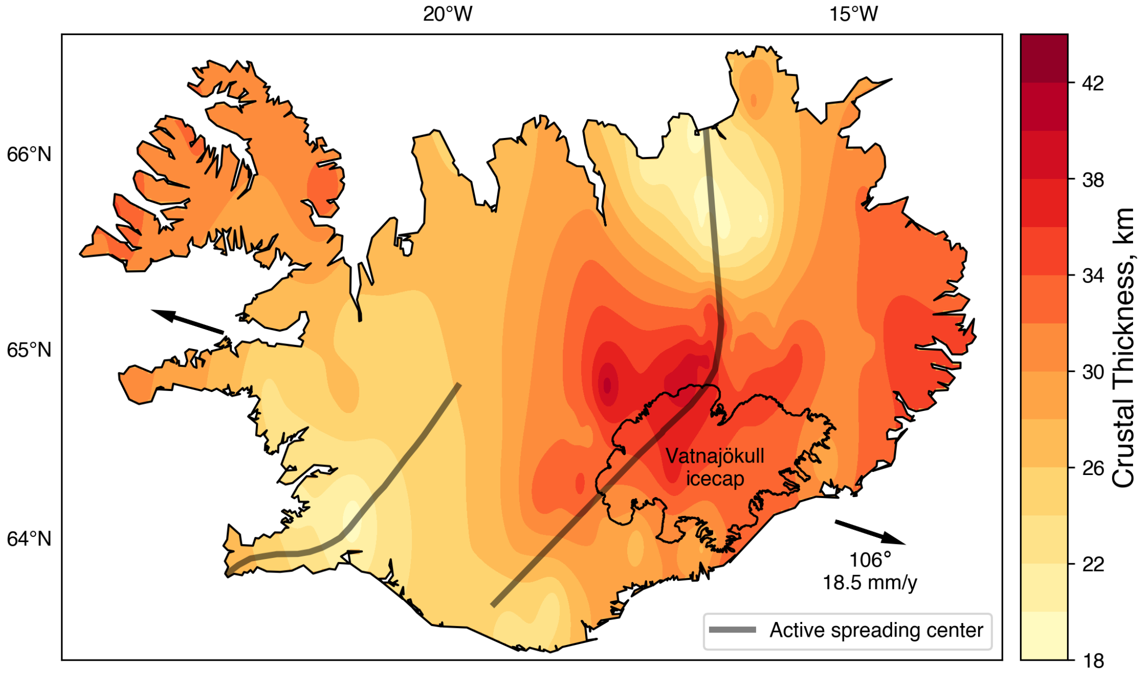

Fig. 3.1 Crustal thickness based on Jenkins et al. (2016) is shown as colored contours. Grey lines denote the location of active spreading centers. Thin black line shows the outline of Vatnajökull icecap roughly corresponding to the estimated location of the plume head. Black arrows indicate the spreading direction of 106° with a full spreading rate of 18.5 mm/yr.

The ridge in Iceland is a slow spreading ridge with an extension direction of 106° and a spreading rate of 18.5 mm/y (DeMets et al., 2010). The crust is relatively hot, with regional geothermal gradients of 40 - 50°C/km (Flóvenz and Saemundsson, 1993) and a shallow seismogenic depth of $\sim$7 km, below which it undergoes ductile deformation (flow). While the brittle deformation in the upper crust can be observed directly using earthquakes, or at the surface in the form of vertically oriented fractures and faults in fissure swarms (Hjartardóttir et al., 2016), the style of deformation in the lower crust can only be inferred by lack of seismicity. The most common way to investigate flow within the crust is using seismic anisotropy, as demonstrated by works showing continental crustal flow in Tibet (Shapiro and Campillo, 2004; Duret et al., 2010). Most studies of seismic anisotropy (Bjarnason et al., 2002; Li and Detrick, 2003) in Iceland, however, have focused on the mantle. Research using relative surface wave arrival times from regional earthquakes (Bjarnason and Schmeling, 2009) had previously suggested that radial anisotropy exists in parts of the lower crust in

Iceland. However, the authors acknowledged the poor azimuthal coverage of their data, which prevented a decisive interpretation. Despite the progress made, until the work presented here, no studies of anisotropy in the Icelandic crust with significant azimuthal coverage have been conducted.

3.2.2 Observed radial anisotropy in the crust

We determine the path average velocity for vertically (V_{SV}) and horizontally (V_{SH}) polarized shear waves for 75 inter-station paths (Fig. 3.2) across Iceland by extracting Love and Rayleigh phase velocity dispersion curves (Fig. 3.4) from ambient noise (Yao et al., 2006; Bensen et al., 2007) cross correlations (Fig. 3.3 and invert them for V_{SH} and V_{SV} respectively (Herrmann, 2013) (Fig. 3.5a). We then compute radial anisotropy (Fig. 3.5b) as $\xi = (V_{SH}/V_{SV})^2$. The terms positive and negative radial anisotropy are used to describe $\xi > 1$ ($V_{SH} > V_{SV}$) and $\xi < 1$ ($V_{SH} < V_{SV}$) respectively. The assumption that Love and Rayleigh waves are only sensitive to V_{SH} and V_{SV} respectively is not strictly correct (Anderson, 1965; Dziewonski and Anderson, 1981) and may result in the strength of anisotropy being overestimated. However, as further discussed in the Methods section, we feel that this assumption – which is widely used – does not unduly influence our findings.

The anisotropy profiles (Fig. 3.5b) inverted from the average dispersion curves display $\xi < 1$ in the brittle crust near the surface, while in the lower ductile crust, from $\sim$15 to 35 km depth, we observe $\xi > 1$. The smoothing character of surface waves makes it hard to know the exact nature of the transition between $\xi < 1$ and $\xi > 1$. Below $\sim$40 km depth the sensitivity of Love waves decreases to the point where a reliable interpretation is no longer possible. It should be noted that we initially attempted to invert Rayleigh and Love dispersion curves simultaneously assuming an isotropic velocity structure, but found that no isotropic model could satisfy the data (Fig. B.1).

While not the focus of this work, $V_{SH} < V_{SV}$ in the upper crust is attributed to the presence of vertically oriented cracks and dykes (Dunn and Toomey, 2001; Barclay and Toomey, 2003). This is consistent with the observed extension of brittle crust by plate spreading and the intrusion of dykes in the neo-volcanic rift zones (White et al., 2011; Sigmundsson et al., 2015).

There are two possible explanations for the observation of $V_{SH} > V_{SV}$ in the lower crust: (1) Thin Periodic Layering (TPL) where two or more isotropic materials with different velocities form a geological unit comprising alternating layers with thicknesses that are significantly smaller than the observed seismic wavelength (Backus, 1962) (e.g., sills of different compositions). Layering has been observed in exhumed oceanic crust (Jousselin et al., 2012) and has been suggested as the cause of radial anisotropy (Bjarnason and

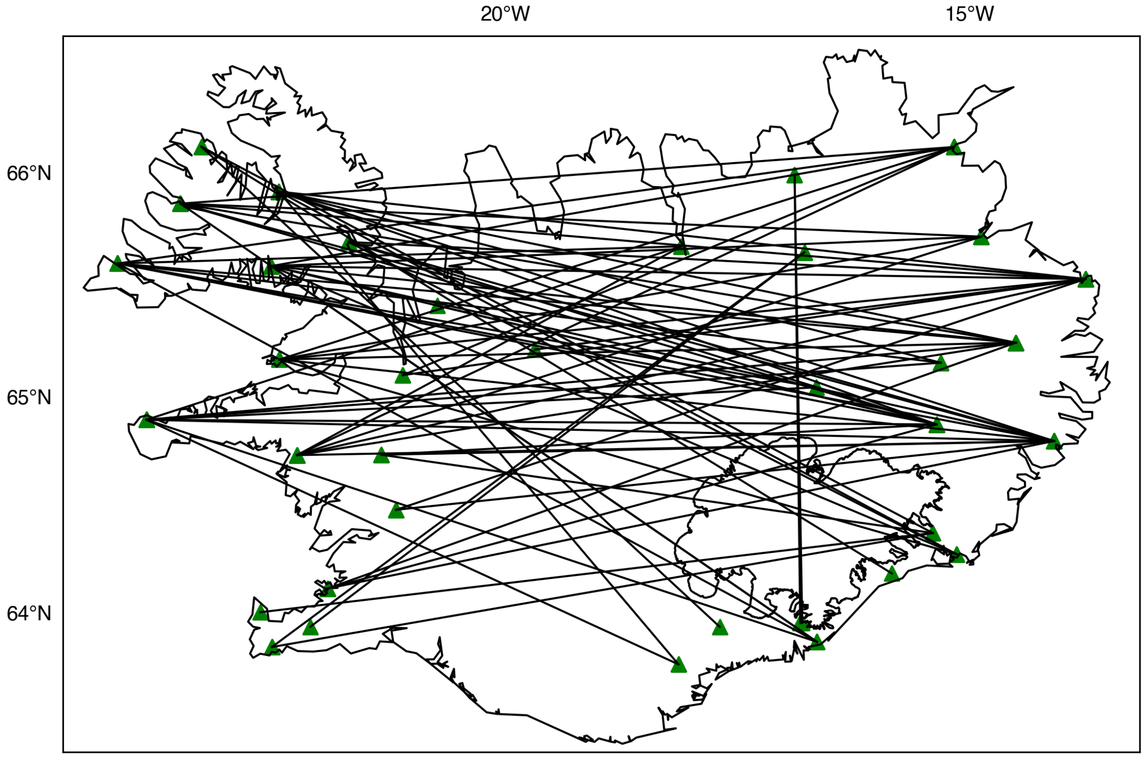

Fig. 3.2 75 inter station paths across Iceland used in this work. Green triangels are broadband seismometers installed in vaults.

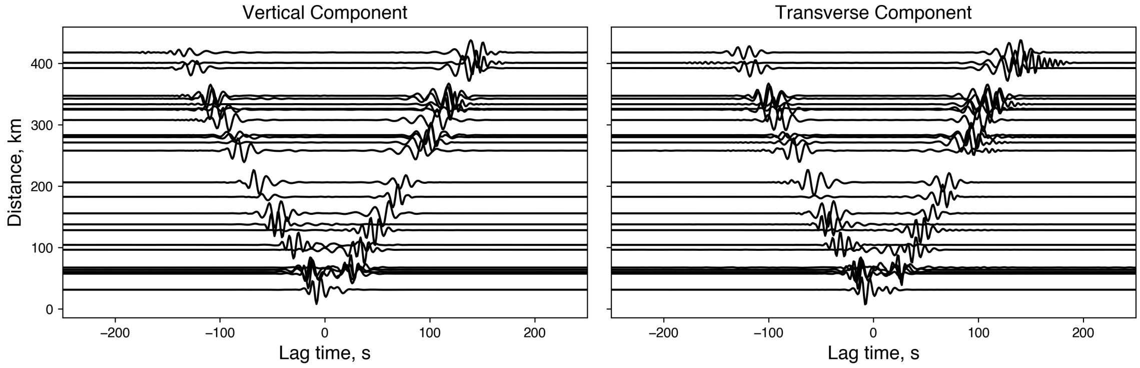

Fig. 3.3 Noise cross correlation functions extracted from the vertical and transverse components for all station pairs that include HOT24 display a typical move out pattern. The NCFs are bandpass-filtered between 10 - 60 s. The vertical component arrivals represent Rayleigh waves and the transverse component arrivals represent Love waves.

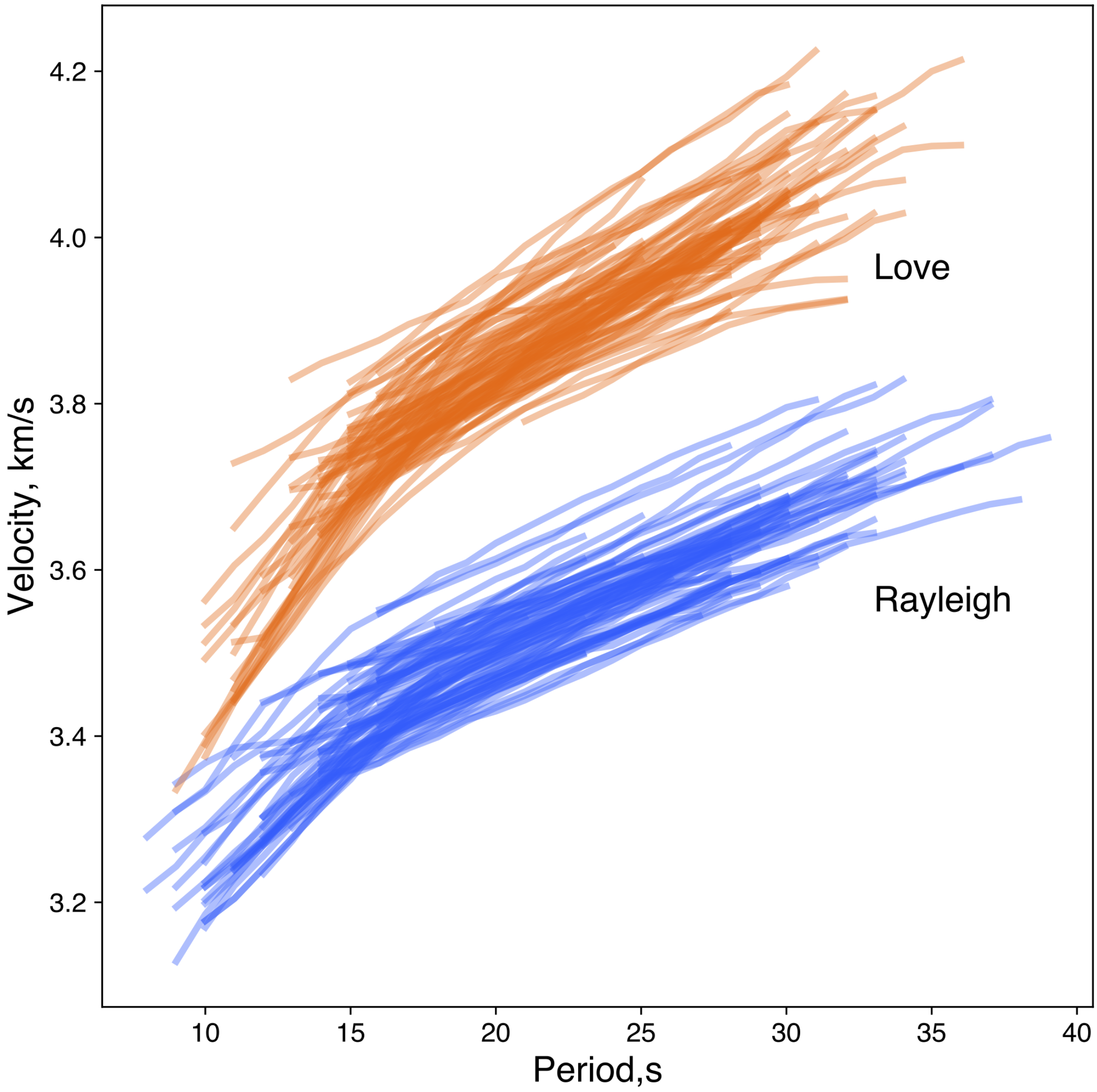

Fig. 3.4 Measured phase velocity dispersion curves of fundamental mode Love and Rayleigh waves for the 75 paths shown in the inset map on Figure 3.2

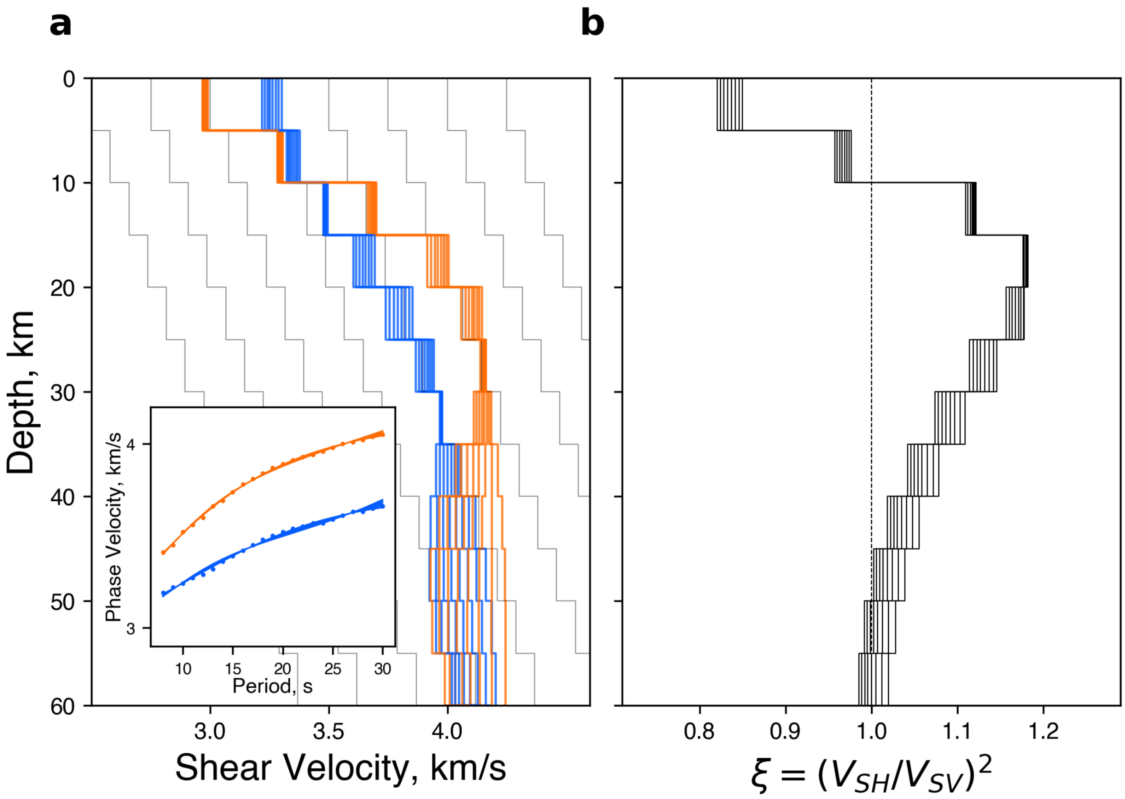

Fig. 3.5 **a** Grey lines show the starting models used in the inversion of Rayleigh dispersion data for V_{SV}. Blue lines show the resulting V_{SV} models (one for each starting model) which in turn are used as starting models in the inversion of Love dispersion data for V_{SH} . The resulting V_{SH} models are shown as orange lines. The inset shows the observed (dots) and fitted (solid lines) dispersion curves for Rayleigh (blue) and Love (orange) waves used in the inversion. **b** Radial anisotropy (ξ) vs depth. Different lines show the results from different starting models. The dashed line represents a radially isotropic model. The process is repeated for each station pair. The example shown in this figure is for the regional average dispersion curve (i.e based on all the available inter-station dispersion management).

Schmeling, 2009; Russell et al., 2019). Such a structure would manifest as radial anisotropy which does not change with the azimuth of propagation (Fig. 3.6a–b), also called Vertically Transverse Isotropy (VTI). (2) Lattice Preferred Orientation (LPO), which involves the alignment of crystals in a preferred orientation. Where anisotropic minerals are present and aligned over a large region comparable to the seismic wavelength, they produce large-scale anisotropy which would be observed as a change in the propagation velocity of seismic waves as a function of orientation. Unlike TPL, the preferred alignment of crystals could result in a dependence of ξ on azimuth. For example, the alignment of olivine with type A fabric due to flow with a vertical flow plane, could manifest itself as ξ that is low parallel to the flow direction and increases with azimuth away from it (Bastow et al., 2010) (Fig. 3.6c-d). An additional mechanism that is suggested to be able to produce radial anisotropy with azimuthal variations is oriented melt pockets (Bastow et al., 2010) or OMP. However, we do not consider it likely to be a significant contributor to anisotropy in the lower crust since there is no evidence of prominent vertical structure in lower oceanic crust exposed in ophiolites. Although sub-vertical dykes are present in the upper third of oceanic crust (Layer 2), the dominant structure in the lower crust (Layer 3) is sub-horizontal, probably due to melt storage and differentiation in sills. Furthermore, the observed radial anisotropy for OMP is expected to be strongly negative (V_{SV} faster than V_{SH})(Bastow et al., 2010) which is not what we observe.

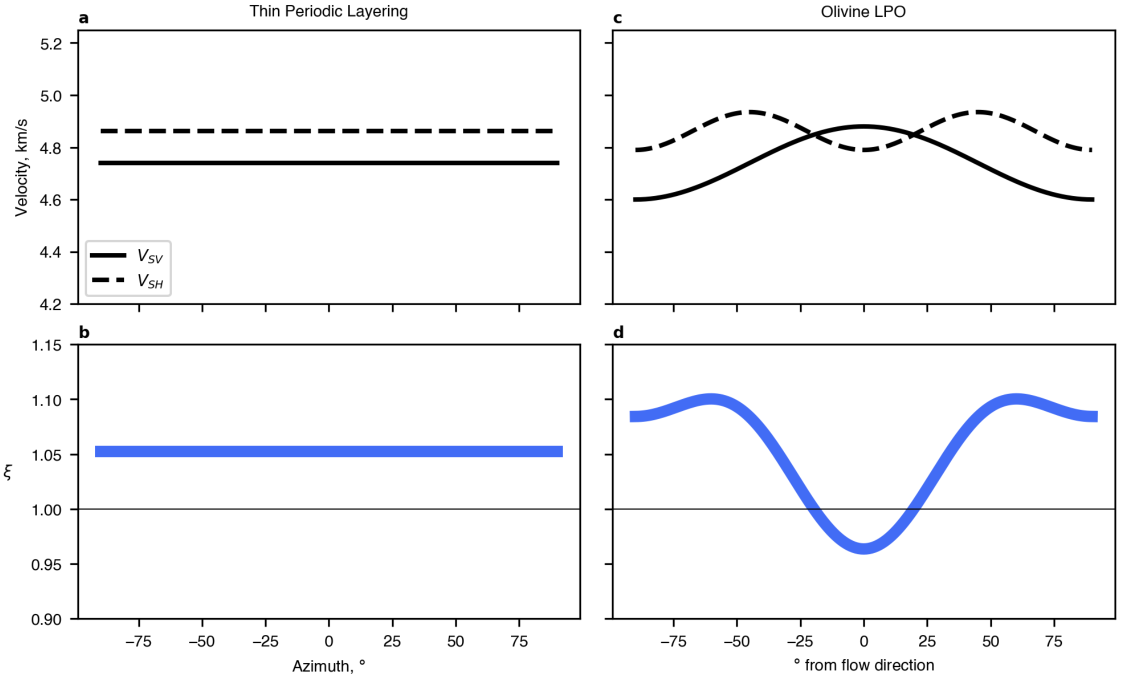

Fig. 3.6 Schematic diagram showing the expected radial anisotropy vs azimuth of different mechanisms. **a-b** Thin periodic layering can produce positive radial anisotropy with Vertical Transverse Isotropy (VTI), i.e. no correlation between radial anisotropy and azimuth. **c-d** Flow induced Lattice Preferred Orientation (LPO) of olivine crystals, can produce positive radial anisotropy with azimuthal variations. Velocities in **c** are taken from Bastow et al. (2010)

3.2.3 Observed azimuthal variations in radial anisotropy

We test for azimuthal variations by plotting ξ versus back azimuth for each station pair, fitting the data with a 2θ sinusoid (Fig. 3.7) and using an F-test to determine whether the sinusoid fits the data significantly better than a random distribution about a mean. We also fitted a $2\theta + 4\theta$ sinusoid but F-tests showed that the improvement in fit was not justified by the data. Focusing on ξ rather than V_{SV} and V_{SH} separately has the advantage of reducing the contribution of regional variations in the isotropic velocities.

In the brittle crust (Fig. 3.7a), while we see large scatter in the data, an F test shows that the sinusoid fit is significant. The sinusoid fit suggests that ξ is highest parallel to the spreading direction and decreases away from it, as expected for vertically oriented cracks and dykes striking perpendicular to the extension direction. This is consistent with observations of shear wave splitting from local earthquakes showing a fast splitting direction parallel to the strike of the rift (Bacon et al., 2019). We attribute the large scatter to the heterogeneity of the upper crust and the period range ($\sim$10 – 40 s) used in this work.

In the lower ductile crust, from 20 to 25 km depth (Fig. 3.7b), we observe a clear dependence of radial anisotropy on the propagation direction and an F test shows that the fit is highly significant ($p < 0.01$). The radial anisotropy is smallest around azimuths of $\sim$100° - 110°, which is similar to the spreading direction, and increases away from it. To further validate this, we divide our data points into two groups, spreading-parallel (angle to spreading <45°) and spreading-perpendicular (angle to spreading >45°) and use a T test to demonstrate that the difference in mean of the two groups is statistically significant with very high confidence ($p < 0.01$). The azimuthal variation clearly indicates that anisotropy cannot be attributed to TPL alone and that LPO is required to explain the observation. We note that while layering alone cannot explain our observation in the lower crust, it is possibly present and contributes an azimuth-independent increase in radial anisotropy.

At depths of 35 - 40 km (Fig. 3.7c) we do not observe any significant trends and F tests show that the periodic functions do not fit the data better than a random distribution about a mean. This may be due to complication near the Moho under most of Iceland, but may also be attributed to decreased sensitivity of our data at these depths.

3.2.4 LPO in the lower crust

The azimuthal alignment of crystallographic axes over large regions requires the presence of shear. However, the type of fabric formed in response to shear may change depending on several factors including composition, shear mechanism and the presence of other phases. Studies of the upper oceanic mantle usually interpret observed azimuthal variations in velocity

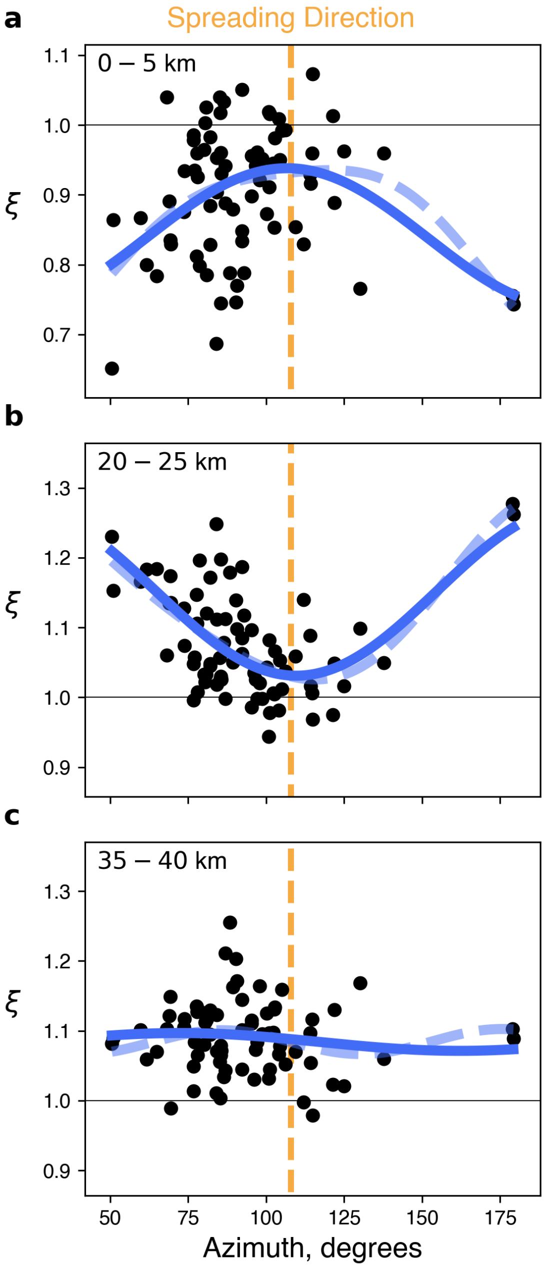

Fig. 3.7 In all panels black dots indicate the radial anisotropy measured for different station pairs. Each dot is the mean of the ensemble of different inversion results from using different starting models. Blue solid and dashed lines show the best fitting 2θ and $2\theta + 4\theta$ sinusoids respectively. **a** In the uppermost crust, despite data scatter, the data fit suggests that radial anisotropy is weak parallel to the spreading direction and becomes strongly negative away from it. **b** In the lower crust we clearly observe $\xi > 1$ which changes with azimuth and the direction of minimal anisotropy is similar to the spreading direction. **c** at depths of 35 - 40 km we observe $\xi > 1$ with no significant correlation with azimuth. All panels have the same vertical-horizontal aspect ratio. Uncertainties are presented in Figure 3.11. Additional depths are presented in Figure 3.17.

as LPO of olivine with the fast axes parallel to the lineation (i.e., flow direction), and attribute the shear to velocity gradients due to corner flow near spreading ridges (Ismaïl and Mainprice, 1998; Blackman et al., 2002; Blackman and Kendall, 2002; Long and Becker, 2010). Unlike the mantle, the composition of the lower crust in Iceland is not as well constrained and is thought to be more heterogenous. As discussed earlier, the crust at these depths is expected to consist of a mix of gabbroic and olivine-rich cumulates. The azimuthal variations we observe could therefore be explained by LPO in olivine cumulates.

While olivine LPO is sufficient to explain our observation, plagioclase and clinopyroxene, which are common in gabbro, can also be highly anisotropic at the single crystal level. The effect of deformation of multiphase rocks, such as gabbro, on fabrics and seismic properties is hard to analyze and the experimental data on deformed gabbro remains limited compared to olivine. Furthermore, while olivine is orthorhombic, plagioclase and clinopyroxene have lower symmetries triclinic and monoclinic respectively which creates additional degrees of freedom in producing CPO. An analysis (Jousselin et al., 2012) of deformed gabbro samples from the Moho transition zone in the Oman ophiolite found that some samples had a significant azimuthal alignment of plagioclase [100] axes with the shear direction (Fig. 3.8). Another study (Satsukawa et al., 2013) which analyzed the largest database yet of CPO in plagioclase bearing rocks, including gabbro, showed that while azimuthal alignments were present in some plastically deformed samples, the shear wave anisotropy pattern was highly scattered and had a relatively complex relation to the foliation. The study concluded that the presence of multiple phases in gabbro would generally reduce seismic anisotropy by destructive interference. It is therefore difficult to determine the exact contribution of gabbro deformation to our observation. In fact, since the anisotropy values we see are high compared to previous studies of olivine anisotropy in the mantle, and assuming they are not overestimated due to modelling limitations, it is reasonable to assume that the highly anisotropic minerals in gabbro are likely to be involved. Nevertheless, even if we are uncertain of the relative proportions of anisotropic minerals, LPO is required to explain our observation and so is shear.

Generating shear not only requires flow but also a velocity gradient within the layer that flows. Models of oceanic crust formation which include corner flow have been suggested previously and would induce such a velocity gradient, but have been found to be unlikely (Korenaga and Kelemen, 1998). A different mechanism to generating a velocity gradient is density induced flow, which has also been suggested in Iceland (Jones and Maclennan, 2005; Bjarnason and Schmeling, 2009). Such flow would be fastest in the deepest parts of the crust and slower at shallower depths. While this process might be taking place, it would probably not result in our observation, since flow modelling (Jones and Maclennan, 2005) suggests

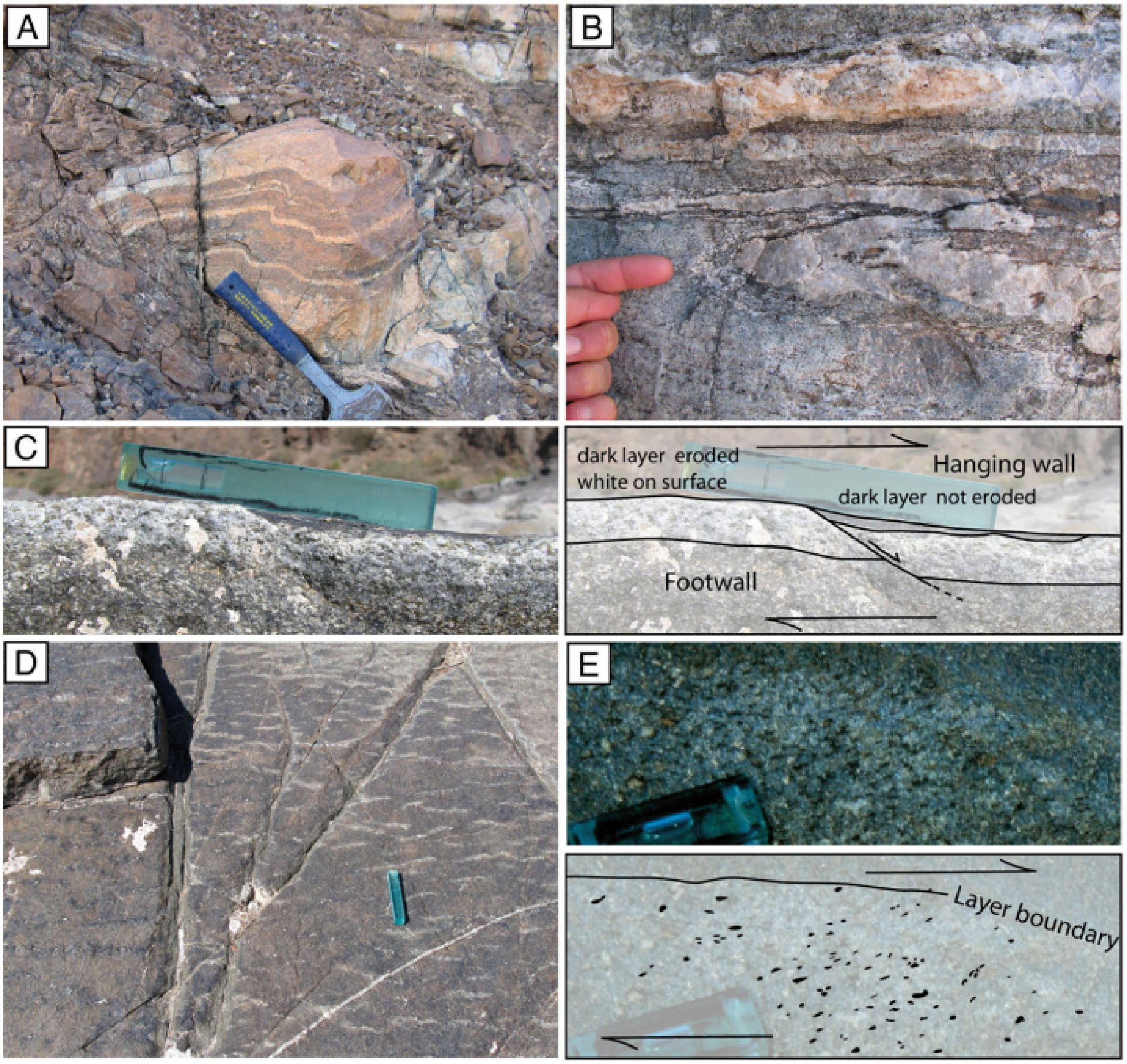

Fig. 3.8 Kinematic indicators of simple shear in layered gabbro lensesfrom Jousselin et al. (2012). **a–b**) Asymmetrical folds; as is the case for strong deformation, fold axes are rotated parallel to the lineation direction. **c–d**) Normal shear zones in cross-section and planar view. The planar view shows the consistent orientation of the shear plane, and the cross-section view explains the color variations in map view induced by the movement at the shear zone. **e**) Close-up view on a layer with olivine crystals at a consistent angle to the layering.

that it only takes place in a small region along the northern rift zone where crustal thickness gradients and temperatures are highest. Another possible mechanism is shear between the olivine and gabbro cumulates. Since the different cumulates have different viscosities they will respond to extension at different rates. This type of shear has been observed clearly in the Moho transition zone of the Oman ophiolite where gabbro lenses are found in host dunite and resulted in significantly lineated crystallographic fabrics (Jousselin et al., 2012). Such shear could match our observation. Another possible mechanism for a velocity gradient in lower crustal flow which would match our observation is a flow velocity increase with depth. In this scenario, flow is slowest near the cold brittle-ductile transition where no flow takes place, and accelerates away from it.

While we have established that crustal flow is required, discussing the direction of flow requires speculation as to which is the dominant fabric creating anisotropy. If we assume that the olivine LPO style used earlier (Fig. 3.6c–d) is the dominant one, then our observation could be explained by flow parallel to the spreading direction (Bastow et al., 2010). However, further flow modelling and laboratory data regarding gabbro deformation is required to exclude other possible flow regimes.

Figure 3.9 displays a schematic summary of our interpreted mechanisms for seismic anisotropy in the Icelandic crust. Although it is hard to know exactly which mineral fabrics contribute to the overall anisotropy pattern, the alignment of olivine and possibly additional phases in the ductile crust remains the most plausible interpretation of our observation. The presence of LPO reveals that lower crustal flow in Iceland is not a simple translation of crustal mass but requires internal shear. Similar crustal flow may be present wherever sufficiently thick and hot oceanic crust is extended. One such common scenario is volcanic rifted margins during breakup, which display oceanic crustal thickness of up to 30 km and elevated temperatures due to upwelling asthenosphere (Geoffroy, 2005). Moreover, any place where a mantle plume interacts or has interacted in the past with a spreading ridge, will have undergone such conditions. Furthermore, since we know the Earth is cooling over time, oceanic crustal flow may have been more widespread in the distant geological history. Another practical implication of LPO in the crust is that it may complicate the delay times measured in SKS splitting studies that are usually attributed to the mantle.

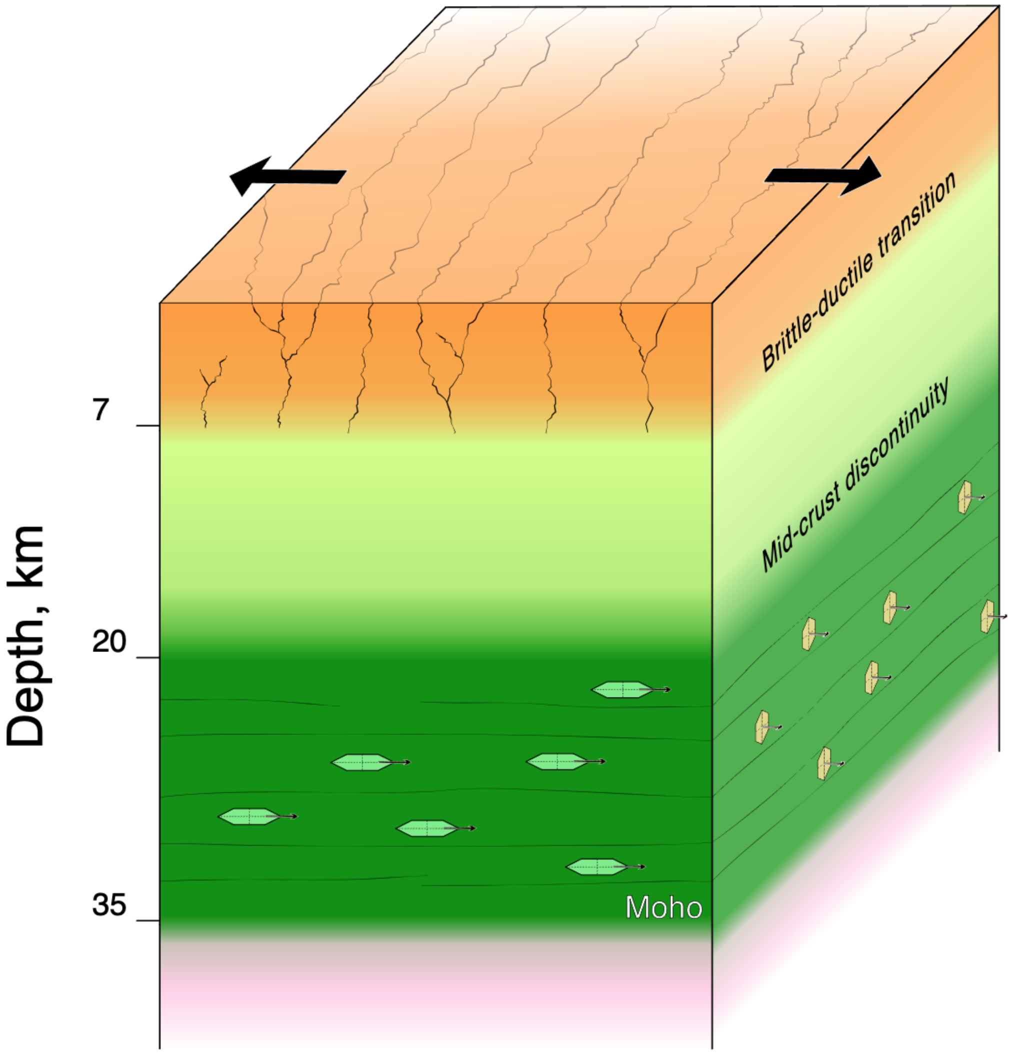

Fig. 3.9 Schematic summary of interpreted mechanisms for seismic anisotropy in the Icelandic crust. Black arrows indicate the spreading direction. In the upper crust spreading perpendicular cracks dominate seismic anisotropy. In the lower crust, LPO is the main contributer to seismic anisotropy

3.3 Methods

3.3.1 Seismic Data

Continuous broadband records from the following sources were used in this study: 1) An ongoing deployment by the University of Cambridge that is largely focused in the rift zones, supplemented with seismometers from the British Geological Survey. 2) HOTSPOT - a temporary deployment which operated from 1996 - 1998. 3) The IMAGE project network deployed on the Reykjanes Peninsula by GFZ. 4) The permanent station BORG of the Global Seismic Network. We only used data from instruments which have a corner frequency of 0.0166 Hz (60 s period) or lower (mostly Guralp 3ESP and Streckeisen STS2) which are installed in vaults. This dataset includes a total of 418 potential station pairs for data analyses.

3.3.2 Extraction of Dispersion Curves

The extraction of daily Noise Cross-correlation Functions (NCFs) from continuous records is performed following Bensen et al. (2007). 3-component daily continuous records are first detrended, demeaned and tapered before being bandpass filtered between 2 – 60 seconds and decimated to 1 Hz. The response of the instrument is then deconvolved from the waveforms which are next convolved with the response of the instrument with the narrowest period band (Guralp 3ESP with a period of 60 s). Next, the North and East components are rotated to radial and transverse. This is followed by winsorizing at 3 RMS, which reduces the effect of large amplitude spurious arrivals, and spectral whitening. Finally, the waveforms at different stations are cross-correlated and stacked using phase weighted stacking (Ventosa et al., 2017) to give an NCF. Love and Rayleigh phase velocity dispersion curves are extracted from NCFs by using the method of Yao et al. (2006). The causal and acausal parts of the NCF are averaged and the symmetric NCFs are converted to Empirical Green's Functions (EGF). The EGFs are then subjected to a series of narrow bandpass filters centered at 1 second intervals up to a period corresponding to 1/12 of the station separation distance. It should be noted that while the measurements appear as discrete points in Fig 3.9, adjacent points are not truly independent measurements since the filter has a decay period band which can lead to a certain overlap in frequency content. This representation is however true to the way information is inserted into the inversion software SURF96 which requires discrete measurements and has no notion of measurement width. Next, a dispersion curve is then extracted by picking the arrival on the filtered EGF with the longest period and tracking it down to shorter periods, stopping if a sharp change in velocity is encountered.

We only used station pairs with a station spacing of more than 200 km, which left 221 station pairs out of a maximum of 418. This ensures a high quality of measurements (Russell et al., 2019) and guarantees a relatively long sampling period (>=20 s) which is important for depth sensitivity. In the next step we discarded any dispersion curve that was too short (included less than 15 consecutive discreet periods) or visually corrupted. The 15 consecutive discreet periods criterion is somewhat arbitrary but reducing it to 8 did not add usable data points in the azimuth range of 140°–170°, which is lacking in our dataset. The gap is attributed to the fact that Iceland is more limited in its N-S extent (200 – 250 km) compared to its E-W extent (350 – 450 km) and that there is a lack of broadband instruments along the northern coast. The final dataset contains 75 station pairs with a good azimuthal coverage except for a gap between 140°–170°.

3.3.3 Inverting for path average shear velocity

We perform a regularized non-linear inversion of phase dispersion curves for 1-D shear velocity with a range of different starting models using SURF96 (Herrmann, 2013). We use 8 constant gradient starting models with 0.25 km/s spacing which are shown in grey lines in Fig. 3.5a. First, the Rayleigh dispersion curve is inverted for V_{SV} structure. Then, the resulting V_{SV} profile is used as an initial model for inverting the Love dispersion curve for V_{SH}. Finally, radial anisotropy is calculated as $\xi = (V_{SH}/V_{SV})^2$. The difference in the inversion result introduced by the different starting models (Fig. 3.5b) is largest near the surface and in the mantle and smallest around 20 km depth (each profile represents the result from a single starting model). This is attributed to the period range used in this work ($\sim$10 – 40 s). The choice of the user defined damping parameter on the result is shown in Figure 3.10 and does not change the main observation.

3.3.4 Uncertainty of ξ vs azimuth

To estimate the uncertainty in the ξ vs azimuth plot (Fig. 3.7) we use two different approaches. First, we use the standard deviation of the ensemble of different inversion results generated by using different starting models as a measure of uncertainty. The result is shown in Figure 3.11a-c. It can be seen that the uncertainty arising from different starting models is small compared to the size of the azimuthal variations. A different approach for estimating uncertainty is binning the data and using the mean and standard deviation within each bin. This approach is arguably more meaningful since each measurement is independent. We test two different bin sizes, 30° and 15°, and the results are shown in Figures 3.11d-f and

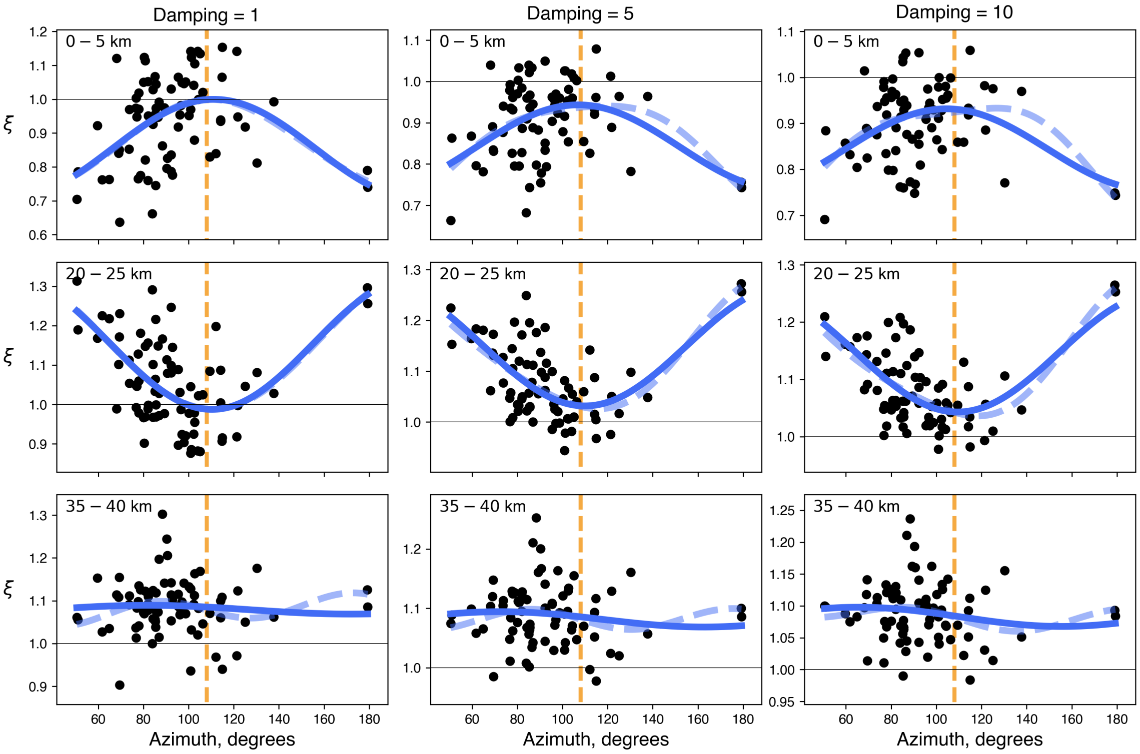

Fig. 3.10 The user defined damping parameter in the shear velocity inversion may affect the result. We present the same azimuthal variation of radial anisotropy results as Figure 3.7 with different damping factors. As expected, increasing the damping factor decreases the amplitude of the signal but does not affect the observed trend of positive anisotropy in the lower crust (20 - 25 km), and negative anisotropy in the upper crust (0 - 5 km).

3.11g-i respectively. Both plots show that the uncertainty is small compared to the size of the azimuthal variations.

3.3.5 Effect of V_P on ξ values

A major assumption in the inversion process we adopt is that Rayleigh waves are only sensitive to V_{SV} and Love waves to V_{SH}. This assumption is not strictly true since Love waves are also slightly sensitive to V_{SV} and Rayleigh waves to V_{PH} and V_{PV} (Anderson, 1965; Dziewonski and Anderson, 1981). Since we only use fundamental modes, the Love wave sensitivity to V_{SV} is not a major issue as they are nearly independent of V_{SV} (Dziewonski and Anderson, 1981) and isotropic calculations should give approximately correct results (Bhattacharya, 2015). The sensitivity of Rayleigh waves to V_{PH} and V_{PV}, although much smaller than to V_{SV}, is more substantial and could affect an isotropic inversion.

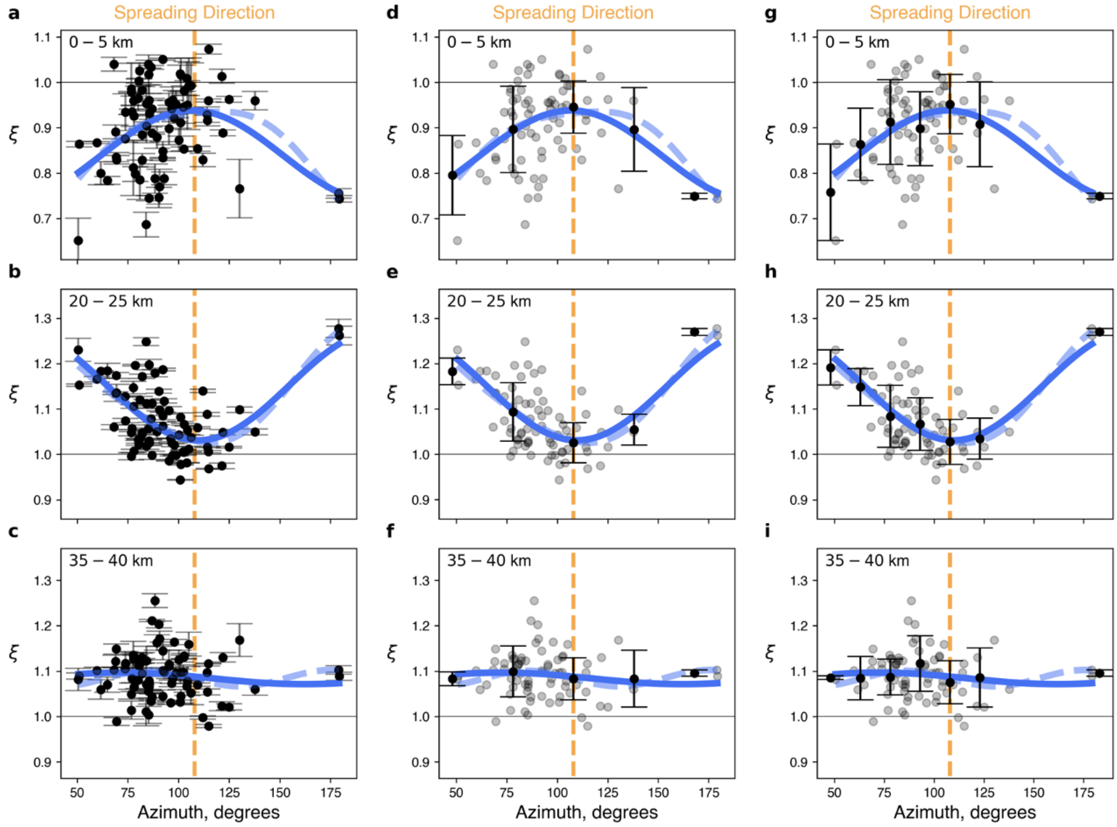

Fig. 3.11 Data points and sinusoid fits are the same as in Figure 3.7. **a-c** Error bars indicate individual uncertainty values assigned to each data point based on the standard deviation of the ensemble of different inversion results from using different starting models. **d-f** Data points from Figure 3.7 are shown in grey. Black dots are data binned to 30° bins and error bars indicate standard deviation within each bin. Bins with only one data point are not plotted. **g-i** same as **d-f** but with 15° bins.

To test the effect of V_P on our results, we examine a wide range of plausible V_P/V_S ratios (Darbyshire et al., 1998), which are kept constant during the inversion for V_S. We tested 20 V_P/V_S models including: constant ratio, gradual increase and sharp increases at 20 and/or 40 km depths which are shown in Figure 3.12a. The different V_P/V_S models made only negligible changes to the resulting anisotropy profile shown in Figure 3.12b, indicating very little sensitivity to isotropic V_P. This poor sensitivity may be explained by Rayleigh wave sensitivities to V_{PH} and V_{PV} having mostly opposite signs, suggesting that decreasing one and increasing the other can change Rayleigh wave velocities without changing the isotropic V_P.

While unmodelled P-wave anisotropy may still affect the accuracy of our ξ values to a degree, it is unlikely to change the conclusion due to the comparative nature of our observation

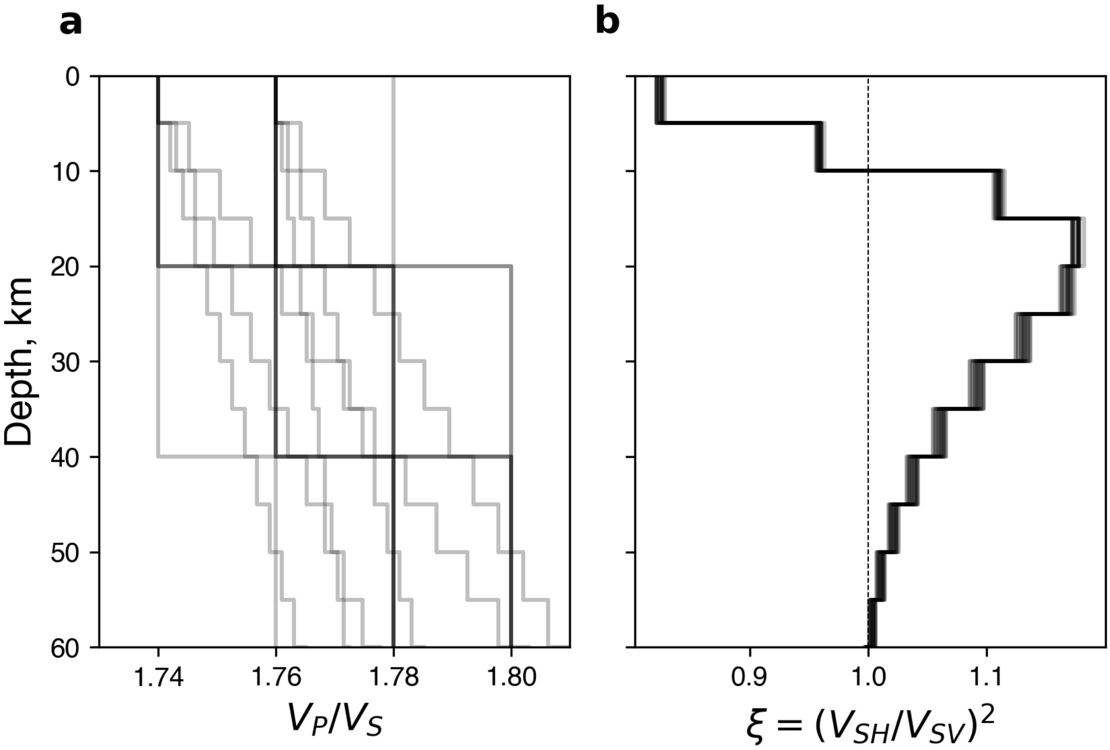

Fig. 3.12 **a** The range of 20 V_P/V_S models used when inverting for shear velocity and anisotropy are plotted as grey lines. The data and inversion process are the same as in Figure 3.5. **b** The resulting radial anisotropy models from using the different V_P/V_S models are plotted as grey lines.

for several reasons. First, as previously mentioned, the Rayleigh wave sensitivities to V_{PH} and V_{PV} are still small compared to V_{SV} and the size of the observed S-wave anisotropy is very large ($>$ 10% in some azimuths). While it could be overestimated due to unmodelled P-wave anisotropy, it would probably require an unreasonable amount of only P-wave anisotropy to generate if no S-wave anisotropy is present. Second, it is unlikely that such substantial P-wave anisotropy will not be accompanied by some S-wave anisotropy. Putting all of the above together, explaining our observed azimuthal changes without S-wave anisotropy would require an extreme azimuthal increase in P-wave anisotropy without an accompanying increase in S-wave anisotropy. Not only would it be difficult to find a physical explanation for this, if one existed it would probably be best explained using LPO in any case.

Therefore, we conclude that the qualitative nature of our observation – increasing S-wave anisotropy away from the spreading direction – is not influenced by this approximation even if the exact anisotropy values are overestimated.

3.3.6 "Squeezing" tests

Due to the smooth nature of surface waves sensitivity kernels, inverting phase velocities may "smear" vertical structure and make it hard to tell which parts of the model require radial anisotropy to explain our observation. To test this, we try to fit our data while "squeezing" the anisotropy into specific parts of the models by keeping other parts isotropic. For convenience, we name parts of our model as follow: brittle crust (0 – 5 km), ductile crust (5 – 30 km), mantle (30+ km). Additionally, we divide the ductile crust into gabbroic (5 – 20 km) and olivine enriched (20 – 30 km) parts.

To support our main conclusion, it is important to show that positive radial anisotropy must be present in the ductile crust. We repeat the inversion process while requiring that the ductile crust remain isotropic, with the result displayed in Figure 3.13. Not only do we see that the level of fit for Love dispersion is reduced, we also find that the resulting models require unrealistically high anisotropy in the mantle. Therefore, we conclude that the radial anisotropy is required within the ductile crust.

We next test whether we can narrow the source of positive anisotropy to the gabbroic part of the ductile crust or to the olivine enriched part, the results of which are displayed in Figures 3.14 and 3.15. As is often the case, it can be seen that there is a trade-off between the thickness of the anisotropic layer and the strength of anisotropy, and both models are able to fit our data. When the olivine enriched part is kept isotropic, the gabbroic layer and the mantle both show a significant increase in anisotropy values. This model would indicate a significant contribution to anisotropy from LPO in gabbro. However, while possible, it is somewhat difficult to suggest a mechanism that would produce such strong LPO only in the gabbroic layer and the mantle but not in between them. When the gabbroic part is kept isotropic, we need an increase in anisotropy in the olivine enriched part and to some extent in the mantle. This model could be interpreted by assigning the increase in anisotropy with depth within the crust to either the olivine enrichment or to the increase in temperature with depth.

Additionally, we test whether negative anisotropy is required in the brittle crust by setting it to be isotropic, the results of which are presented in Figure 3.16. We observe that a sizeable negative anisotropy anomaly is generated immediately below the brittle layer, creating a model which would be extremely hard to explain. While not shown, we also tried keeping larger parts of the model near the surface isotropic (0 – 10 km and 0 – 15 km). This had a similar effect of pushing the negative anisotropy deeper and reducing the quality of fit for short period Love wave dispersion data.

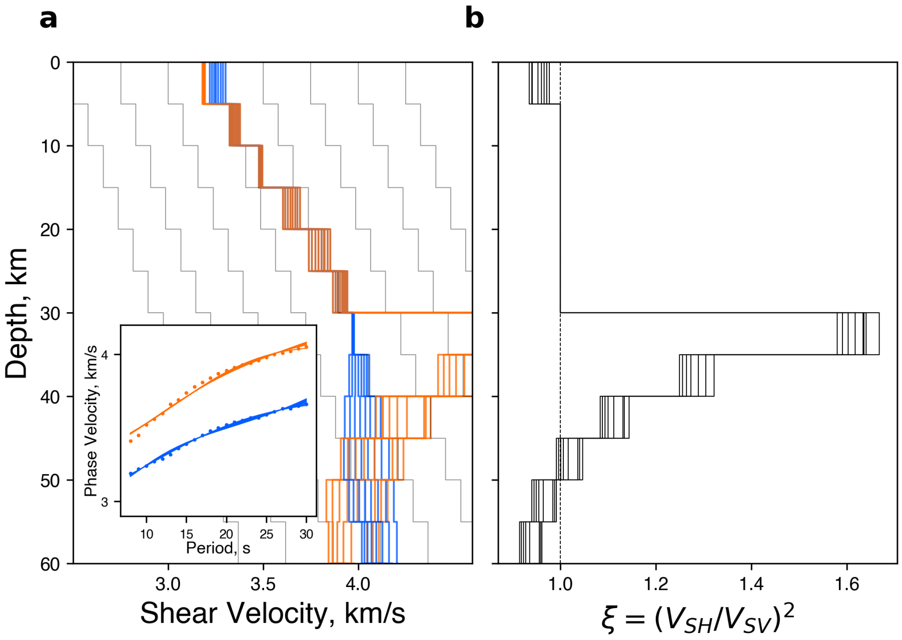

Fig. 3.13 Same as Figure 3.5 but the ductile crust (5 – 30 km) is kept isotropic.

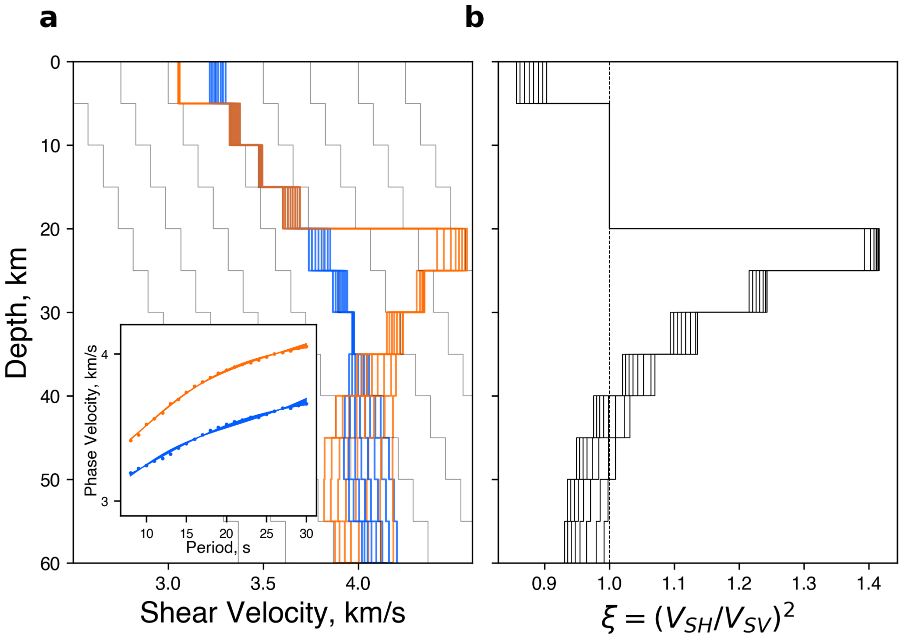

Fig. 3.14 Same as Figure 3.5 but the gabbroic part of the ductile crust (5 – 20 km) is kept isotropic

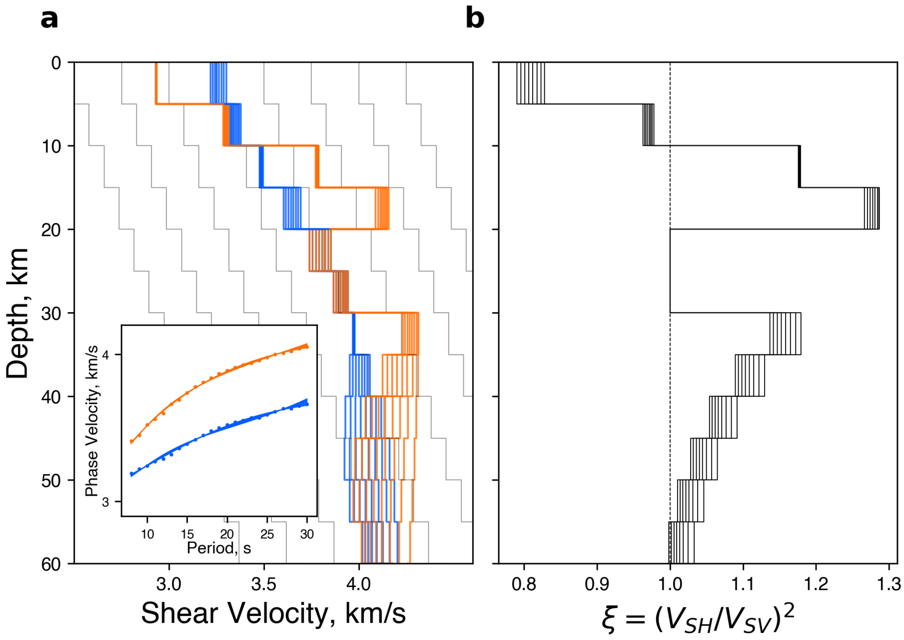

Fig. 3.15 Same as Figure 3.5 but the olivine enriched part of the ductile crust (20 – 30 km) is kept isotropic.

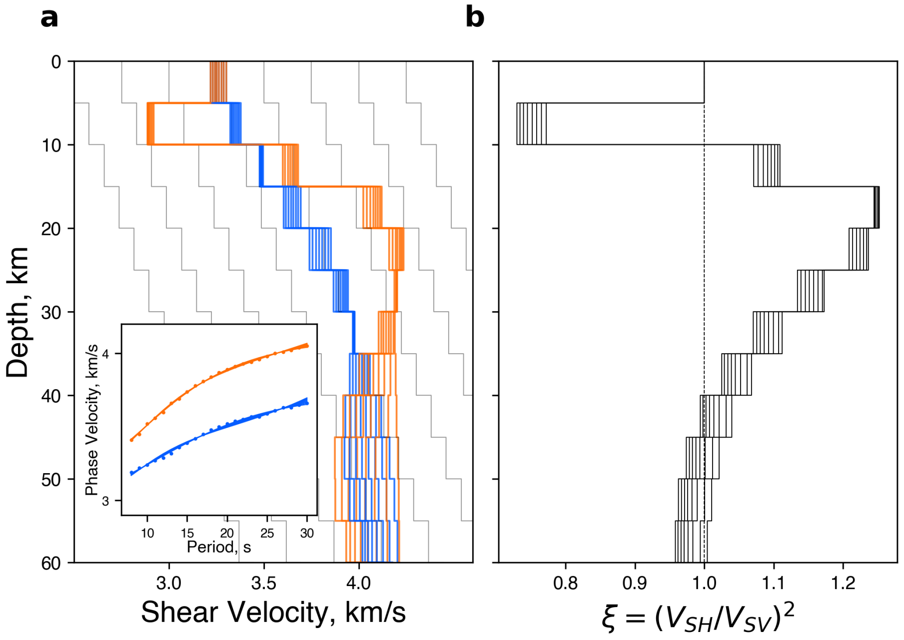

Fig. 3.16 Same as Figure 3.5 but the brittle crust (0 – 5 km) is kept isotropic.

3.3.7 Model fitting for ξ versus azimuth data

We fitted the data with two periodic functions. One with only a 2θ term and one with both a 2θ and a 4θ term:

$$\xi(\theta) = A * \cos(2 * (\theta - \varphi_A)) + C \tag{3.1}$$

$$\xi(\theta) = A * \cos(2 * (\theta - \varphi_A)) + B * \cos(4 * (\theta - \varphi_B)) + C \tag{3.2}$$

where θ is azimuth and the rest are free parameters. A and B are the amplitudes of 2θ and a 4θ sinusoids respectively. φ_A is the azimuth of the largest amplitude for the 2θ sinusoid and φ_B (and $\varphi_B \pm 90$) is the azimuth of the largest amplitude for the 4θ sinusoid. The free parameters have no clear physical meaning and are simply used to check if the anisotropy has a periodical behaviour. Model fitting for intermediate depths not displayed in Figure 3.7 can be seen in Figure 3.17. Fitting was done using the curve_fit procedure in the open source Scipy package in Python without any initial guess or constrains.

3.3.8 Control of the two data points at 175° on the result

The two data points at 175° may appear to exert a strong control on the model fitting in Figure 3.7. To test this, we fit the same models as shown in Figure 3.7 but without using these two points and the results are shown in Figure 3.18. The observed fit is similar and again shows low radial anisotropy near the spreading direction and high values away from it at 20 – 25 km depth. The t-test for statistical difference between "spreading-parallel" and "spreading-perpendicular" ray paths was also repeated without these two points and the result remained highly significant ($p < 0.01$)

3.3.9 Additional North South station pairs

As mentioned, due to Iceland's narrow N-S extent and a shortage of broad band coverage along it's northern coast, we found almost no station pairs with an azimuth above $\sim$130° that passed our quality control criteria. As also discussed earlier, we believe that this dataset is good enough to support our conclusions since it is sufficient to show that radial anisotropy increases away from the spreading direction with decreasing azimuth on a 90-degree range to conclude that azimuthal variations exist. The alternate hypothesis of TPL would show up as a random distribution of anisotropy values without correlation. Nonetheless, to further explore our results, we have searched for additional station pairs with azimuths larger than 130° which only marginally failed our quality control criteria, detailed in sections 3.3.1 and 3.3.2. We have found 10 such stations pairs which are shown in Fig.3.19. We then calculated

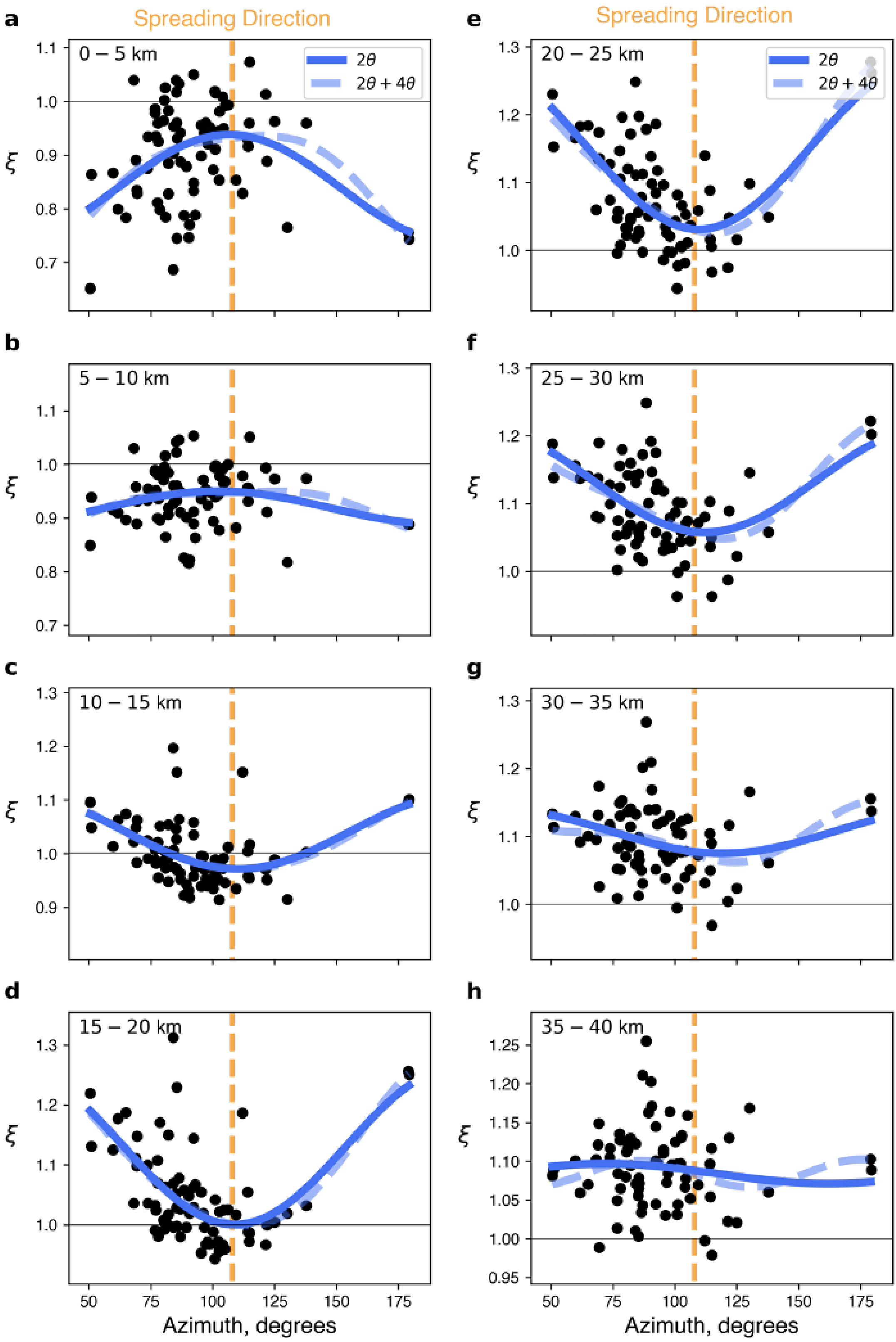

Fig. 3.17 Same as Figure 3.7 for depths 0 - 40 km.

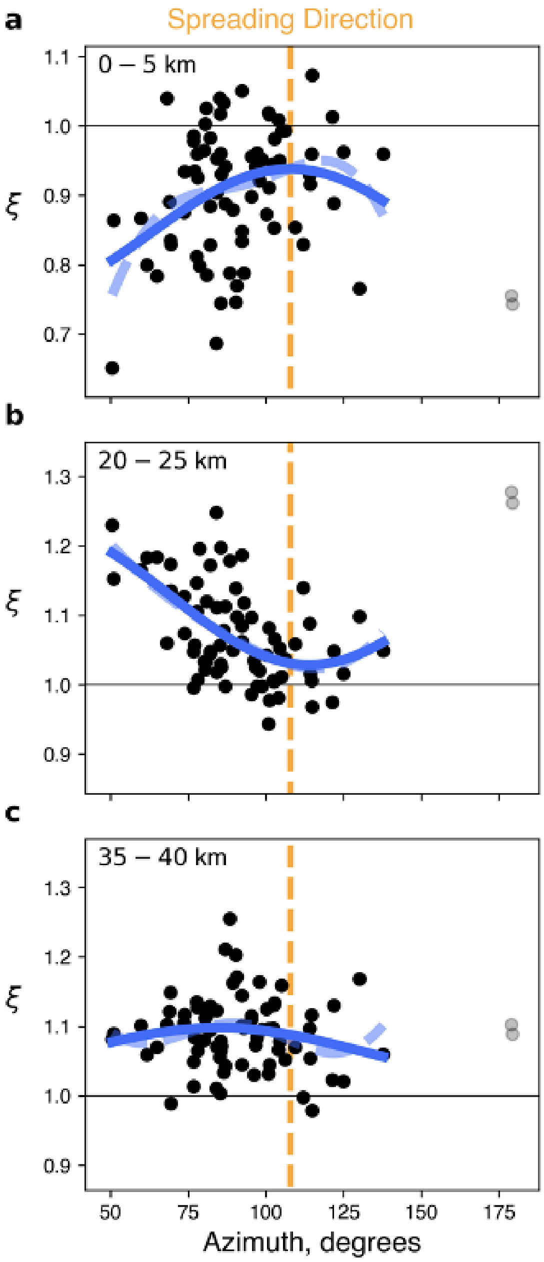

Fig. 3.18 Same as Figure 3.7 but model fitting is done without the two data points at ∼175° indicated in grey.

the radial anisotropy along those paths which are shown as empty circles next to the results of the main analysis in Fig.3.20. At the depth of 20 - 25 km (Fig.3.20b), it can be seen that except for a single point at (160°,1.02) all new data point fall relatively close to the fitted sinusoid. While interpreting these data points requires caution due to the different quality control criteria, we conclude that they do not alter our observation in the lower crust. in the upper crust (Fig.3.20a) and mantle which (Fig.3.20c) which are not the focus of our work, the scatter is large and cannot be said to reinforce or contradict our findings.

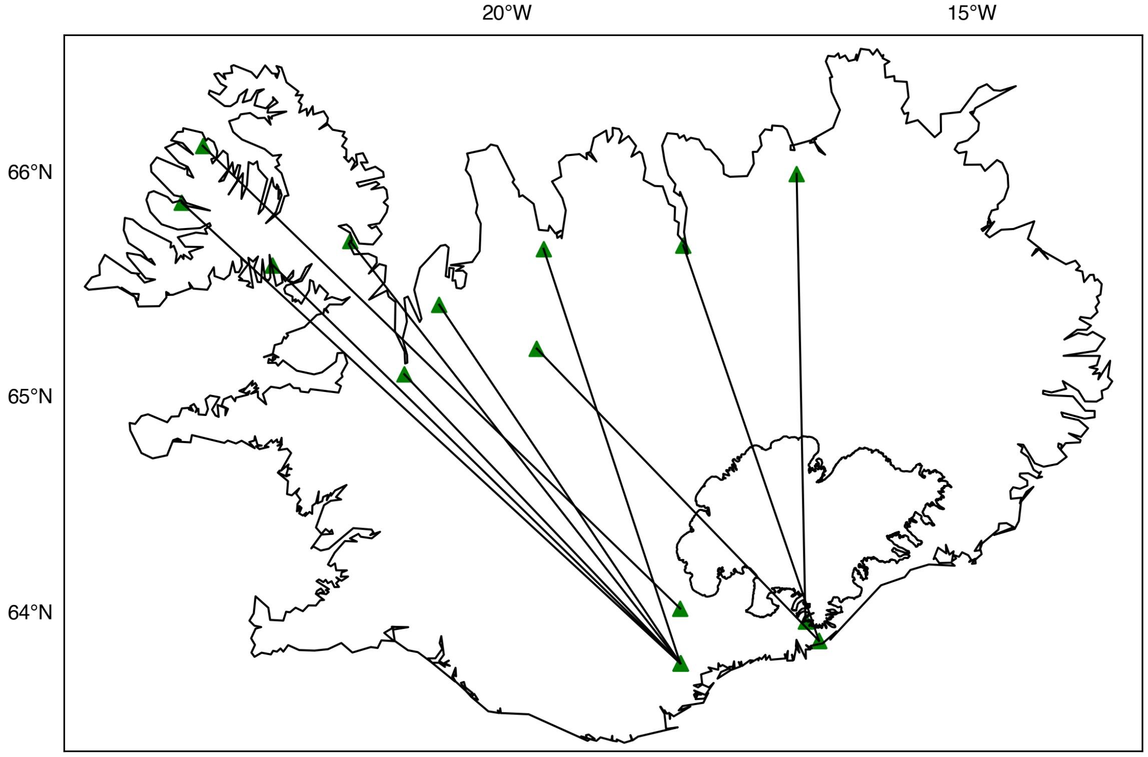

Fig. 3.19 10 Additional inter station paths which marginally failed our quality control criteria and were not used in the main analysis

3.3.10 F tests

To observe trends in the ξ versus azimuth plot (Fig. 3.7) we fit several different functions to the data. If two functions with a different number of free parameters are fitted to the same dataset, the function with the larger number of free parameters will normally have lower residuals due to the extra free parameters, regardless of the quality of fit. An F-test can determine whether the reduction in residuals justifies the extra free parameters. An F test is

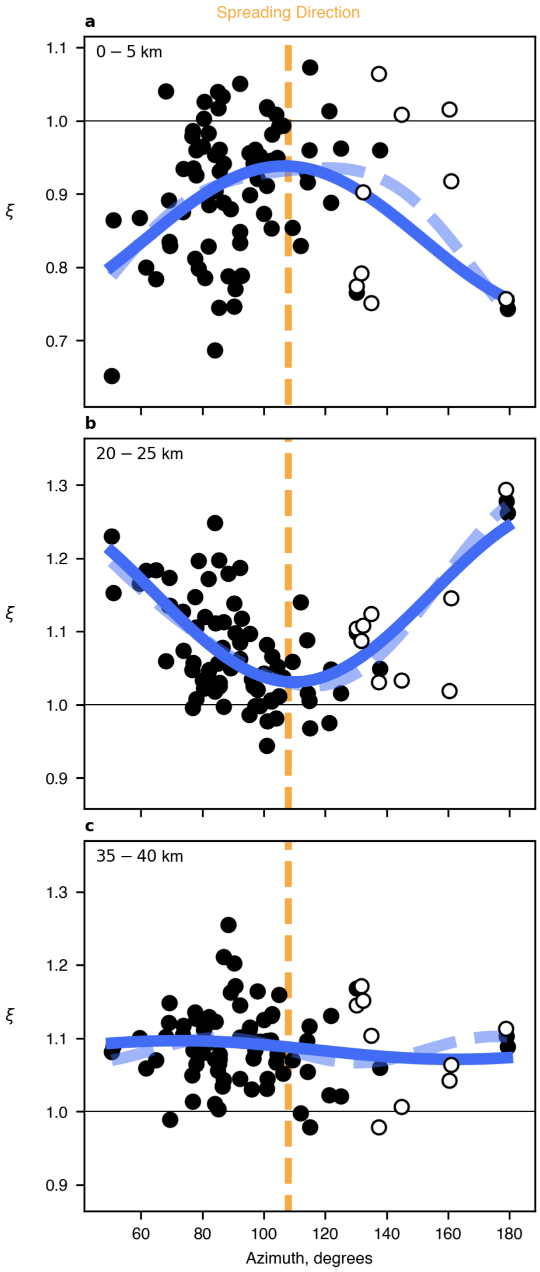

Fig. 3.20 Same as Fig. 3.7 with the addition of 10 additional data points (denoted by empty circles) representing station pairs which marginally failed our quality control criteria.

computed by solving:

$$F = \frac{\left(\frac{RSS_1 - RSS_2}{p_2 - p_1}\right)}{\left(\frac{RSS_2}{n - p_2}\right)} \tag{3.3}$$

where RSS_1 and RSS_2 are the residual sum of squares for models 1 and 2 respectively, p_1 and p_2 are the number of free parameters in each model and n is the number of data points. The resultant F can be used to obtain a p value that indicates whether the extra free parameters are justified. Tests were performed using the open source Scipy package in Python.

3.3.11 T test

The t-test can be used to determine whether the means of two sets of data are significantly different from each other. Tests were performed using the open source Scipy package in Python.

Chapter 4

Velocity and anisotropy structure of Askja volcano from ambient noise: Implications for body and surface wave models.

The work presented in this chapter has been submitted as a manuscript to Geophysical Journal International with the following co-authors and title:

Volk, O., White, R. S., Greenfield, T., Winder, T., Bacon, C. Rawlinson, N. (2020) Velocity and anisotropy structure of Askja volcano from ambient noise: Implications for body and surface wave models. *In revision - Geophysical Journal International*

I acknowledge the work of T.G. and T.W. who performed the earthquake relocation analysis and C.B. who contributed the local shear wave splitting dataset.

4.1 Chapter abstract

In recent years, measuring surface wave velocity from ambient noise has gained increasing popularity in the study of crustal properties. However, extensive comparisons between ambient noise results and those obtained from local earthquakes remain elusive. Here, we measure Love and Rayleigh group velocity using ambient noise recorded around Askja, a large active volcano in central Iceland, explore its velocity structure and anisotropy and compare our findings to those from local earthquake studies. We find that crack density and

orientation estimated using surface wave anisotropy strongly correlate with local shear wave splitting and outcrop mapping, indicating the method is highly effective for such analyses. Furthermore, we show that V_{SV} derived from Rayleigh waves can be significantly faster than V_S extracted from body waves, which has important implications for jointly exploiting these two classes of data. Finally, we invert the travel times for 3D V_{SV} and V_{SH} models and image a shallow slow anomaly consistent with a magma body predicted by geodetic data at a depth of 2 - 3 km but not resolved by body wave tomography, demonstrating how the two datasets can complement each other.

4.2 Introduction

The properties of the shallow crust are important in a wide range of applications including hydrology, hydrocarbon exploration and geohazard assessment. In the case of volcanoes, the shallow crust is crucial for understanding how volcanic systems work, since this is where the majority of degassing occurs and magmatic and hydrothermal systems interact. In recent years, the relatively new method of measuring surface wave velocities using ambient noise (Shapiro and Campillo, 2004; Shapiro et al., 2005; Yao et al., 2006) has become a valuable tool for studying crustal velocity structure and anisotropy. The main advantage of the method is that it is completely independent of earthquakes and therefore very useful in aseismic regions or where event location limits the coverage of body waves. Moreover, it also very useful for exploring azimuthal and radial anisotropy, which makes it an important tool for various applications such as measuring crack properties.

Although the ambient noise method was originally developed and implemented for relatively large regions, it has subsequently gained popularity in volcano-seismology (e.g. De Siena et al., 2018; Brenguier et al., 2007; Masterlark et al., 2010; Obermann et al., 2016) and other local-scale studies that involve shorter periods and shallower heterogeneities. Furthermore, it is gradually becoming common to use earthquake body waves and surface waves from ambient noise jointly when the two datasets overlap. Possible uses include ray tracing through crustal models derived from ambient noise to determine earthquake location (e.g. Johnson et al., 2010; Jolly et al., 2017), accounting for crustal contribution to teleseismic travel times (e.g. Rawlinson et al., 2016) and joint inversion of body waves and surface waves (e.g. Syracuse et al., 2015). Such uses often implicitly assume that the different data sets have similar or complementary sensitivities. For instance, locating local earthquakes using surface wave derived velocity models implicitly assumes that body waves and surface waves are sensitive to the same structure.

In practice however, body and surface waves may have different sensitivity to structure and different sources of errors. For example, the typical periods used for the picking of body waves from local earthquakes tend to be well below 1 s, while for surface waves periods above 0.5 s are usually used. This difference means that body waves are sensitive to smaller scale structure. Another difference is that while Love and Rayleigh are, to first-order, only sensitive to V_{SV} and V_{SH} structure respectively, body waves sample a combination of both along their ray path. Therefore, it is important to properly understand the implications of these differences if body and surface waves are to be jointly used to constrain seismic structure.

Another geophysical method which can be used jointly with ambient noise tomography and is popular in studying volcanoes is InSAR (Interferometric synthetic-aperture radar) (Pepe et al., 2019; Masterlark et al., 2010; Xie et al., 2011). While InSAR provides highly-resolved spatial and temporal images of ground deformation, ambient noise tomography images the subsurface structure and the two methods can complement each other in giving more holistic interpretation. For example, Pepe et al. (2019) developed an InSAR analysis tool named Total Horizontal Derivative which highlights the deformation source boundaries and showed that the patterns retrieved by applying it at Campi Flegrei volcano revealed the same bi-lobe structure which appears as a slow anomaly in the ambient noise tomography. Similar comparisons between ambient noise tomography ans InSAR can therefore lead to a better understanding of volcanic systems, as well as demonstrate the advantages and limitations of such works.

Askja, a large volcano in the central Icelandic highlands (Fig. 4.1), has been intensively studied using various methods including body wave tomography (Mitchell et al., 2013; Greenfield et al., 2016), local shear wave splitting (Bacon et al., 2019), InSAR (De Zeeuw-van Dalfsen et al., 2012; Rymer and Tryggvason, 1993; Sturkell and Sigmundsson, 2000; Sturkell et al., 2006; Pagli et al., 2006) and detailed field mapping (Hjartardóttir et al., 2009), but not using ambient noise. The region around Askja has a dense long-term coverage of seismic instruments and is therefore an ideal location for comparing ambient noise results to existing observations in a shallow heterogeneous environment. In what follows, we first measure the group velocities of Rayleigh and Love waves around Askja from the recorded ambient noise wavefield. We then invert for 1D V_{SV} and V_{SH} regional models, calculate radial anisotropy, and compare the results to a regional 1D model derived from body waves. Next, we use measurements of azimuthal anisotropy to infer the primary crack orientation and compare the result to field mapping and local shear wave splitting. Finally, we invert the velocities to obtain 3D V_{SV} and V_{SH} models and compare them to body-wave tomography results. We conclude by discussing the merits of using short period surface waves extracted from ambient noise in studies of the shallow crust, including their applicability in joint body and surface wave studies and earthquake location.

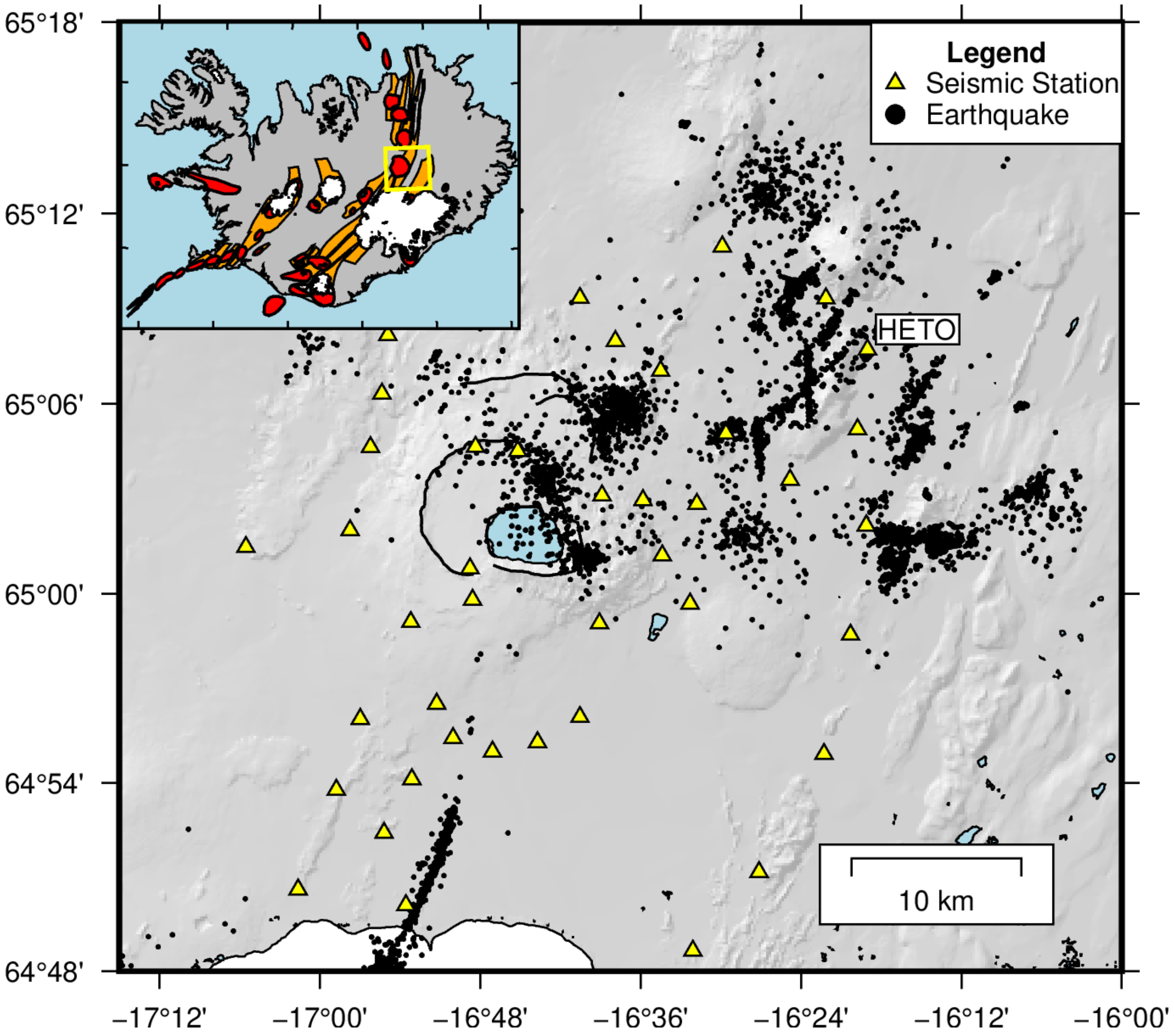

Fig. 4.1 A map of the research area. Black lines show the outlines of Askja calderas and black dots indicate background seismicity. Yellow triangles denote seismic stations used in this work and blue areas represent water bodies. The inset map shows the study area location in Iceland. Red areas indicate recent volcanism, orange areas show fissure swarms associated with rifting and white areas indicate the location of icecaps.

4.3 Methods and Data

4.3.1 Seismic Data

In this study, we use continuous recordings with an average duration of 24 months and a minimum of 10 months from 44 3-component broadband seismic stations (Fig. 4.1), which are a part of an ongoing deployment run by the University of Cambridge that focuses on Askja and Bárðarbunga volcanoes in the central highlands in Iceland (Greenfield et al., 2020).

4.3.2 Group velocity measurements

We follow the workflow of Bensen et al. (2007). 3-component daily continuous records are first detrended, demeaned and tapered before being bandpass filtered between 2 – 30 seconds and decimated to 1 Hz. Next, the instrument's response is deconvolve from the record and the resulting waveform is convolved with the response of the instrument with the narrowest period band used in the analysis (Guralp 6TD with a period of 30 s). Next, the horizontals are rotated to radial and transverse components. This is followed by winsorizing at 3 times RMS (replacing extreme values with truncated ones), which reduces the effect of spurious large amplitude arrivals, and spectral whitening. Next, the waveforms from all simultaneously recording pairs of stations are cross correlated and stacked using phase weighted stacking (Ventosa et al., 2017) (Fig. 4.2). Finally, we estimate the group velocity dispersion curves (Fig. 4.3) using an automated code (Pilia et al., 2015) for frequency time analysis (Dziewonski et al., 1969; Levshin and Ritzwoller, 2001). Cross correlations from inter-station distances smaller than 1.5 wavelengths or that have signal to noise ratios (SNR) smaller than 10 are discarded. We retrieve 303 dispersion curves for Rayleigh waves and 440 for Love waves.

4.3.3 Forward modelling of dispersion curves and 1D shear inversions

SURF96 (Herrmann, 2013) is used for both the forward modelling of dispersion curves and the 1D non-linear regularized inversions of dispersion curves for velocity structure. The top of the surface wave model is set at the average station elevation of 800 m above sea level and the model is parametrized using 1 km thick layers. This parametrize was chosen following the model of Mitchell et al. (2013) since one of the main objectives of this study is to compare that model to the surface wave derived velocity models we produce. The inversion process is repeated 100 times using different starting models (Fig. B.2) which are generated by randomly perturbing the body wave model from Mitchell et al. (2013) and the standard deviation of the results is used to estimate model uncertainty.

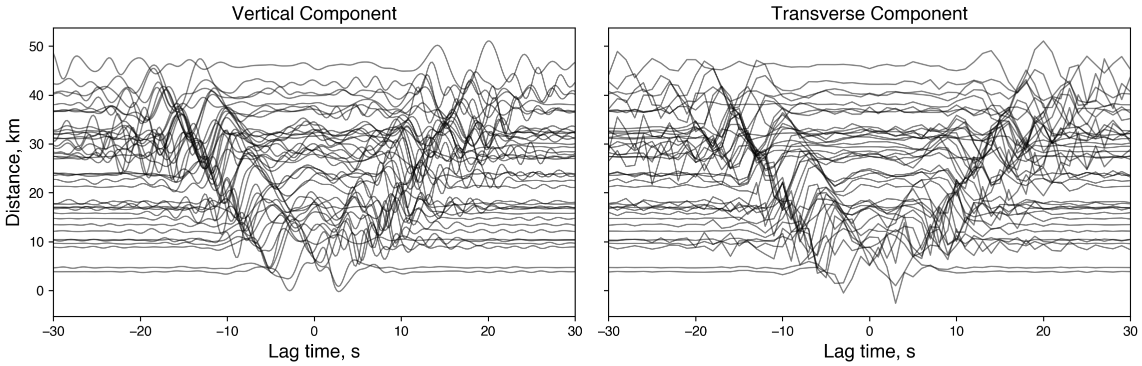

Fig. 4.2 Noise cross correlation functions extracted from the vertical and transverse components for all station pairs that include HETO (Fig. 4.1). Both plots display a typical move-out pattern associated with surface wave empirical Green's functions.

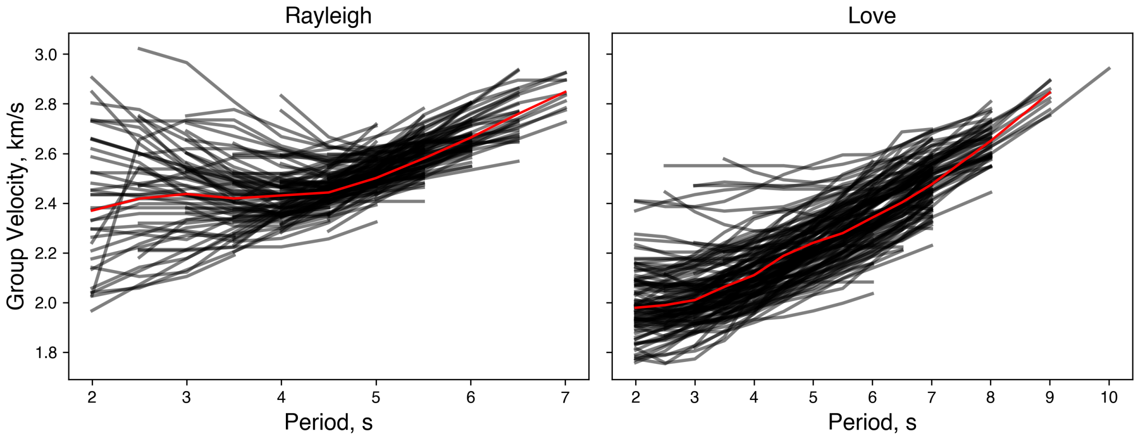

Fig. 4.3 Rayleigh and Love wave group velocity dispersion curves extracted from the cross-correlations are shown in black. The red line indicates the mean group dispersion curve.

4.3.4 Earthquake location

A random selection of 200 local earthquakes are chosen from a catalogue with manually-refined phase arrival times (Greenfield et al., 2020). We perform no quality control of this catalogue to test the location stability for both well-located (30+ P- and S-wave phase arrival picks with good azimuthal coverage and at least one station close to the epicentre) and poorly located (<10 P- and S-wave phase arrival picks with maximum azimuthal gap of up to 180deg) events. Earthquake hypocentres are inverted for using the program NonLinLoc (Lomax et al., 2014), with travel-time look-up tables created using the finite-difference scheme from Podvin and Lecomte (1991). An equal-differential-time approach (Font et al., 2004), is used to generate a complex probability density function (pdf) for each earthquake.

This pdf is then sampled using an oct-tree sampler. The maximum likelihood location is chosen as the final hypocentres for each event.

4.3.5 Isotropic 2D group velocity maps

The inversion of inter-station surface wave travel times for 2D period-dependent group velocity maps was done using FMST (Rawlinson and Sambridge, 2005), an iterative non-linear travel time tomography code. The model spans 56 km in longitude (E-W), 66 km in latitude (N-S) and is parametrized using a velocity grid with 2 km spacing. We invert the travel times of 3 - 6 s Rayleigh and Love waves separately. The inversions involve 136 travel times for Rayleigh and 312 for Love. Damping and smoothing regularisation are imposed to address the issue of solution non-uniqueness, and return models that favour smaller perturbations to the starting model and longer wavelength structure. The selection of damping and smoothing parameters is performed using an L-curve (Fig. 4.4), with values closest to the "knee" of the L chosen as the optimum trade-off between data fit, model smoothness and model perturbation. To achieve this we repeat the inversion several times while varying one of the two parameters and keeping the other fixed at 0.1.

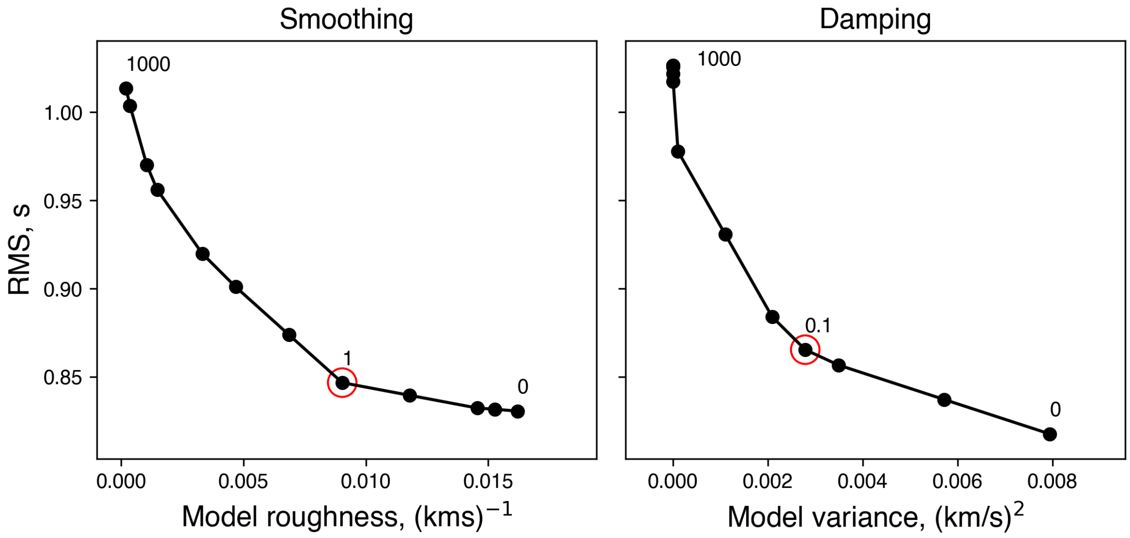

Fig. 4.4 An example of how damping and smoothing parameters were chosen for the inversion at a period of 4 s. The red circle shows the selected value which best balances model smoothness/perturbation and data fit.

4.4 Results and Discussion

4.4.1 1D Shear velocity models and radial Anisotropy

Although 1D velocity models have limited applicability in strongly heterogeneous regions such as central Iceland, they represent a useful first-order approximation for many studies. We start our analysis by comparing the average dispersion curves for Love and Rayleigh waves with the dispersion curves predicted by an existing 1D shear velocity model constrained by body waves (Mitchell et al., 2013) (Fig. 4.5a). For Love waves, the observed dispersion curve is slightly faster than the predicted dispersion curve, but overall is largely similar considering the heterogeneity of the region and the uncertainties contained in the surface wave data and body wave model. For Rayleigh waves, the observed dispersion curve is similar at longer periods but becomes considerably faster than the predicted dispersion curve as the period decreases.

We then invert the average Love and Rayleigh wave dispersion curves for representative 1D V_{SH} and V_{SV} models respectively. As expected from the dispersion curves shown in Fig. 4.5a, the V_{SH} model is largely similar to the body wave model whereas the V_{SV} model becomes significantly faster at shallow depths. We attribute the similarity between the body wave model and the V_{SH} model from Love waves to the fact that body waves emanating from earthquakes below the array tend to impinge upon the surface with near vertical slowness and are therefore mostly polarized in the horizontal plane, similarly to Love waves. We interpret the increase in V_{SV}/V_{SH} closer to the surface in terms of an increase in the sub-vertical crack density as depth decreases. Such sub-vertical cracks are expected at rift zones and will decrease V_{SH} much more significantly than V_{SV} (Ding et al., 2017). To estimate the crack density, we calculate the radial anisotropy (Fig. 4.5c) in percent as $100 \times \frac{V_{SH}-V_{SV}}{(V_{SH}+V_{SV})/2}$. Although the relationship between crack density and radial anisotropy is complex and involves exact knowledge of crack geometry and void infill, we use a simplified relationship (Ding et al., 2017) to obtain a first-order estimate. We note that this calculation relies on the assumption that Rayleigh and Love waves are only sensitive to V_{SV} and V_{SH} respectively which is not strictly correct (for an extended discussion see section 3.3.5), but considered sufficient for achieving a first-order estimate (e.g. Guo et al., 2012; Chang et al., 2010; Dreiling et al., 2018). We observe that crack density is about $\sim$0.15 near the surface, which agrees with porosity estimates (Franzson, 2001) and gradually decreases to zero at a depth of 3 - 4 km, which we interpret as the crack closure depth.

The above result highlights two key points: (1) Crack density and closing depth are consistent with prior knowledge and demonstrate that radial anisotropy from surface waves is a reliable estimator of crack properties in heterogeneous shallow crust. (2) The fact that the

V_{SV} model derived from Rayleigh wave dispersion differs considerably from the body wave model near the surface shows that jointly exploiting both classes of data requires caution.

The latter point is significant since many ambient noise studies only use Rayleigh waves and therefore produce V_{SV} models. The higher near-surface velocities in this case suggest that combining these models with body wave data may lead to systematic errors. One common scenario is where a 1D V_{SV} model constrained by Rayleigh waves is used to locate local events when no other velocity model exists. For example, Johnson et al. (2010) located earthquakes at Okmok volcano, Alaska, using a velocity model derived from Rayleigh waves presented by Masterlark et al. (2010). Jolly et al. (2017) similarly used such a velocity model for locating events at White Island volcano, New-Zealand. In this scenario, using a velocity model that is faster than the actual velocities may cause earthquakes to appear deeper than they really are. To demonstrate this effect for the Askja region we relocate 200 events with manually-refined arrival time picks using our V_{SV} and V_{SH} models. The location process using NonLinLoc requires a V_P model. This is calculated by SURF96 during the inversion for V_S by maintaining the original V_P/V_S ratio. We treat the catalogue depth (located using the body-waves derived velocity model from Mitchell et al., 2013) as true depth and the depth change when locating using V_{SV} as “error”. We find an increase in depth of up to 3 km and an increase in root-mean-square error (RMS), which suggests that the location quality is lower (Fig. 4.6). We also see that for V_{SH} the depth and RMS increase are smaller, demonstrating that using V_{SH} models can help mitigate this issue. Another scenario where this may have an effect is teleseismic travel time tomography of the mantle. Since teleseismic body waves smear structure vertically beneath stations, a velocity model from surface waves may be used to constrain the crustal velocity structure. For our regional velocity models, a vertically incoming teleseismic shear wave will propagate $\sim$0.2s faster through the V_{SV} model compared to the V_{SH} model. In such a scenario, since the incoming body waves are mostly sensitive to V_{SH}, the artificially high crustal velocities will lead to the recovery of a slower mantle beneath. Another example is the joint inversion of receiver functions and Rayleigh wave dispersion data for Moho depth. In this case, the Moho depth may appear to be deeper than it really is due to the higher velocities.

4.4.2 Azimuthal anisotropy

The group velocities of surface waves in an anisotropic medium with sub-vertical cracks are expected to vary with azimuth (Smith and Dahlen, 1973; Crampin and Taylor, 1971; Mindevalli and Mitchell, 1989) and can be used to estimate the dominant crack orientation if one exists. Rayleigh wave velocities are expected to vary as approximately:

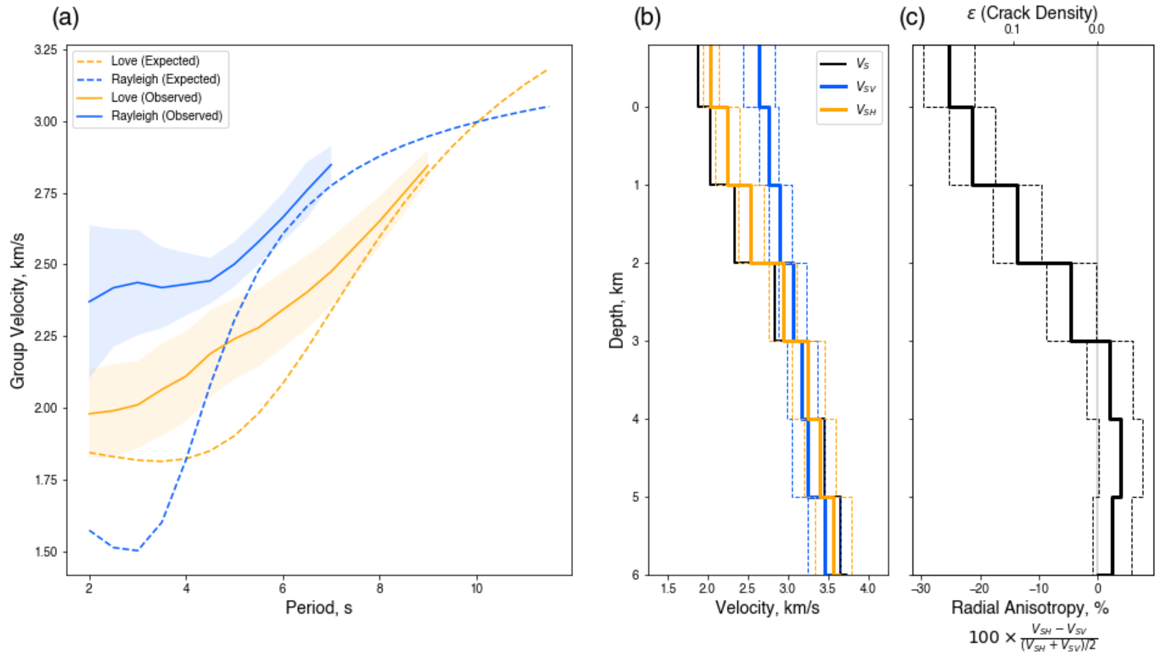

Fig. 4.5 **a** Solid lines show the observed mean group dispersion curves for Love (orange) and Rayleigh (blue) waves with their standard deviations (shaded regions). Dashed lines show group velocities predicted by the regional 1D V_S body wave model. **b** Black line indicates the regional 1D V_S model obtained from body waves. Orange and blue lines show the 1D V_{SH} and V_{SV} models constrained by inversion of the mean Love and Rayleigh wave group dispersion curves respectively, with their standard deviation shown by the dashed lines. **c** Black line shows the radial anisotropy calculated from the surface wave V_{SH} and V_{SV} models on the bottom horizontal axis and the estimated crack density calculated using an approximate relationship with anisotropy on the top horizontal axis. For panels **b** and **c** depth is bsl

$$U_R(\theta) = U_0 + A \cdot \cos(2(\theta - \varphi)) \tag{4.1}$$

where θ is the azimuth of the propagating surface wave with the peak velocity parallel to the strike of the cracks. Love wave velocities are expected to vary as approximately:

$$U_L(\theta) = U_0 + A \cdot \cos(4(\theta - \varphi)) \tag{4.2}$$

with one of two slow directions parallel to the strike of the cracks. Figure 4.7 from Mindevalli and Mitchell (1989) demonstrates the azimuthal variations in surface wave velocity in the presence of cracks from lab and theoretical studies.

We fit these expressions to their respective datasets using a non-linear least-squares fitting procedure (Fig. 4.8a,b). We observe that the orientation of the peak velocity of the best-fit sinusoid for Rayleigh waves is 23° and the two troughs of the best-fit sinusoid for Love

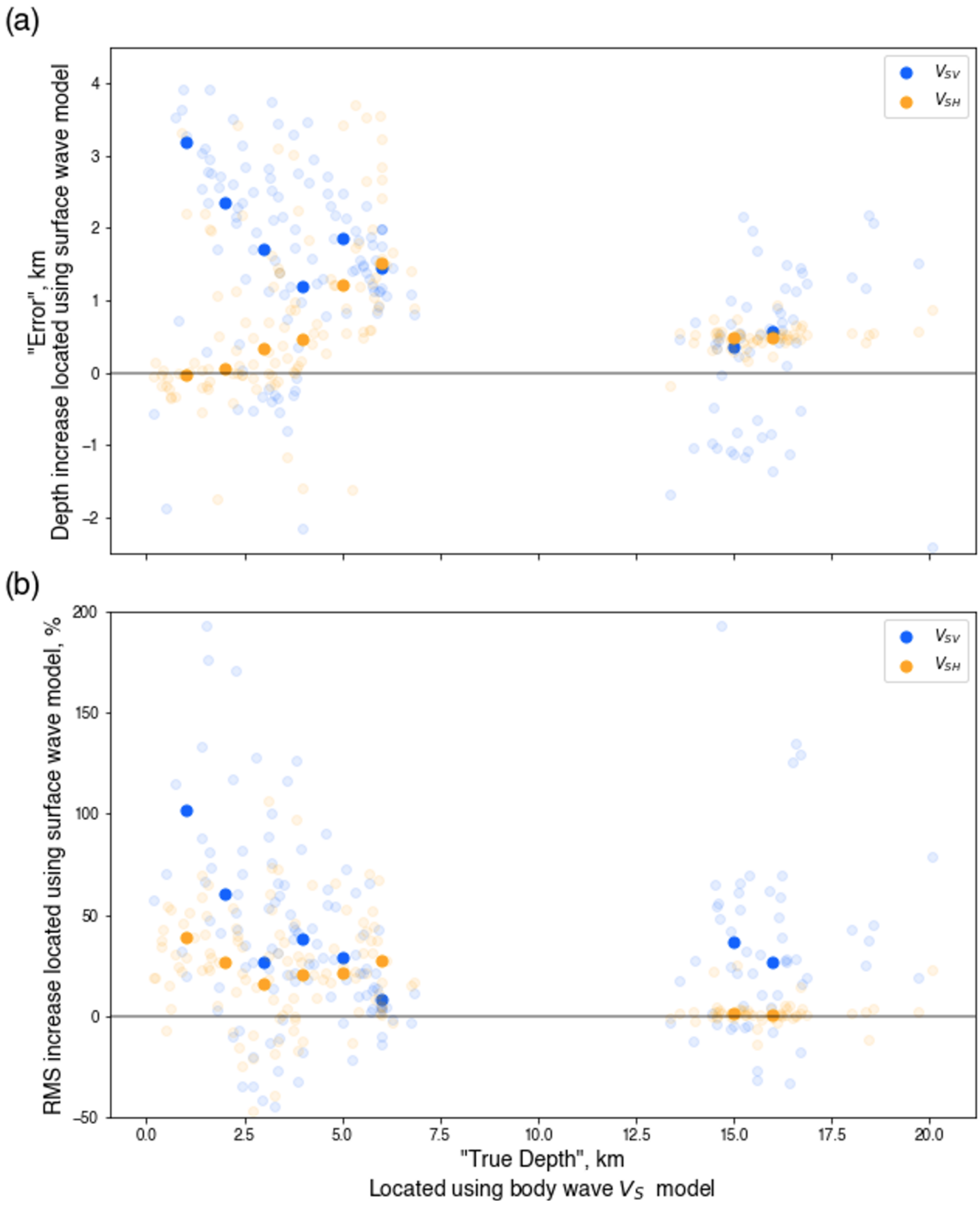

Fig. 4.6 **a** the x axis shows the depth at which events were located using a 1D shear wave velocity model constrained by local earthquake arrival times. The y axis shows the increase in depth when the locations are carried out using a 1D model derived from ambient noise surface waves. Blue dots indicate the located depths from the V_{SV} model and the orange dots the depths from the V_{SH} model. Each transparent dot represents an event and the solid dots are the result of binning the events using a 1 km depth window. Only bins with more than 10 measurements are displayed. **b** is similar to a but the y axis represents the increase in the RMS body wave travel time residuals.

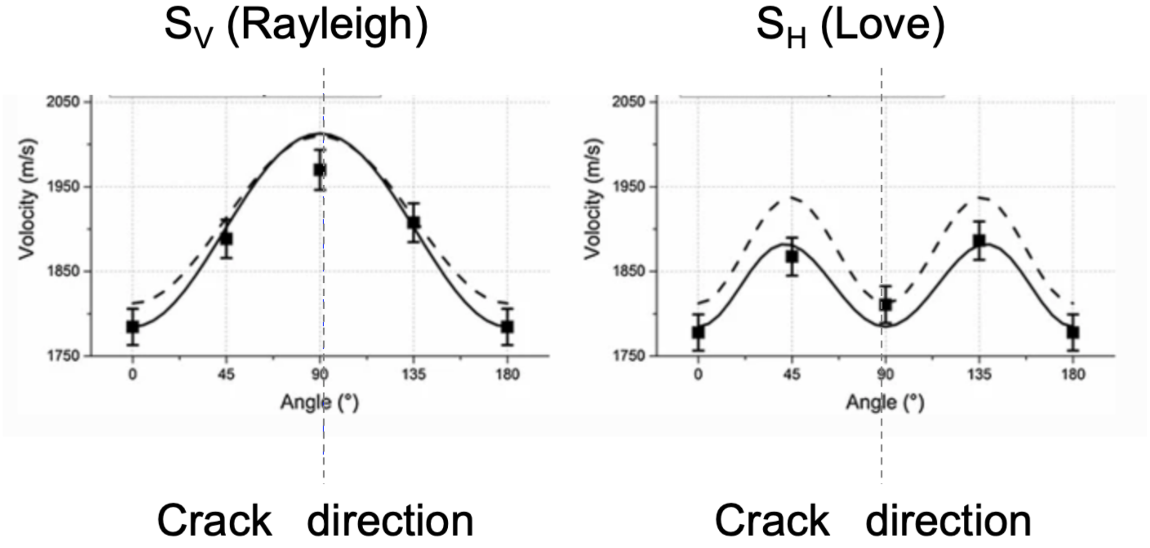

Fig. 4.7 Expected azimuthal anisotropy from oriented cracks using lab and theoretical results from Mindevalli and Mitchell (1989). Squares represent lab results. Solid and dashed lines represent theoretical values using slightly different assumptions.

waves are at 28° and 118°, suggesting a main crack orientation of 23-28°. We use F tests to determine whether the sinusoid fits the data better than a random distribution. For the Love wave result, F tests suggest that the fit is statistically significant for all tested periods, whereas for the Rayleigh wave result the fit is significant for periods 2s and 3s and becomes worse at longer periods (Fig. 4.9). We attribute this to the fact that Rayleigh waves are sensitive to deeper structure and at longer periods their peak sensitivity is at depths (Fig. 4.10) where crack density diminishes. We then compare our results to a detailed field mapping study of crack orientations (Hjartardóttir, Einarsson and Sigurdsson, 2009) and measurements of fast shear wave splitting directions from local shallow earthquakes (Bacon et al., 2019) (Fig. 4.8c) around Askja. In a medium hosting subvertical cracks, the fast shear wave is polarized in the plane parallel to the dominant strike of these features (Crampin, 1978) and therefore fast splitting directions indicate the azimuth of cracks. We can clearly observe that the distribution of both the mapped crack strikes and fast shear wave splitting directions are centred near the expected azimuth predicted by surface waves.

Field mapping and shear wave splitting also shows that the crack orientation is most coherent in the area surrounding the caldera and becomes more random within the edifice where caldera related processes dominate over rifting processes. If we restrict our data to only short ray paths that are contained within the edifice, we indeed find no significant azimuthal fit.

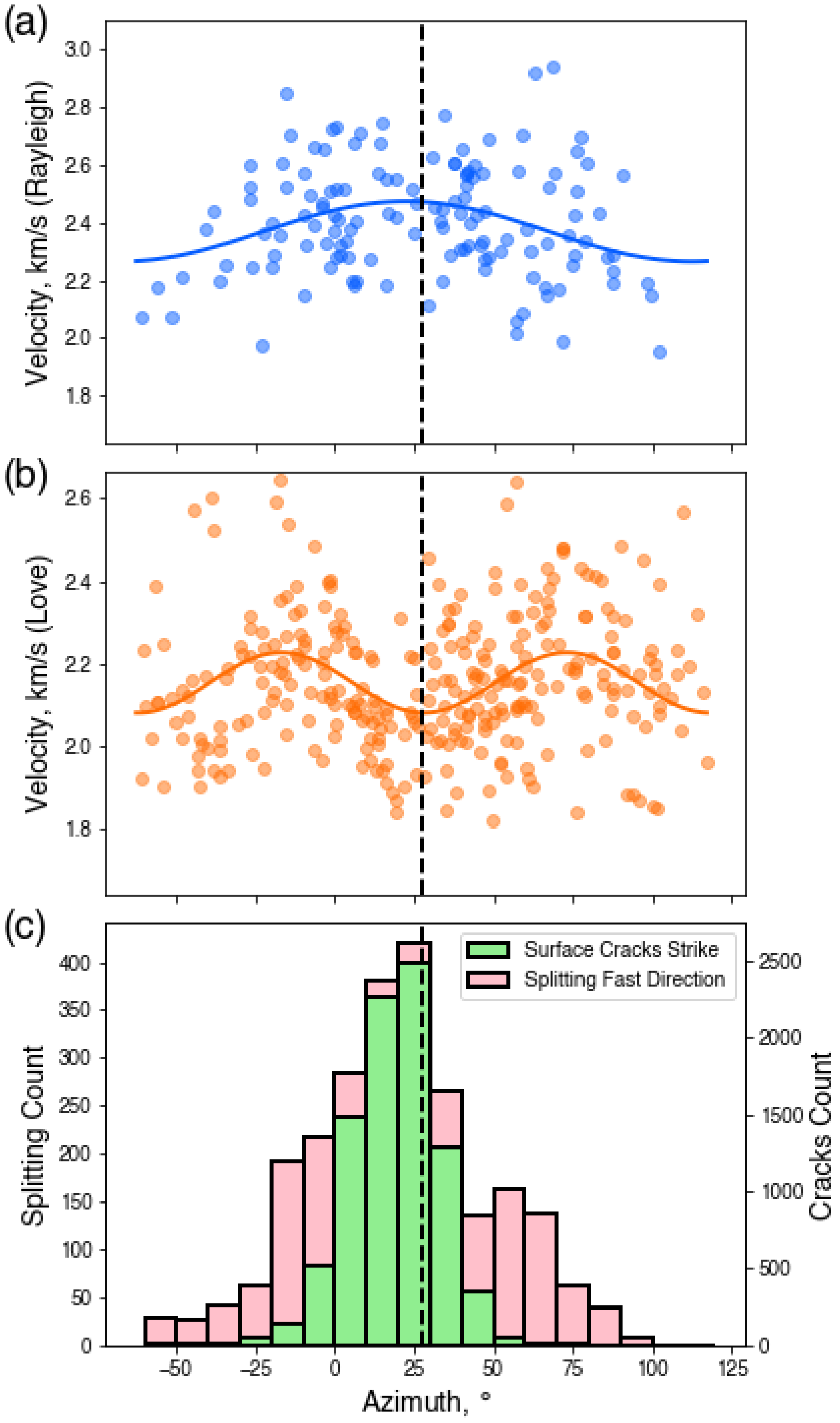

Fig. 4.8 **a** Scattered points show measurements of Rayleigh wave group velocity at a period of 2 s versus azimuth. The solid line is the best fitting 2 cosine showing a peak velocity at an azimuth of 23°. **b** Scattered points show measurements of Love wave group velocity at a period of 4s versus azimuth. The solid line is the best fitting 4θ cosine showing two troughs at 28° and 118°. **c** The pink histogram shows counts of fast splitting measurements from local shallow (depth < 4km) earthquakes. The green histogram shows counts of crack strikes mapped at the surface. Both histograms are centred near ~25°. A dashed vertical line is plotted on all panels at 28° to help facilitate comparison of the different datasets.

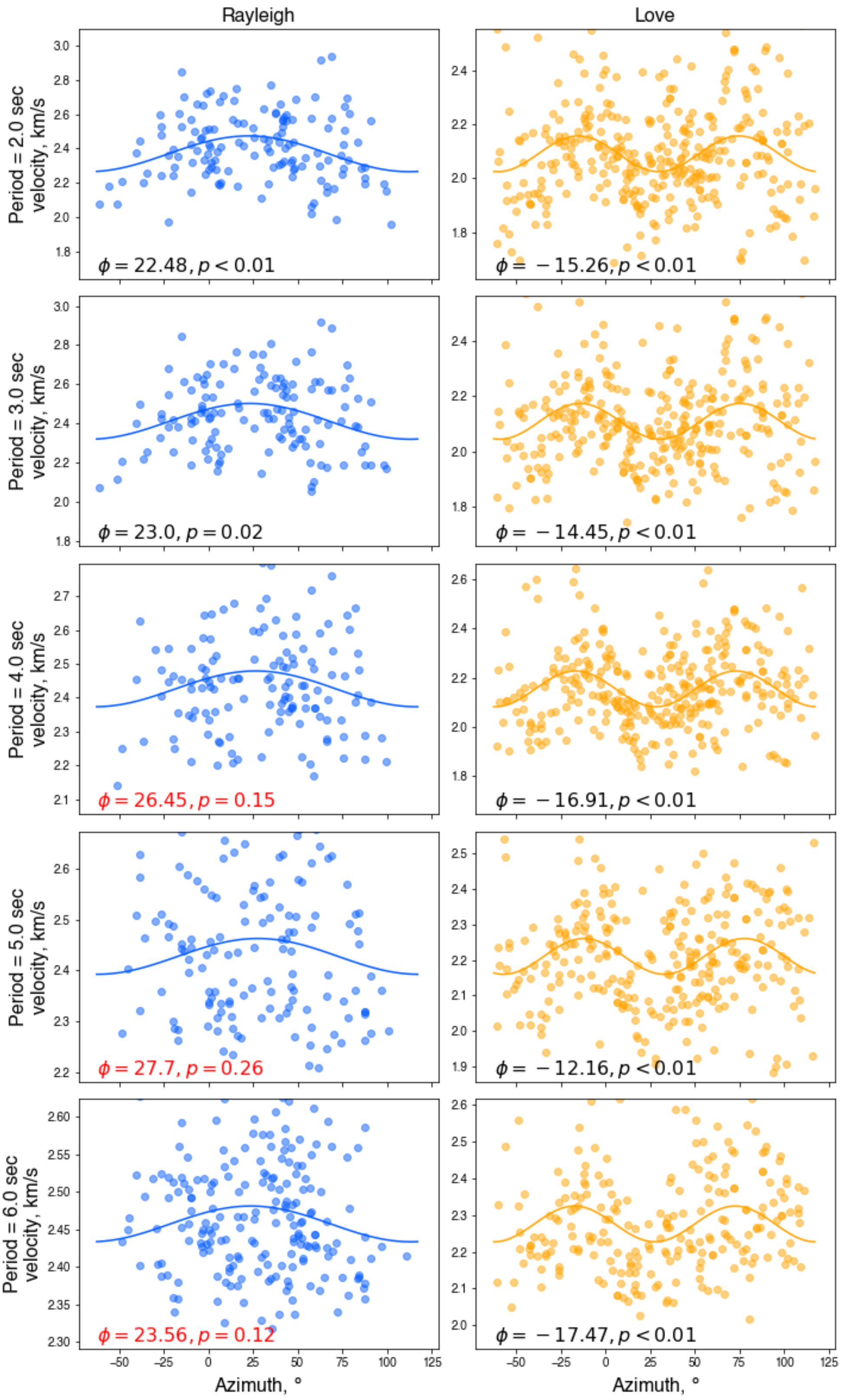

Fig. 4.9 Scattered points and solid lines are the same as Figure 4.8 but for different periods. The left column shows Rayleigh data and the right shows Love data. For each panel, the best fit ϕ value from the relevant equation (eq. 4.1 for Rayleigh and eq. 4.2 for Love) is displayed at the bottom left corner together with the p value indicating the statistical significance of the fit. Text in red colour indicates $p > 0.05$. It can be seen that for Love the fit is statistically significant for all tested periods, whereas for the Rayleigh wave result the fit is significant for periods 2 s and 3 s and becomes worse at longer periods.

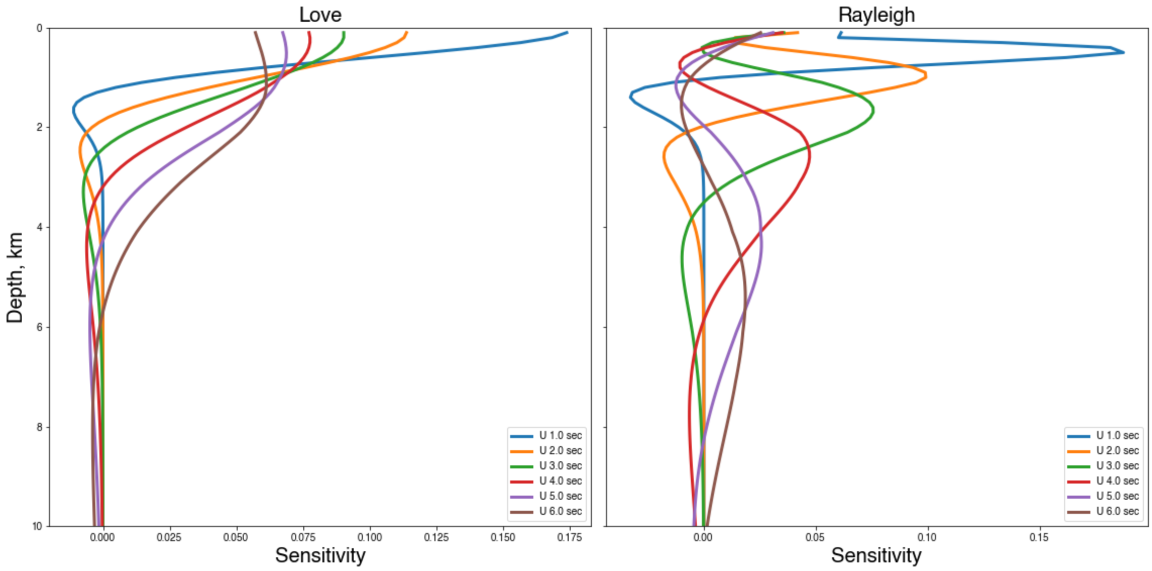

Fig. 4.10 Group velocity sensitivity kernels for Love and Rayleigh waves calculated using a 1D regional velocity model from Mitchell et al. (2013).

This result shows that surface waves extracted from ambient noise can be a reliable tool for estimating crack orientation when body waves and/or field mapping are not available. The main crack orientation provides useful insight into the local tectonics since it is expected to be perpendicular to the local extension direction, which can be inferred from our result to be ∼118°- 298°.

4.4.3 3D shear velocity structure

In this section we invert the inter-station group travel times for 3D shear velocity structure using the so called two step method and compare our results to an existing 3D shear velocity model from local body waves presented by Greenfield et al. (2016). First, we invert the group travel times for 2D group velocity maps at periods 2 - 7 seconds (Fig. 4.11). The RMS travel time reduction was 11% and 20% on average for Rayleigh and Love waves respectively. These are relatively small reductions, which we attribute in part to the strong azimuthal anisotropy presented in the previous section and is not accounted for by the isotropic inversion. Synthetic recovery tests (Fig. 4.12) indicate that under the caldera (denoted by black lines) the path coverage is sufficient to resolve anomalies of 10x10 km, similar to the size of the caldera. Random noise with a Gaussian distribution and 0.5 s standard deviation was added to the synthetic data. The most obvious feature in the Rayleigh group maps is what appears to be a circular slow anomaly directly under the caldera, best seen at a period of 4 s. The Love wave group velocity map also shows the region under the caldera as slow but the encircling fast feature seen in the Rayleigh wave model is not as clear and does not exist to the south west.

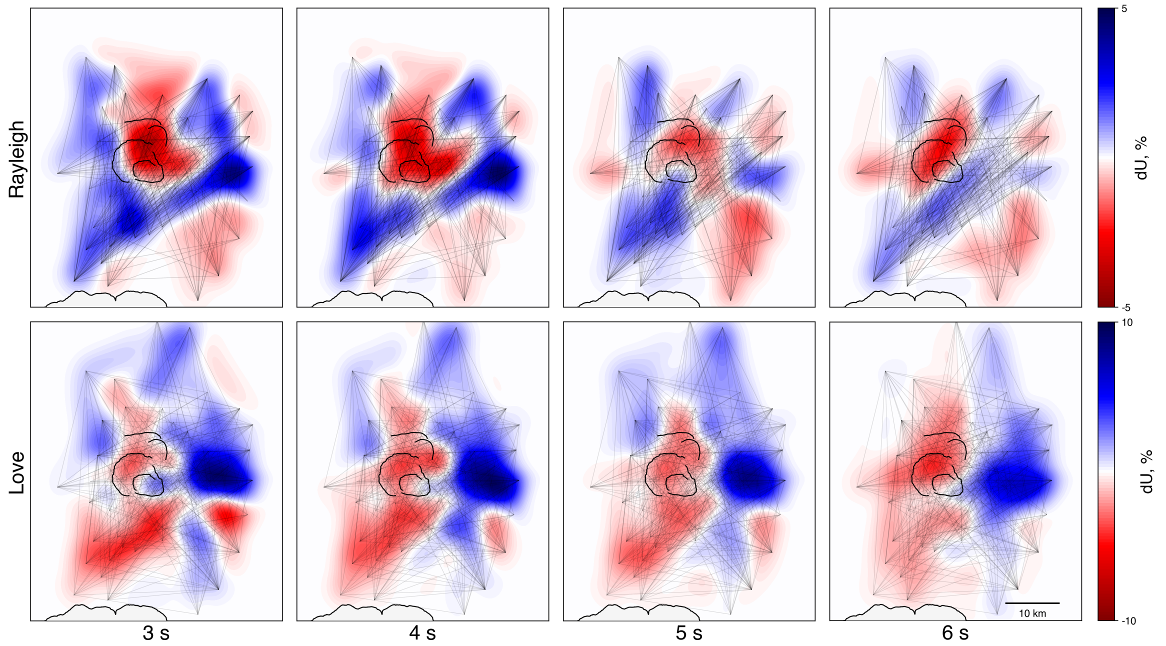

Fig. 4.11 Group velocity perturbation maps at periods 3-6 s. Black lines indicate ray-paths used in the inversion. Perturbation is shown as a percent from the starting model.

Next, we extract pseudo dispersion curves from the model at a spacing of 2 km and invert them for shear velocity and depth using the approach defined in Section 4.3.3 with 100 starting models per dispersion curve. We combine the inverted velocity profiles to produce separate full 3D shear velocity models for V_{SV} and V_{SH}. The resulting 3D models are presented in Figure 4.13 using depth slices from 1 to 4 km depth. Columns from left to right display V_{SV}, V_{SH}, isotropic shear velocity calculated as a Voigt average $V_S = \sqrt{(2V_{SV}^2 + V_{SH}^2)/3}$ (Dziewonski and Anderson, 1981) and radial anisotropy. No smoothing has been applied to the data after joining the independent velocity profiles. Before we discuss the results is important to note two limitations of our analysis. (1) Since surface waves naturally smear vertical structure due to their smooth sensitivity kernels, they do not provide good depth constraints (vertical cross sections are shown section B.2.1) (2) When computing radial anisotropy in %, the division means that small errors in the denominator can lead to very large changes in absolute values. We therefore avoid interpreting these values and only discuss it in terms of high or low radial anisotropy.

Both models, as well as the calculated V_S, display a circular slow anomaly under the caldera encircled by a fast feature. This is most obvious in the V_S model at 0 - 2 km depth bsl, and in the V_{SV} and V_{SH} models at 2 km depth bsl. The main finding of the body wave

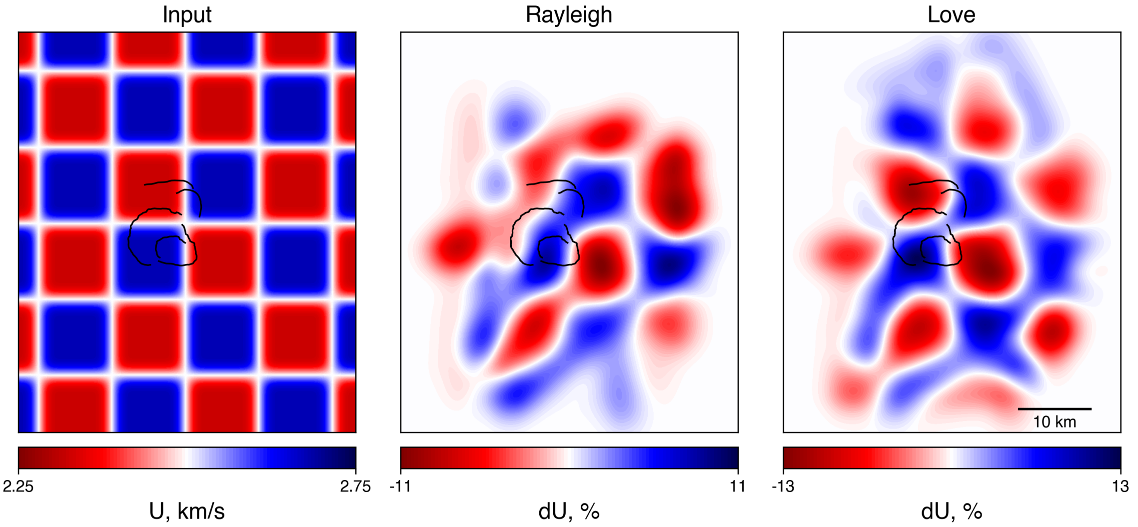

Fig. 4.12 Synthetic recovery tests for the isotropic group velocity inversion. **a** The input model. The colour scale indicates group velocity. The synthetic anomaly size is 10x10 km **b** The recovered model for Rayleigh waves. The color scale indicates group velocity perturbation relative to the starting model used in the inversion. **c** Same as **b** but for Love waves.

tomography in Greenfield et al. (2016) (Fig. 4.14d-f) in the upper crust was a slow anomaly with high V_P/V_S ratio under the caldera centred at ∼5km (bsl), which was interpreted as a hot region of melt storage (∼10% melt). At shallower depths comparable to the slow anomaly we observe, the body wave tomography did not resolve a similar feature, but rather a fast anomaly (Fig. 4.14a-c). However, a number of studies (De Zeeuw-van Dalfsen et al., 2012; Rymer and Tryggvason, 1993; Sturkell and Sigmundsson, 2000; Sturkell et al., 2006; Pagli et al., 2006) using InSAR, GPS and microgravity data have observed long term subsidence and mass changes at Askja which are best explained by a deflating magma body under the centre of the caldera. The geodetic data was best fitted by a Mogi source (Mogi, 1958) at a depth of 2.8 - 3.5 km with a volumetric decrease of 0.0012 – 0.0017 km^3/yr. While the Mogi source modelling did not provide information about absolute volume, De Zeeuw-van Dalfsen et al. (2012) also attempted to fit the data with a deflating penny shaped horizontal crack which gave a best fitting radius of 1.7 - 2.3 km and can at least provide a rough estimate of the lateral extent. The centre of the modelled deflating body, denoted as a black star in Figure 4.13, is laterally very close to the centre of the slow anomaly we observe. Such a magma body would appear in tomographic images as an area of lower velocities under the centre of the caldera with a high V_P/V_S ratio. As previously mentioned, Greenfield et al. (2016) did not find such an anomaly, but showed through the use of synthetic tests that even if such a magma body existed, it would be poorly constrained by the body wave dataset

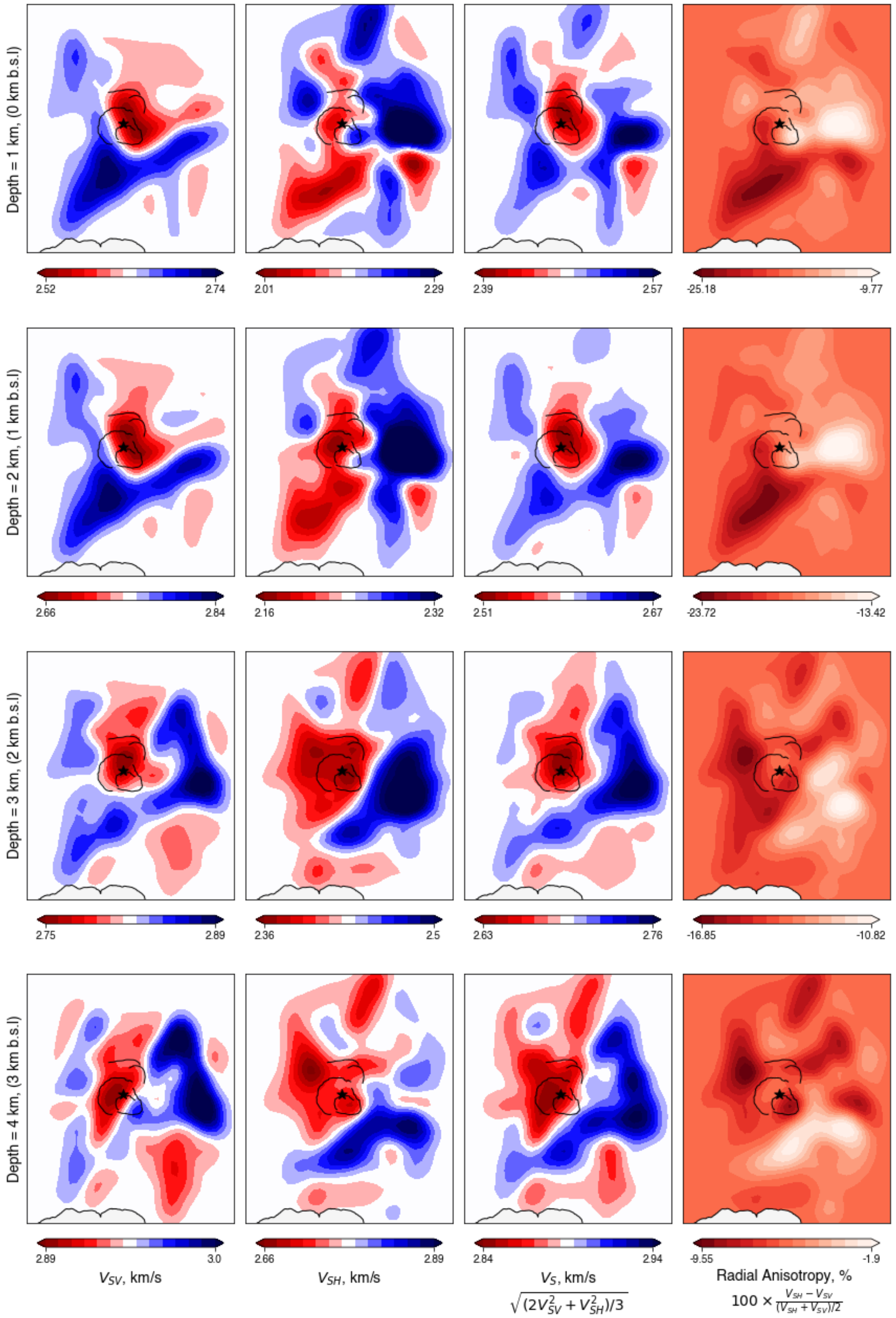

Fig. 4.13 3D Shear velocity structure and radial anisotropy of Askja. Columns from left to right display V_{SV}, V_{SH}, isotropic V_S and radial anisotropy. The centre of the modelled deflating body from De Zeeuw-van Dalfsen et al. (2012) is denoted as a black star. Associated estimated error maps are shown in Fig B.4

they used. They additionally found that rays crossing the location of the predicted magma body were significantly attenuated which would be consistent with the presence of melt. It is therefore possible to interpret the slow anomaly we observe under the caldera as the shallow magma body predicted by the geodetic data. However, we remain cautious as many other reasons exist for velocity anomalies under volcanoes (Lesage et al., 2018), such as temperature, lithology, porosity, water content, etc. To more decisively interpret melt, V_P/V_S ratio and/or attenuation are required but are not solved for by our inversion technique.

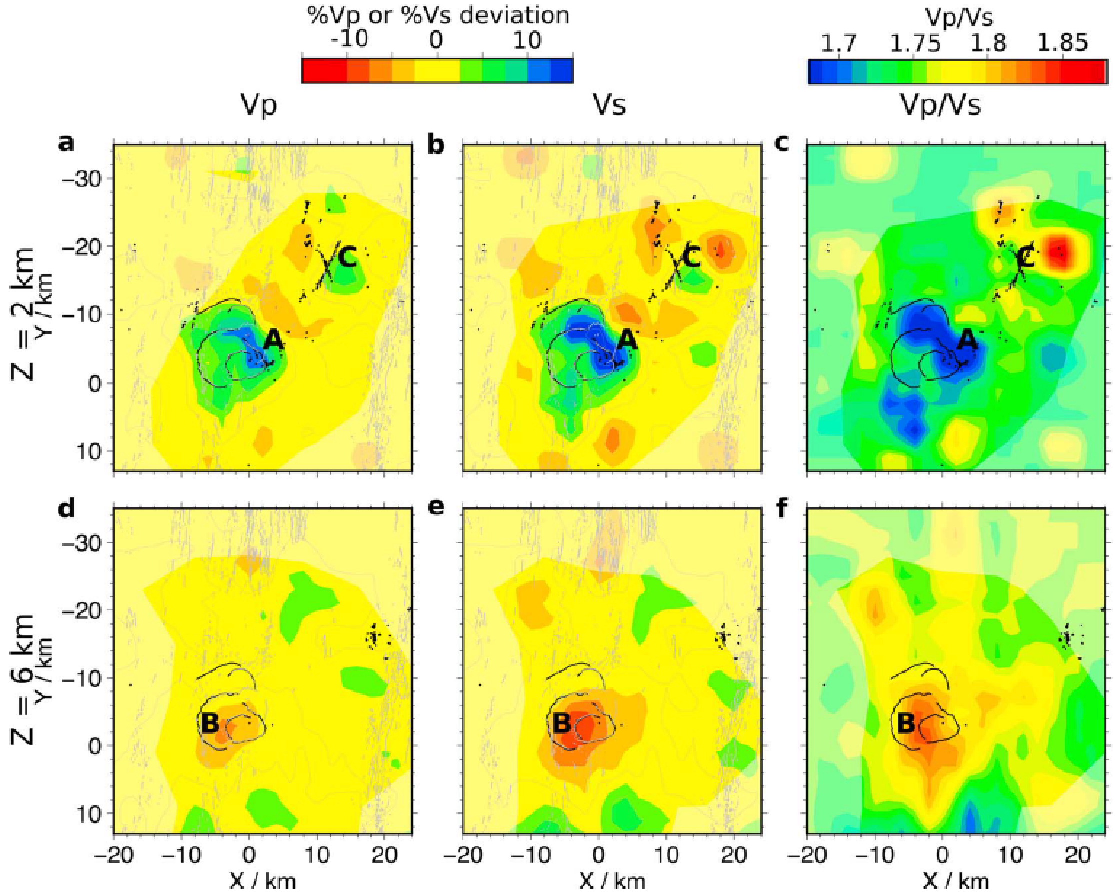

Fig. 4.14 3D velocity structure of Askja from body waves reproduced from Greenfield et al. (2016) showing depth slices at 2 km bsl and 6 km bsl through the V_P,V_S and V_P/V_S models. The V_P and V_S models are plotted as percentage deviations from the starting model, and the V_P/V_S is plotted as absolute value.

To more directly compare our results to the geodetic studies, we perform a synthetic recovery test (Fig, 4.15)where the input model has a circular slow anomaly with a radius of 2.3 km, and is centred at 65.05°N 16.78°W, as modelled in De Zeeuw-van Dalfsen et al. (2012). Random noise with Gaussian distribution and a standard deviation of 0.5 s is added to the synthetic data. The results show that both the Love and Rayleigh datasets are able to resolve the slow anomaly but the recovered anomaly is somewhat larger. It can also be seen that in Figure 4.13 the centre of the slow anomaly we observe is slightly north of the modelled location of the deflating body. This northward shift is not recreated in the synthetic recovery test, suggesting that if we are indeed seeing the deflating magma body predicted by the geodetic studies, its centre is about ∼2 km north of its suggested location.

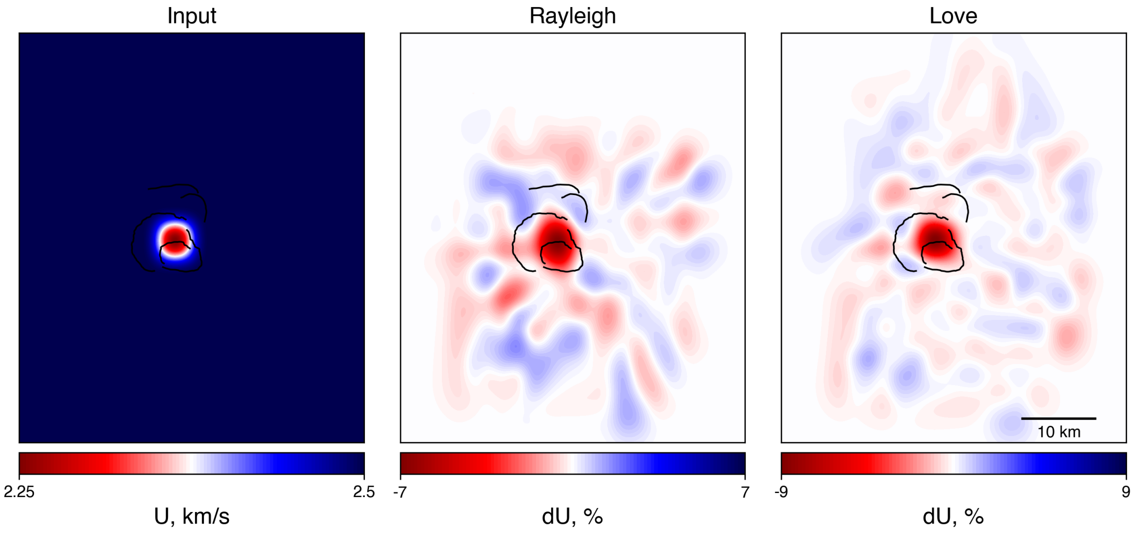

Fig. 4.15 Synthetic recovery test for the isotropic group velocity inversion with. **a** The input model has a circular slow anomaly with a radius of 2.3 km, and a is centred at 65.05°N 16.78°W, as modelled in De Zeeuw-van Dalfsen et al. (2012). The colour scale indicates group velocity. **b** The recovered model for Rayleigh waves. The color scale indicates group velocity perturbation relative to the starting model used in the inversion. **c** Same as **b** but for Love waves.

Another interesting feature which can be observed in Figure 4.13 is the region of strongly negative radial anisotropy south-east of the caldera at depths of 1 - 2 km. Assuming cracks are the main cause of negative radial anisotropy in the region, this could be interpreted as a region of higher crack density. We do not observe any radial anisotropy features which are clearly associated with the caldera as has been observed in other volcanoes using similar analysis (e.g. Mordret et al., 2015; Spica et al., 2017; Jaxybulatov et al., 2014). These works, which observe radial anisotropy features directly under the caldera, often interpret them using dyke (positive radial anisotropy) and/or sill (negative radial anisotropy) complexes. It is therefore possible that such complexes do not exist under Askja, at least at the depths we image. None of the volcanoes studied in the cited works above are a mid-ocean ridge volcano which might also be part of the reason for the lack of such features. Another explanation is that such complexes exist but our imaging is not able to resolve them. As we have seen, the Askja region displays significant azimuthal anisotropy which is not modelled here and may reduce the resolution of the 2D isotropic velocity maps in the first step of the two step method.

To conclude this section, the ambient noise tomography results display a shallow slow anomaly consistent with a deflating magma body predicted from geodetic data. This anomaly was not resolved by body wave tomography, demonstrating how the two dataset can complement each other. Our findings suggests that our understanding of Askja could benefit from further work involving a joint inversion of body waves and surface wave, and from an inversion that allows for azimuthal anisotropy which appears to be significant here.

4.5 Conclusion

We have presented a comparison between results obtained by using surface wave dispersion extracted from ambient noise and results obtained by using body waves from local earthquakes and field mapping in a shallow heterogenous environment. Our results indicate that the radial and azimuthal anisotropy results from surface waves are extremely useful for assessing bulk crack properties such as density and orientation, since they agree with other methods which are not always available in other regions. Furthermore, our results show that in the presence of sub-vertical cracks, using a V_{SV} model constrained by Rayleigh waves jointly with body waves, for example in the case of earthquake depth location, may introduce errors since the V_{SV} models are generally faster. We suggest that this issue may be mitigated by using V_{SH} models from Love waves or by correcting Rayleigh velocities according to crack property estimates. Finally, 3D V_{SV} and V_{SH} models obtained from a two-step inversion approach resolve a shallow slow anomaly that coincides with the location of a magma body predicted by geodetic studies at a depth of 2 - 3 km but was not imaged by the body wave tomography.

Chapter 5

Ambient noise tomography of Iceland

5.1 Chapter abstract

Iceland, which sits atop the northern mid-Atlantic ridge, provides a rare opportunity for studying a mid ocean ridge using land-based methods. Here, we use ambient noise cross correlation to measure Love and Rayleigh phase velocities in the period range 4 - 16 s. Due to the large size of the dataset, we develop an automatic tool for picking phase velocity dispersion curves. We use the automatic process developed to pick more than 3500 dispersion curves. We then invert the phase velocities to produce 2D phase velocity maps, including the first ever such map for Love waves in Iceland. We show that similar to Rayleigh phase velocities, Love phase velocities in Iceland display slow anomalies along the rift zones where young rock is exposed. This reinforces the previously suggested mechanism involving reduction of porosity with crustal age through weathering. We observe that within the rift zones, the slowest velocities correspond to large volcanic centres which we attribute to regional melt storage.

5.2 Introduction

Iceland straddles the mid-Atlantic Ridge spreading centre where the North American and Eurasian tectonic plates diverge and is one of the only places in the world where an active mature spreading ridge is exposed above sea level. The ridge in Iceland is slow spreading at a rate of rate 18.5mm/y and has an azimuth of 106° (DeMets et al., 2010). On shore, spreading is accommodated in three volcanic rift zones (Fig. 5.1): the sub parallel Western and Eastern Volcanic Zones (WVZ and EVZ) in southern Iceland, and the Northern Volcanic Zone (NVZ) in northern Iceland. It is believed that the sub parallel sections are the result of a rift jump in progress from the WVZ, which is dying out over time, to the EVZ (Hardarson et al., 1997). The high levels of crustal volcanism compared to normal spreading ridges has given rise to the hypothesis that a mantle plume exists in the underlying mantle beneath Iceland (White and McKenzie, 1989). This interpretation is supported by a geoid anomaly (Marquart, 1991) as well as geochemical and petrological evidence (White et al., 1992).

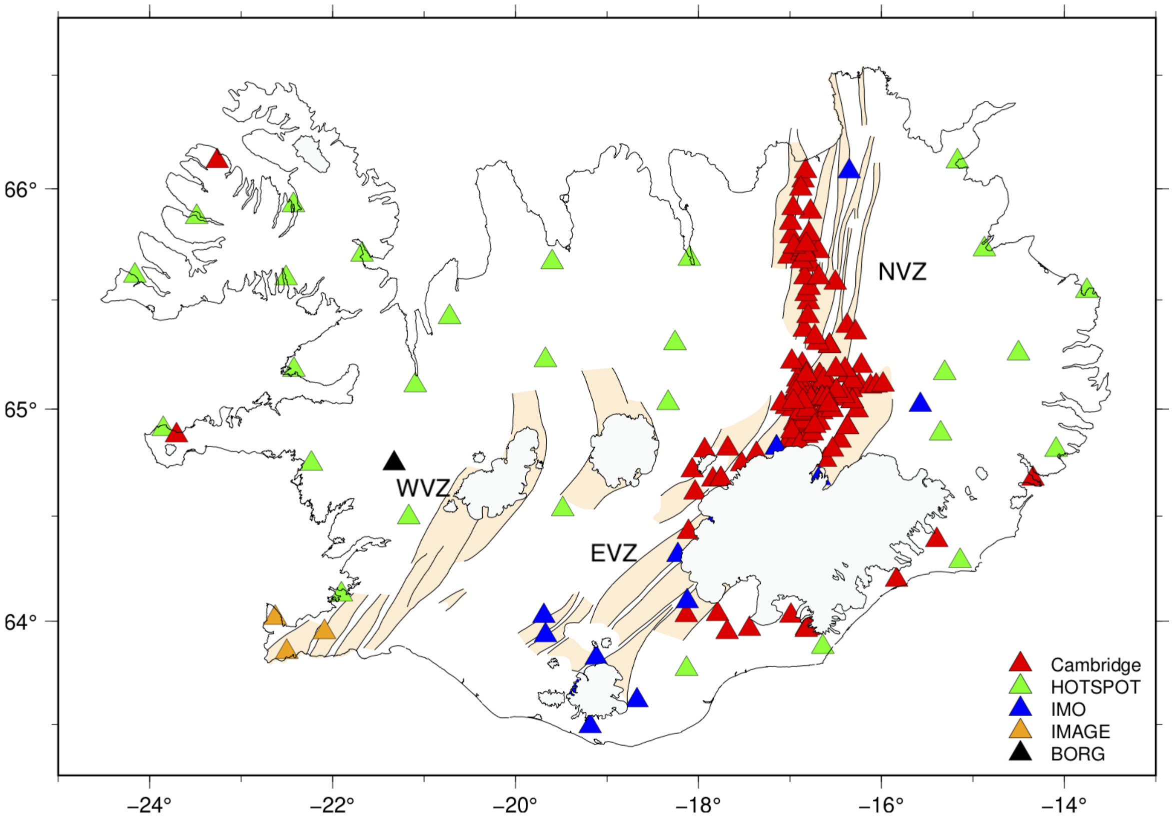

Fig. 5.1 Map of Iceland showing the location of seismic stations used in this work. Triangles denote stations and different networks are indicated by colours.

Due to its unique tectonic setting, Iceland has been the target of a number of seismic tomography studies. In the mantle, teleseismic and global travel time tomography (Fig. 5.2a-c) has revealed a narrow cylindrical low velocity anomaly with a radius of ∼300 km extending to a depth of at least 400 km below Iceland (Wolfe et al., 1997; Foulger et al., 2001; Allen et al., 2002; Bijwaard and Spakman, 1999), usually interpreted as the hypnotized upwelling mantle plume. Regional (French and Romanowicz, 2015)(Fig. 5.2d) and global (Rickers et al., 2013)(Fig. 5.2e) full-waveform tomography appear to show that the mantle plume extends well into the lower mantle.

In the crust, two active source experiments (Fig. 5.3a-b) , called FIRE and ICEMELT (Brandsdóttir et al., 1997; Staples et al., 1997; Darbyshire et al., 1998, 2000), found a highly variable crustal thickness from 40 km under Vatnajökull icecap to less than 20 km beneath the rift zones. These studies also discovered very high P wave velocities of up to 7.2 km/s in the lower crust. Regional surface wave and body wave tomography revealed the 3D structure of the crust (Fig. 5.3c) and a large slow shear wave anomaly along the rift zones (Fig. 5.3e)(Allen et al., 2002). Ambient noise group velocity tomography (Fig. 5.3f) improved the resolution of the crustal model, revealing two narrow and distinct slow anomalies along the separate rift zones (Green et al., 2017) in southern Iceland, corresponding the exposure of young rock (Fig. 5.3g). Joint inversion of surface waves and receiver functions (Jenkins et al., 2018) yielded a detailed 3D crustal thickness map (Fig. 5.3d) and found a mid-crustal discontinuity at $\sim$20 km depth, interpreted as a compositional transition between a mostly gabbroic middle crust to olivine enriched lower crust. In light of the extensive tomographic imaging already done, our work aims to build on existing models by exploiting both Rayleigh and Love wave dispersion data and presenting the first ever Love wave velocity maps in Iceland.

5.3 Data and Methods

5.3.1 Seismic Data

This study uses 3-component continuous broadband waveforms from five seismic networks (not all overlapping in time) with a total of 189 stations deployed across Iceland (Fig. 5.1). 145 stations are sourced from a dense ongoing deployment operated by the University of Cambridge, mostly covering the NVZ and the EVZ. Additional data includes 10 permanent stations from the Icelandic Meteorological Office (IMO) network, 3 stations from the IMAGE project Reykjanes Ridge experiment, 30 stations from the HOTSPOT experiment (Allen et al., 1999) and the permanent station BORG from the Global Seismic Network. We only used station pairs which were simultaneously operational for at least 60 days. Data availability was slightly different for the vertical and the horizontal components, thereby yielding giving a total number of 4140 and 3470 potential station pairs for analysis, respectively.

5.3.2 Noise Cross-Correlations

First, the waveforms at all available stations are preprocessed following Bensen et al. (2007) and all possible station pairs are cross-correlated and stacked using phase-weighted stacking (Ventosa et al., 2017), giving a Noise Cross-Correlation Function (NCF) for each station pair. Since diffrent types of instrumentes are used, the instrument reposose is removed before cross correlation and the record is convolved with the reponse of a Guralp 6TD, which is the

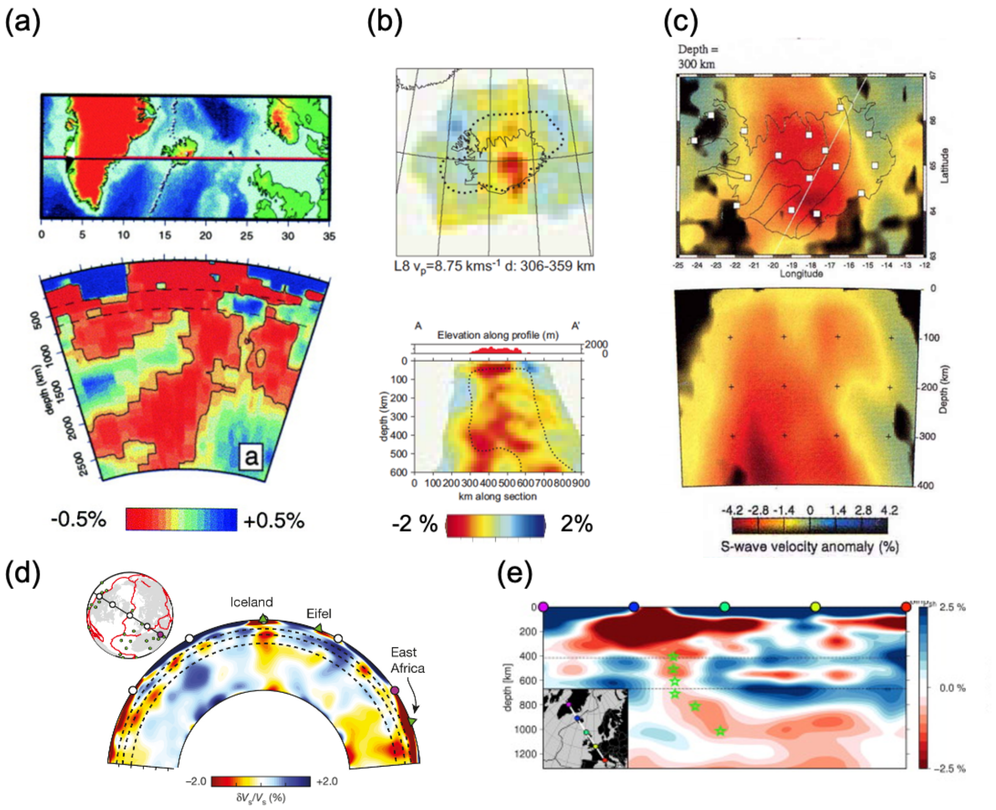

Fig. 5.2 Summary of previous seismic imaging of the mantle beneath Iceland: **a** global arrival tomography from Bijwaard and Spakman (1999), **b** teleseismic tomography from Foulger et al. (2001) and **c** Wolfe et al. (1997), **d** Global French and Romanowicz (2015) and **e** regional Rickers et al. (2013) full-waveform tomography

instrument with narrowest response used here. We use the vertical and radial components for Rayleigh waves velocities and the transverse component for Love waves. Plotting the NCFs as a function of station separation displays a move-out pattern as seen in Figure 5.4, indicating the signal observed on the NCF is indeed a function of the path between the two stations.

The EGF can then be calculated from the NCF by averaging the causal and acausal parts and taking the derivative (Lin et al., 2008):

$$EGF_{AB} = -\frac{d}{dt}\left[\frac{NCF_{AB}(t) + NCF_{BA}(-t)}{2}\right], \quad 0 \leq t \leq \infty \tag{5.1}$$

An example EGF for stations K250 and SYLG is shown in Figure 5.5a.

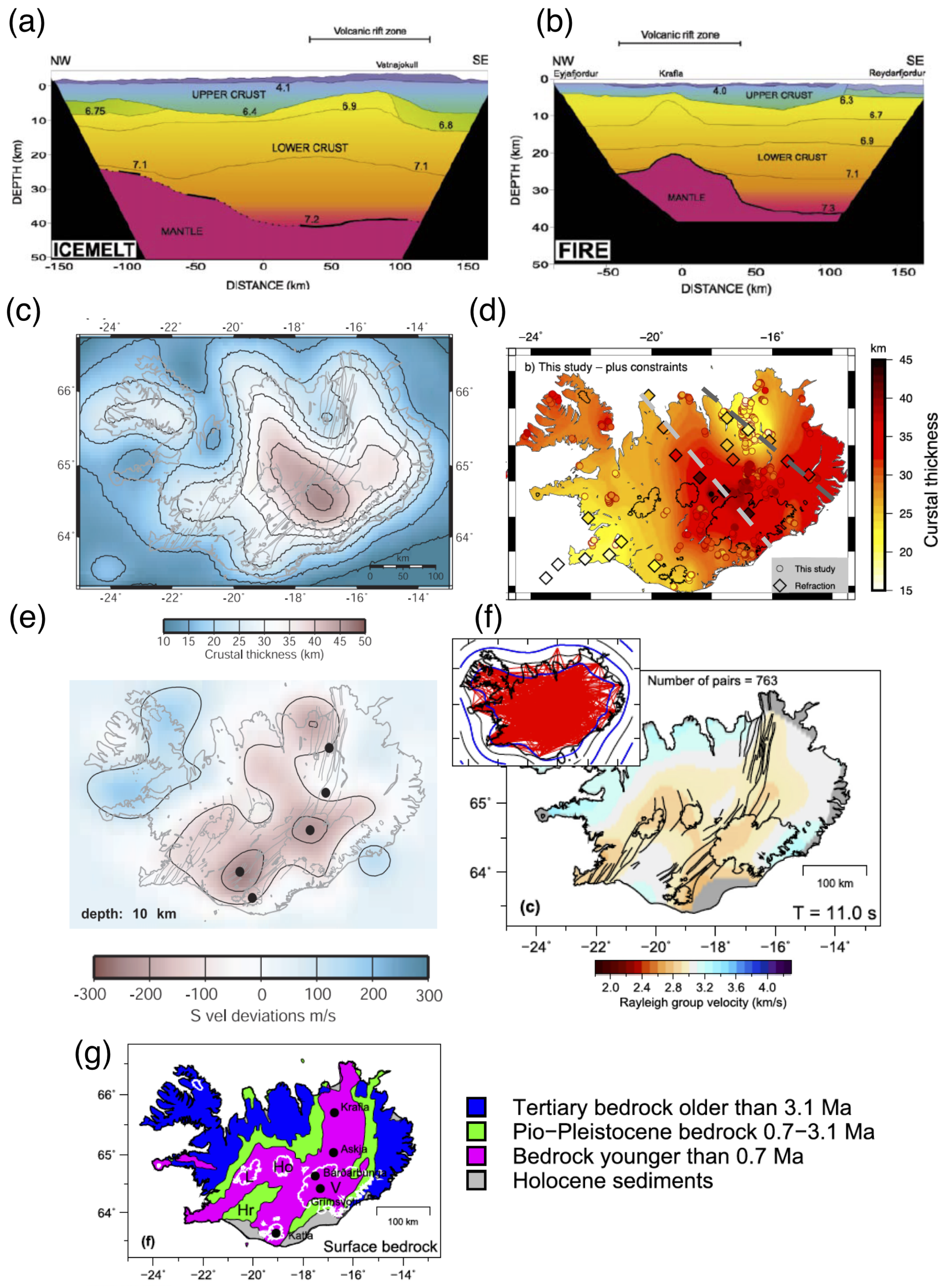

Fig. 5.3 Summary of previous seismic imaging of the crust in Iceland. **a - b** ICEMELT and FIRE - Spreading ridge perpendicular cross sections with V_P velocities from Staples et al. (1997) and Darbyshire et al. (1998). The location of FIRE and ICEMELT are shown in **d** as dashed light and dark grey lines respectively. **c** Crustal thickness map from Allen et al. (2002). **d** Same as **c** from (Jenkins et al., 2018). **e** Shear velocity perturbation map from Allen et al. (2002). **f** Rayleigh Group velocity map from Green et al. (2017). **g** Schematic geological map of Iceland from Green et al. (2017).

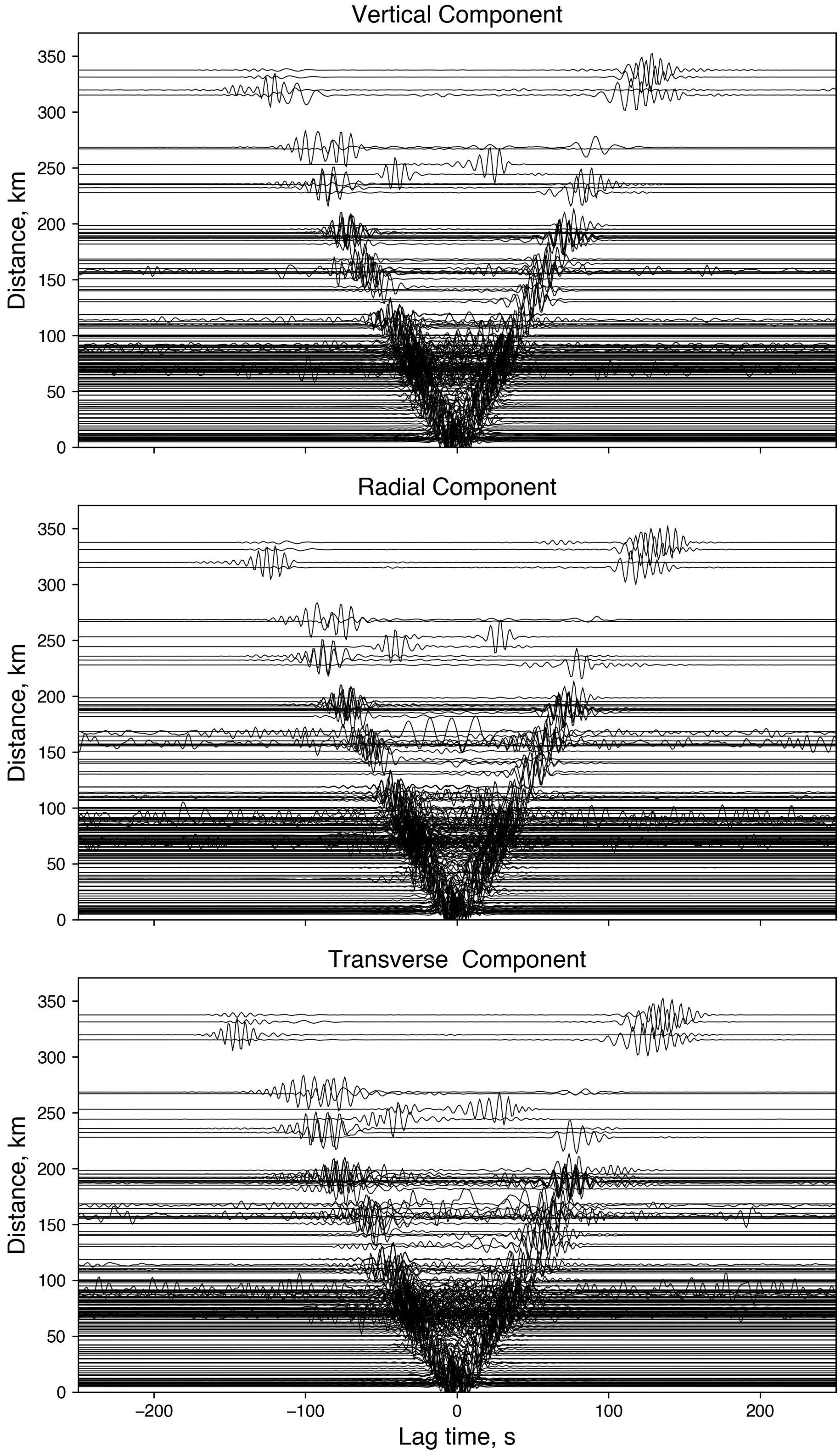

Fig. 5.4 Noise cross correlation functions extracted from the vertical, radial and transverse components for all station pairs that include K250. All plots display a typical move-out pattern associated with surface wave empirical Green's functions.

5.3.3 Automatic Measurements of Phase Velocities from EGFs

Phase velocities for Love and Rayleigh waves can be extracted from EGFs using the image-transformation technique described in Yao et al. (2006). Due to large size of the dataset ($\sim$7500 total EGFs), manual processing is not practical. We therefore develop a fully automated process for picking phase dispersion curves from EGFs based on the image-transformation technique. This process is divided into three separate steps:

- Converting the EGF into a velocity-period image
- Calculating a reference dispersion curve
- Using the reference curve to pick dispersion curves from the velocity-period images

The above steps are described in more detail below.

EGF to velocity-period image conversion

First, the EGF (Fig. 5.5a) is subjected to a series of narrow band passed filters at discrete central frequencies with 1 s intervals (Fig. 5.5b). We then convert the filtered EGF at each frequency from the time domain to the velocity domain (Fig. 5.5c) using the relationship:

$$c = \frac{r}{t - \frac{T}{8}} \tag{5.2}$$

where c is phase velocity, r is the station separation, t is travel time and T is the central period. This equation should not be confused with a similar equation developed by Brune et al. (1960) for extracting phase velocity which additionally includes a term for phase velocity ambiguity. In the equation of Brune et al. (1960), c and t represent exacts values, whereas in equation 2.5 they represent continuous domains, thus there is no notion of ambiguity. The ambiguity is of course still present and is accounted for later, as discussed below. Next, we re-sample the signal at 0.01 km/s increments. Finally, we vertically align all the processed signals in a matrix (Fig. 5.5d) such that the x axis represents the central period T, and the y axis represents velocity. Finally, we replace the line representation of the signal with a seismic colour map, giving the final velocity-period image (Fig. 5.5e). The velocity-period image usually displays several possible dispersion curves, seen has continuous high amplitude regions in red, representing the built-in ambiguity in picking phase velocity. To solve this ambiguity, we next calculate a reference curve which will be used in picking the correct dispersion curve.

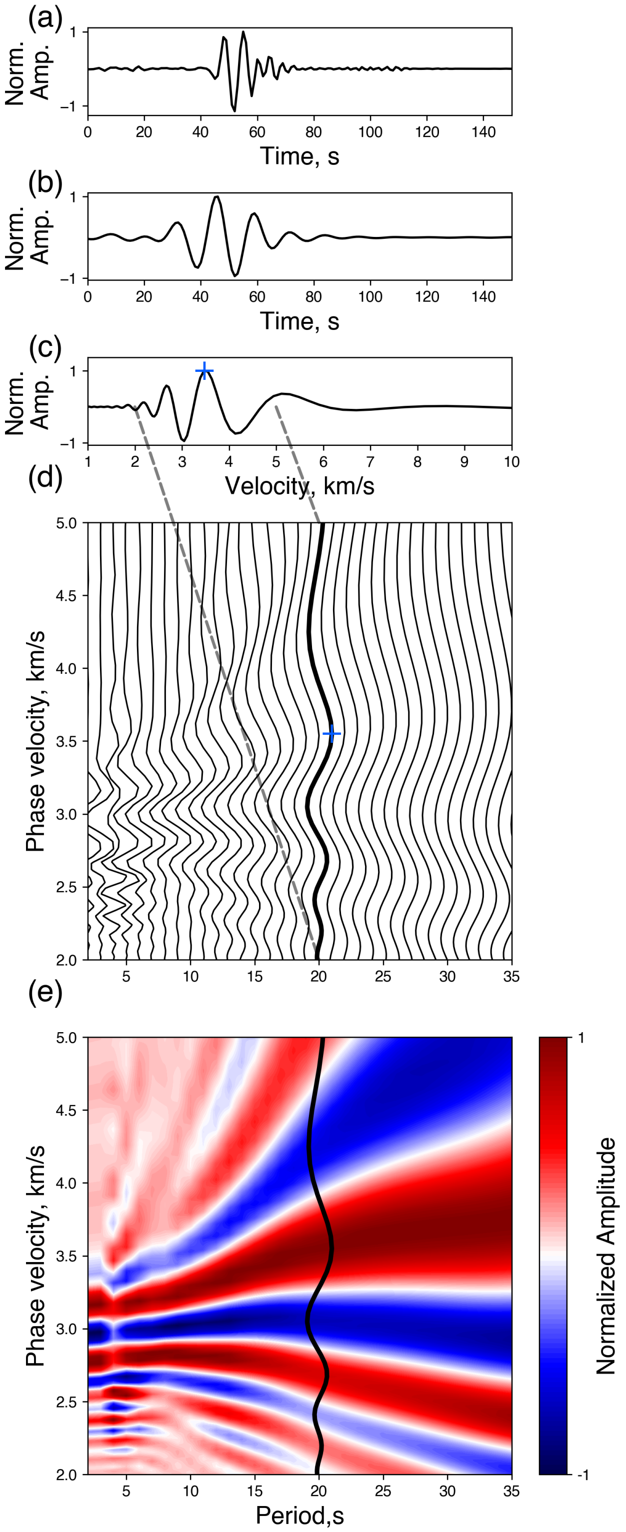

Fig. 5.5 EGF to velocity-period image conversion. **a** An EGF from stations SYLG and K250. **b** The same EGF filtered at a central period of 20 s. **c** The filtered EGF converted from the time domain to the velocity domain using $c = r/(t - T/8)$. **d** Filtered EGFs aligned vertically in a matrix with the positive side to the right. The 20 s filtered EGF from **c** is shown in bold. Dashed grey lines connect the locations of corresponding points from **c**. Blue crosses indicate the same point in **c** and **d**. **e** The line representation is replaced with a seismic colour map. The 20 s filtered EGF from **c** is shown in bold.

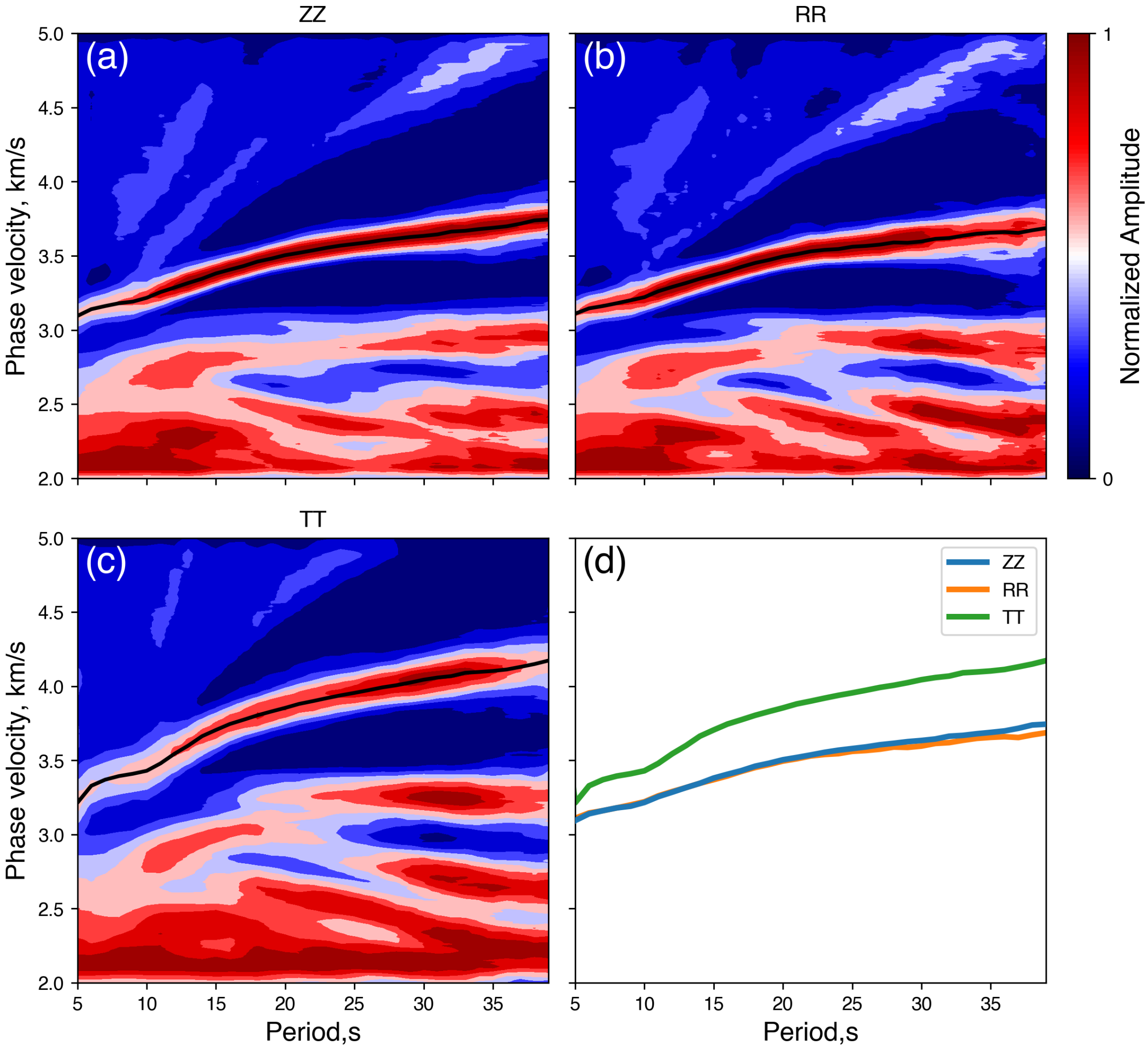

Fig. 5.6 Calculation of regional reference curves. The individual period-velocity images are summed up and the result displays one clear dispersion curve for each component. The results of this process are shown in panels **a**, **b** and **c** for the vertical, radial and transverse component respectively. **d** The calculated curves from **a**, **b** and **c** are plotted together for comparison

Reference dispersion curve

To automatically calculate a reference curve, we first take each period-velocity image and change any pixel which is a local maximum in the velocity domain (y direction) to a value of one and the rest to zero. Then, we sum all the converted images in the period-velocity domain and get a regional velocity-period image with one clear dispersion curve (Fig. 5.6). We repeat this for process for each of the components separately. It can be seen that the vertical and radial curves which represent Rayleigh wave velocities are highly similar (Fig. 5.6d). The fact that these two independently calculated regional dispersion curves for Rayleigh waves are so similar, indicate that this process is robust.

Picking dispersion curves

Next, from each velocity-period image, we wish to pick the dispersion curve that is closest to the reference curve. However, at different periods, different curves could be closer to the reference curve, making the selection non-trivial. Since the ambiguity is smallest at longer periods (least number of possible curves), we choose the curve that is closest to the reference curve at the longest period available, follow it towards shorter periods, and stop at either the minimum period, or when a sharp change is detected (Fig. 5.7). For example, in the case of the transverse component for the pair MJO - SNAE (Fig. 5.7 - bottom right panel), at short periods of 0 - 10 seconds the bottom curve is closeset to the refrence curve and at long periods of 15 - 30 seconds the top curve is closer. We therfore choose the upper curve. While this procedure requires the assumption of the far-field approximation which has traditionally limited similar studies to a station separation of 3 wavelengths, recent works (e.g. Luo et al., 2015) have shown that the measurements remain reliable at a station separation of two or possibly even one wavelength. In this work we limit the station separation to a minimum of two wavelengths. We only used dispersion curves that included at least 8 consecutive discreet periods. The final number of dispersion curves was 2193 and 1576 for Rayleigh and Love respectively.

5.3.4 2D Inversion of Phase velocities

We invert the phase velocities for 2D maps using FMST (Fast Marching Surface Tomography) (Rawlinson and Sambridge, 2005) which is an iterative non-linear travel time tomography solver in 2D spherical coordinates that is widely used for inverting surface waves data from ambient noise. We perform the inversion separately for Love and Rayleigh waves at each period from 4 to 16 seconds. The model spans 580 km in longitude (E-W), 440 km in latitude (N-S) and is parametrized using a velocity grid with 20 km spacing, similar to the

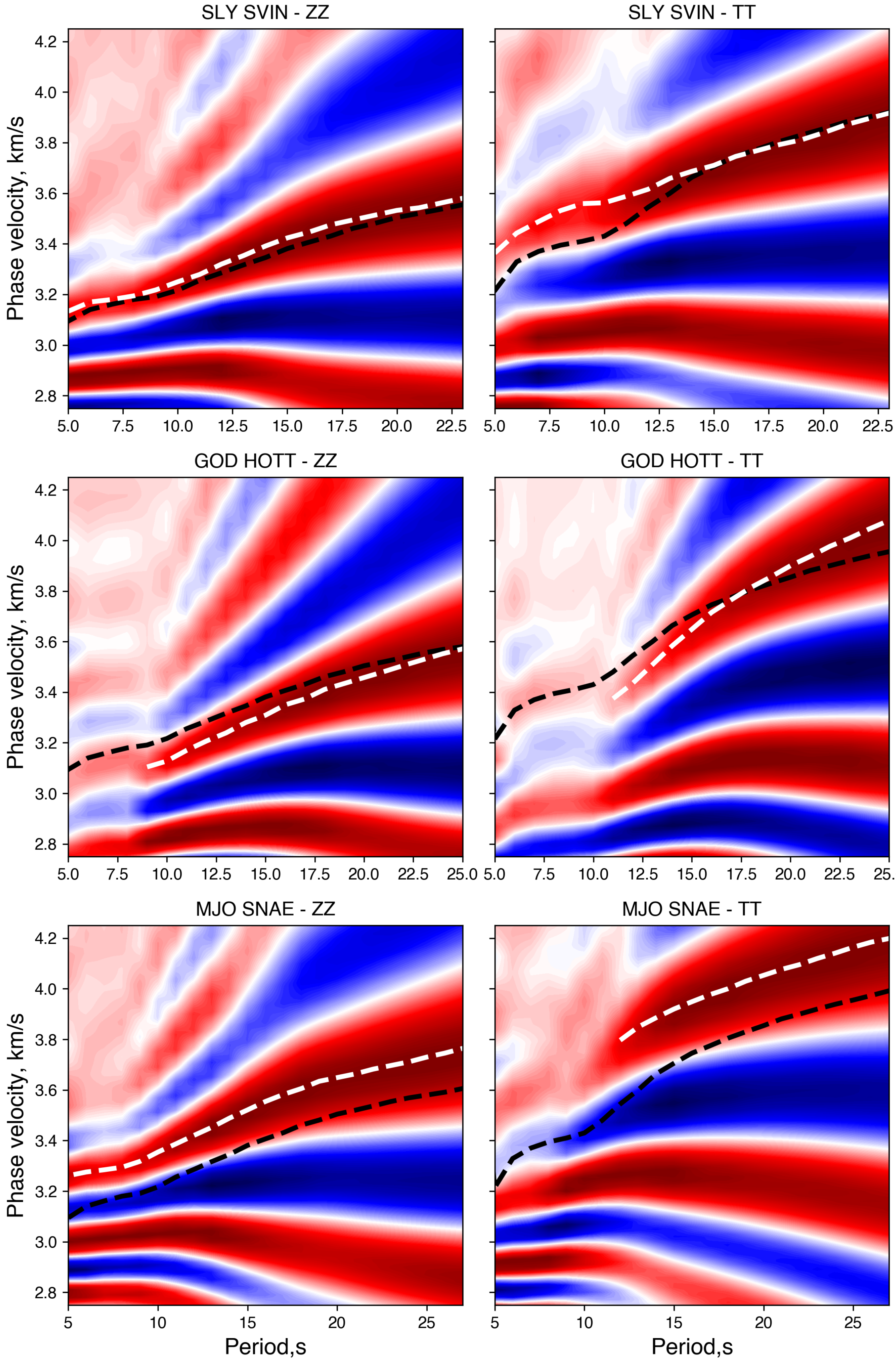

Fig. 5.7 Picking of phase dispersion curves. Examples of automatic dispersion curve picking for station pair SLY - SVIN (191 km apart), GOD - HOTT (204 km apart) and MJO - SNAE (220 km apart). Black dashed lines are calculated reference curves from Figure 5.6. White dashed lines are the picked dispersion curves.

average station spacing. FMST utilizes damping and smoothing regularisation to reduce non-uniqueness. Damping favours models with smaller perturbations to the starting model and smoothing favours models with lower roughness (i.e. a parsimonious final model). Damping and smoothing values are chosen using an L-curve (Fig. 5.8) to balance data fit with model smoothness and model perturbation. To create the L-curve we vary one of the parameters while keeping the other fixed at 0.1 (other values gave similar results).

Synthetic recovery tests were performed separately for Love and Rayleigh with a "checkers" size of 40 km (Fig. 5.9). Gaussian noise with standard deviation 1 s was added to the travel times to simulate the noise content of the observations. It can be seen that the fidelity of the recovery closely follows the network density with the best resolution in the east, where much of the Cambridge network is deployed. Additionally, we performed a recovery test using a realistic velocity structure (Fig. 5.10) based on the findings of previous imaging results and a geological map (Fig. 5.3f-g). It can be seen that with 0 - 1 s noise, the structure is well resolved. With 2 s noise, the structure is somewhat smeared.

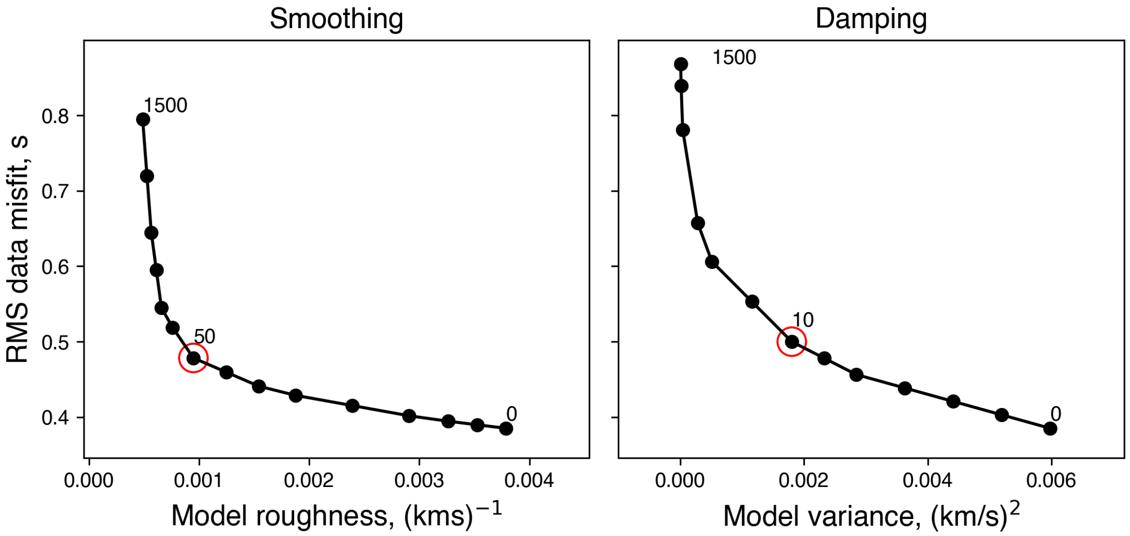

Fig. 5.8 An example of how smoothing and damping parameters are chosen using an L-curve for the inversion at 12 s.

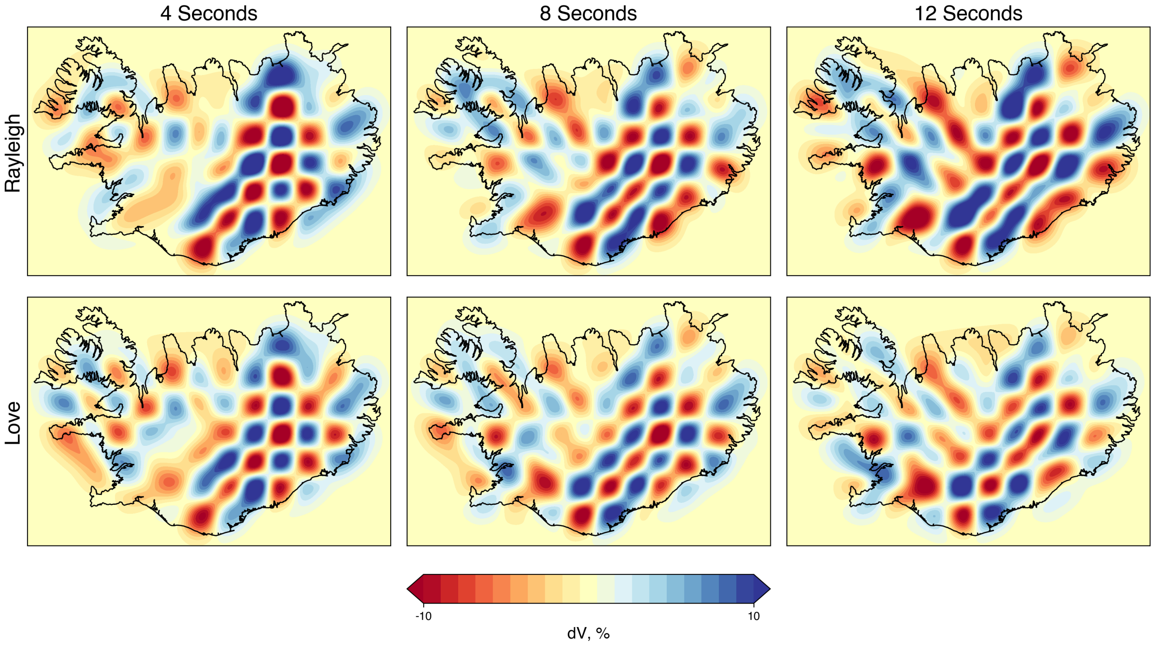

Fig. 5.9 Synthetic recovery tests for Love and Rayleigh waves with 40 km “checkers” at 4, 8 and 12 s periods.

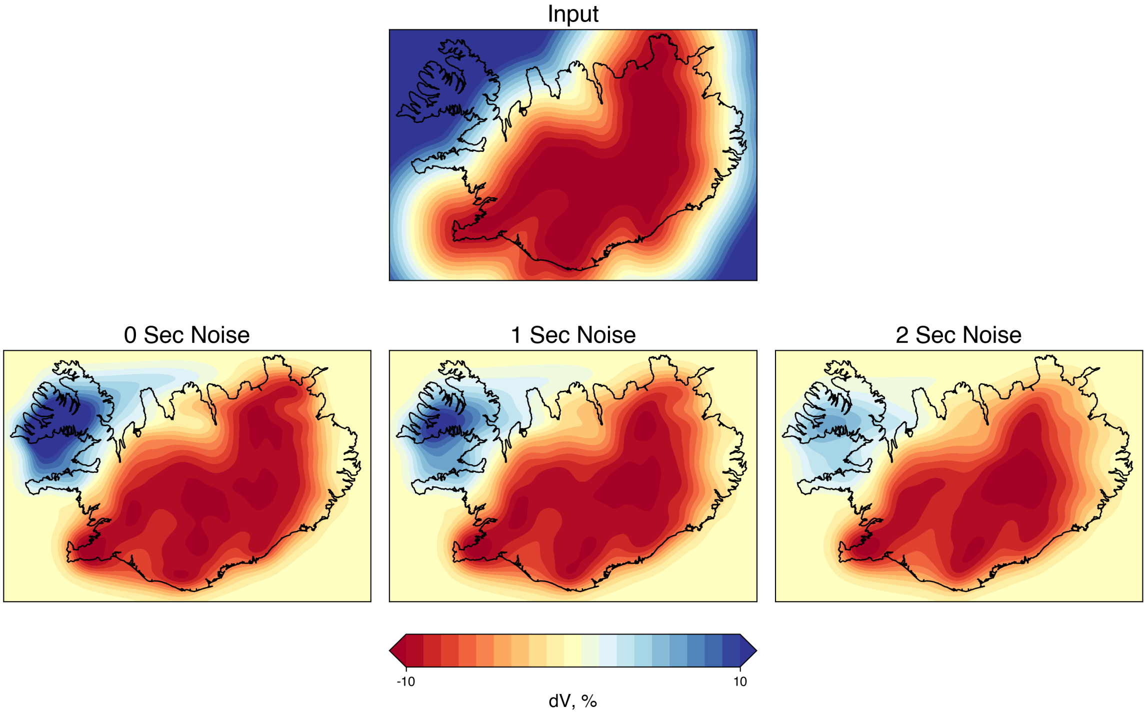

Fig. 5.10 Synthetic recovery test for an input velocity structure based on the results of previous studies using different noise levels.

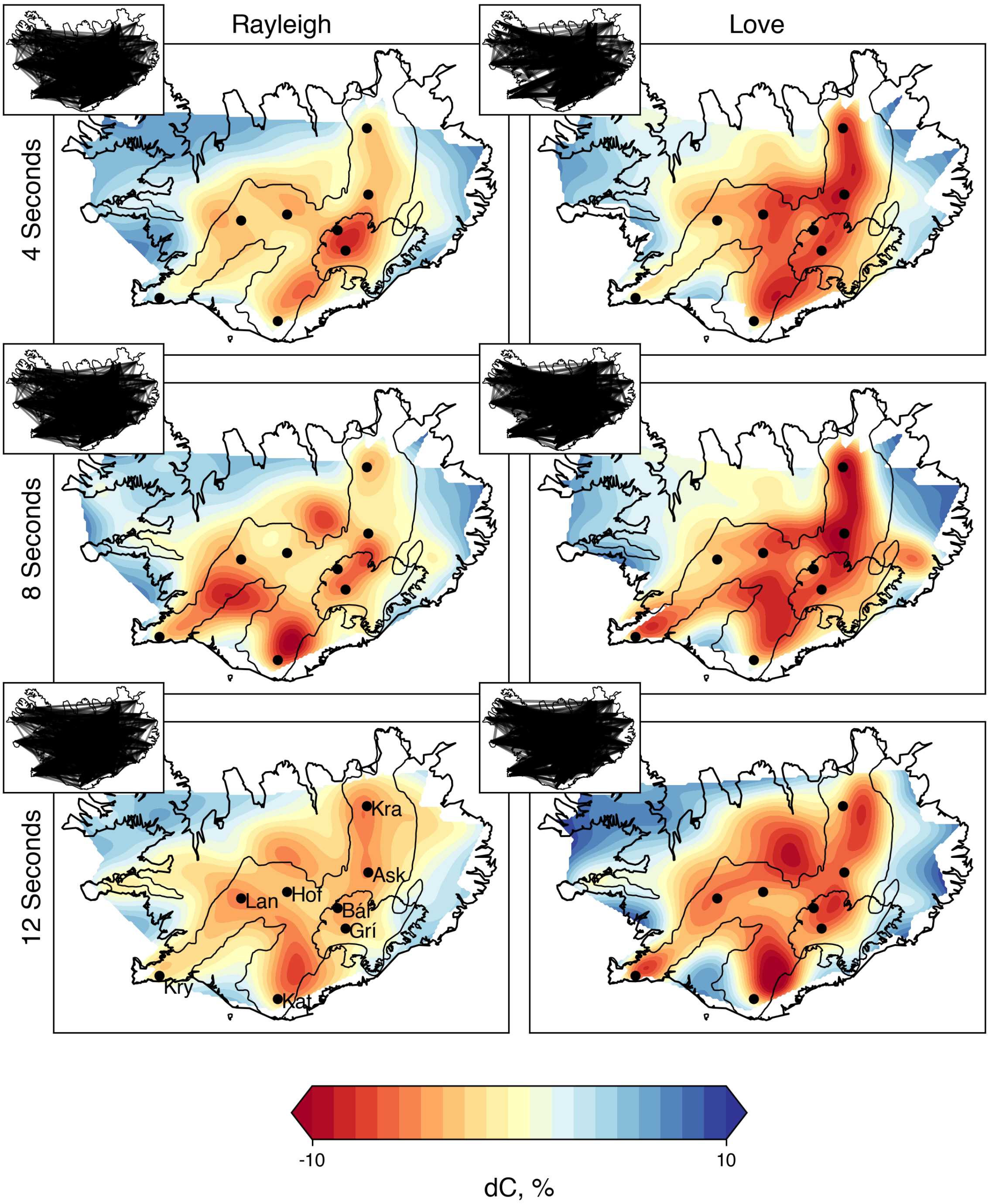

Fig. 5.11 Phase velocity maps of Iceland for Rayleigh and Love waves at periods of 4, 8 and 12 s. Black lines show the outline of outcropping rock younger than 0.7 Ma and the Vatnajökull icecap. The phase velocity maps are masked outside the region covered by the ray-paths. The inset maps show the ray-path coverage at each period. Black dots denote the location of large volcanic centres. Abbreviated names can be seen in the bottom left panel: Kra - Krafla, Kat - Katla, Ask - Askja, Bár - Bárðarbunga, Grí - Grímsvötn, Krý - Krýsuvík, Hof - Hofsjökull, Lan - Langjökull.

5.4 Results and Discussion

5.4.1 2D phase velocity maps

Phase velocity maps for 4, 8 and 12 s are presented in figure 5.11. While it is possible to extract pseudo dispersion curves from this model and invert them for V_{SV} and V_{SH} models as was done in chapter 4, the Love pseudo dispersion curves exhibit an unrealistic geometry, suggesting a more conservative approach of only presenting phase velocity maps. To first order, both Love and Rayleigh phase velocity maps display slow anomalies along the rift zones, and faster velocities elsewhere. This agrees well with previous studies (e.g. Green et al., 2017; Allen et al., 2002). Since the upper crust in Iceland is relatively compositionally homogeneous (mostly basalt), lateral velocity variations most likely reflect changes in temperature, partial melt content or levels of porosity. Green et al. (2017) has interpreted the lateral velocity gradient as the result of an ageing effect, whereby the high porosity of young rifted crust is reduced with time through mineralisation in pore spaces. Allen et al. (2002) has suggested that the lower velocities in the rifts are associated with higher temperatures. To try and distinguish between these two causes, we can look at the differences between Love and Rayleigh phase velocities. As we can see, the velocity gradients we observe between the rifts and the outer regions, are stronger (darker colours) in the Love phase velocity maps than in the Rayleigh phase velocity maps. This could be interpreted as supporting the crack density explanation suggested by Green et al. (2017) since unlike temperature, the existence of sub-vertical cracks (as expected in a rift zone) will decrease Love velocities more significantly than Rayleigh velocities (Ding et al., 2017).

5.4.2 Low velocities and volcanic centres

Near active volcanic centres, it is likely that the presence of partial melt acts to reduce shear velocity. Caricchi et al. (2008) suggested that to reduce the shear velocity by 0.1 km/s, as little as 1% partial melt is required. Within the rift zones, both Love and Rayleigh phase velocity maps display several distinct regions where velocity is reduced further and which coincide with location of known volcanic centres. In the northern most part of the NVZ, one such region can be seen near the location of Krafla, where partial melt has been constrained before at depths of 2 -3 km (Einarsson, 1978; Schuler et al., 2015; Brandsdóttir and Menke, 1992). Another such slow anomaly can be seen beneath the northern part of Vatnajökull icecap, associated with Bárðarbunga and Grímsvötn where partial melt has been imaged at depths of 3 – 4 km (Alfaro et al., 2007). Similarly, another slow anomaly is adjacent to Katla where partial melt has been constrained at depths of 3 - 4 km (Gudmundsson et al., 1994). The region around Askja, where partial melt has also been imaged (Greenfield et al., 2016), does not show such a large slow anomaly. However, Askja is very close (30 km) to Bárðarbunga and Grímsvötn and our model is unlikely to image it as a separate anomaly. We see another such anomaly near Krýsuvík in the 8 and 12 s Love velocity maps, where melt has been suggested (Lu, 2014) but has not previously been decisively imaged. Additionally, in the 4 s Rayleigh wave map, we see weaker slow anomalies near Hofsjökull and Langjökull where shallow melt regions have not peviously been imaged. Overall, our findings agree with Green et al. (2017) which showed that Rayleigh wave velocities were slower around large volcanic centres and we further show that Love wave velocities are similarly affected as well.

5.5 Conclusion

We have presented the first ambient noise derived phase velocity maps in Iceland for both Love and Rayleigh waves by exploiting long-term recordings from 189 stations deployed as part of five separate networks. Reliable phase velocity maps between 4 s and 12 s period were obtained for both data types, which correspond to mid-upper crustal depths.Rayleigh phase velocity maps were found to be similar to group velocity maps with low velocities along the rift zones and very low velocities near large volcanic systems, which is consistent with the presence of partial melt resulting from the combined effects of decompression melting caused by ascending plume material and plate spreading associated with the Mid-Atlantic Ridge. Love phase velocities are shown to follow a similar pattern but display a larger velocity difference between the rift zones and the outer region, reinforcing the suggestion that crustal weathering with age s a major factor in controlling the upper crustal velocity structure. The new results also reveal low velocities in regions where melt has not previously been detected, such as in the 8 and 12 s Love velocity maps near Krysuvik on the Reykjanes Peninsual near Reykjavik. Although not well resolved in our images, further investigation of these anomalies appears warranted.

Chapter 6

Conclusions and future directions

In this thesis, I have presented several different uses of ambient seismic noise to investigate the crust in Iceland. Personally, what I found most exciting about working with ambient noise is the relative ease in which one can obtain a dataset of surface wave dispersion with very dense azimuthal coverage. Isotropic seismic tomography gives us a “static” image of Earth’s velocity structure, while seismic anisotropy is a powerful tool for completing that image by allowing us to infer more dynamic processes. In Iceland specifically, the high level of seismic noise, and the relatively homogeneous crustal composition, create an ideal setting for investigating azimuthal and radial anisotropy. The dense azimuthal coverage of surface wave velocities extracted from ambient noise has given us high-resolution constraints on seismic anisotropy in the Icelandic crust, which is closely related to its tectonic setting.

In chapter 3, we have seen that in the brittle crust, cracks and dykes striking perpendicular to the extension direction result in negative radial anisotropy with an extension perpendicular fast direction. In the lower crust, our dataset has allowed us to observe LPO in oceanic crust for the first time, as positive radial anisotropy with significant variations between spreading perpendicular and spreading parallel ray-paths. Moreover, since LPO requires internal shear, this observation provides new constraints on the style of crustal accretion and deformation at plume-ridge interactions. Similar observation have previously only been made in continental crust (e.g. Shapiro and Campillo, 2004; Duret et al., 2010) where Love and Rayleigh wave velocities in the lower crust could not be reconciled using an isotropic model. The anisotropy there was attributed to LPO in micas related to crustal thinning. Further interpretation of our result to decisively include a mechanism for driving flow and a flow direction depends on further research into the composition of the lower crust as well as knowledge on gabbro deformation.

In chapter 4, I presented a unique comparison between local shear wave splitting, outcrop mapping and surface wave anisotropy. Comparisons between Rayleigh wave anisotropy and shear wave splitting has been done on regional and global scales (Wüstefeld et al., 2009; Montagner and Nataf, 1986), but to the best of my knowledge has not been demonstrated in shallow heterogeneous crust. This comparison has shown us just how useful the surface waves can be for estimating crack properties. Unlike shear wave splitting, which requires local seismicity, and outcrop mapping, which is time consuming and can only be done where the terrain allows, ambient noise analysis can be easily carried out almost anywhere on the planet. Similarly with the results from the upper crust in chapter 3, the fast direction here is found to be perpendicular to the extension direction. Moreover, in chapter 4, I compared the 1D average shear velocity models derived from surface waves to the one derived from body waves and showed that due to the presence of cracks, V_{SV} models derived from Rayleigh waves can be significantly faster than body wave derived S-models which are mostly sensitive to V_{SH}. This is important since V_{SV} models derived from Rayleigh waves have been used to locate earthquakes (e.g. Johnson et al., 2010; Jolly et al., 2017) at various volcanoes worldwide and may lead to systemic errors in depth location. I suggest that this could be mitigated by using V_{SH} models from Love waves or using estimates of crack density. Also in chapter 4, ambient noise tomography has revealed a slow shallow anomaly which most likely corresponds to a shallow melt storage region predicted by InSAR. As body wave tomography could not resolve this anomaly, this demonstrates again how ambient noise is able to achieve observations not previously possible and complement body wave observations. An interesting future direction could be to perform a joint inversion of some or all of the datasets available in Askja. Each of the datasets in this work and in previous studies (InSAR, delay times, Rayleigh dispersion, Love dispersion, body wave picks) has been inverted separately. Finding a holistic model of Askja which could satisfy most/all types of data would probably give us a fuller understanding of the Aksja region.

In chapter 5, I developed an automated method for picking phase dispersion curves and used it to pick more than 3500 dispersion curves of both Love and Rayleigh waves. I showed that to first order, both Love and Rayleigh velocities in the upper crust are dominated by cracks, which is consistent with the observations of anisotropy in the upper crust in chapters 3 and 4. I additionally showed that both Love and Rayleigh velocities display very slow velocities near large volcanic centres, demonstrating the importance of partial melt in controlling shear velocities in Iceland.

One thing that has historically limited deep seismic imaging in Iceland, which also applies to the work presented in Chapters 3 and 5, is its relatively small geographical extent. With several types of seismic imaging such as ambient noise analysis, the recovered depth is limited by the lateral size of the network coverage (Bensen et al., 2007). In teleseismic body wave tomography, a small network footprint reduces vertical resolution, limiting our ability to image the mantle plume beneath Iceland in greater detail (Keller et al., 2000; Wolfe, 2002). I therefore believe that deploying ocean bottom seismometers around Iceland would lead to a better understanding of the plume source. From a surface wave analysis perspective, this would allow us to explore seismic anisotropy in the mantle with dense azimuthal coverage using both ambient noise and teleseismic waves.

To conclude, I have presented several new observations regarding the seismic anisotropy and velocity structure of the Icelandic crust by extracting and analysing surface wave dispersion data from ambient noise. Iceland is a unique place which has historically provided new and exciting observations and has helped further our understanding of plate tectonics and, as we have seen here, continues to do so. All of this would not have been possible without the work of many researchers who have collected and archived seismic data in Iceland for decades and I feel honoured and fortunate to have taken a part in this process.

References

Aki, K. (1957). Space and time spectra of stationary stochastic waves, with special reference to microtremors. *Bulletin of the Earthquake Research Institute*, 35:415–456.

Alfaro, R., Brandsdóttir, B., Rowlands, D. P., White, R. S., and Gudmundsson, M. T. (2007). Structure of the grímsvötn central volcano under the vatnajökull icecap, iceland. *Geophysical Journal International*, 168(2):863–876.

Allen, R. M., Nolet, G., Morgan, W. J., Vogfjörd, K., Bergsson, B. H., Erlendsson, P., Foulger, G., Jakobsdóttir, S., Julian, B. R., Pritchard, M., et al. (1999). The thin hot plume beneath iceland. *Geophysical Journal International*, 137(1):51–63.

Allen, R. M., Nolet, G., Morgan, W. J., Vogfjörd, K., Nettles, M., Ekström, G., Bergsson, B. H., Erlendsson, P., Foulger, G. R., Jakobsdóttir, S., Julian, B. R., Pritchard, M., Ragnarsson, S., and Stefánsson, R. (2002). Plume-driven plumbing and crustal formation in Iceland. *Journal of Geophysical Research*, 107(B8):2163.

Anderson, D. L. (1965). Recent evidence concerning the structure and composition of the earth's mantle. *Physics and Chemistry of the Earth*, 6:1–131.

Backus, G. E. (1962). Long-wave elastic anisotropy produced by horizontal layering. *Journal of Geophysical Research*, 67(11):4427–4440.

Bacon, C., White, R., and Rawlinson, N. (2019). Depth Constraints on Seismic Anisotropy in Iceland from Shear Wave Splitting Measurements. In *AGU Fall Meeting*, number S41D–0559, San Francisco.

Barclay, A. H. and Toomey, D. R. (2003). Shear wave splitting and crustal anisotropy at the mid-atlantic ridge, 35° n. *Journal of Geophysical Research: Solid Earth*, 108(B8).

Bastow, I. D., Pilidou, S., Kendall, J.-M., and Stuart, G. W. (2010). Melt-induced seismic anisotropy and magma assisted rifting in Ethiopia: Evidence from surface waves. *Geochemistry, Geophysics, Geosystems*, 11(6).

Bensen, G. D., Ritzwoller, M. H., Barmin, M. P., Levshin, A. L., Lin, F., Moschetti, M. P., Shapiro, N. M., and Yang, Y. (2007). Processing seismic ambient noise data to obtain reliable broad-band surface wave dispersion measurements. *Geophysical Journal International*, 169(3):1239–1260.

Bhattacharya, S. N. (2015). Sensitivities of surface wave velocities to the medium parameters in a radially anisotropic spherical Earth and inversion strategies. *Annals of Geophysics*, 58(5):0545.

Bijwaard, H. and Spakman, W. (1999). Tomographic evidence for a narrow whole mantle plume below Iceland. *Earth and Planetary Science Letters*, 166(3-4):121–126.

Bjarnason, I. T. and Schmeling, H. (2009). The lithosphere and asthenosphere of the Iceland hotspot from surface waves. *Geophysical Journal International*, 178(1):394–418.

Bjarnason, I. T., Silver, P. G., Rümpker, G., and Solomon, S. C. (2002). Shear wave splitting across the Iceland hot spot: Results from the ICEMELT experiment. *Journal of Geophysical Research: Solid Earth*, 107(B12):ESE 23–1–ESE 23–12.

Blackman, D. K. and Kendall, J.-M. (2002). Seismic anisotropy in the upper mantle 2. Predictions for current plate boundary flow models. *Geochemistry, Geophysics, Geosystems*, 3(9):1–24.

Blackman, D. K., Wenk, H.-R., and Kendall, J. M. (2002). Seismic anisotropy of the upper mantle 1. Factors that affect mineral texture and effective elastic properties. *Geochemistry, Geophysics, Geosystems*, 3(9):1–24.

Bodin, T., Sambridge, M., Tkalčić, H., Arroucau, P., Gallagher, K., and Rawlinson, N. (2012). Transdimensional inversion of receiver functions and surface wave dispersion. *Journal of Geophysical Research: Solid Earth*, 117(B2).

Boschi, L., Weemstra, C., Verbeke, J., Ekström, G., Zunino, A., and Giardini, D. (2013). On measuring surface wave phase velocity from station-station cross-correlation of ambient signal. *Geophysical Journal International*, 192(1):346–358.

Brandsdóttir, B., Menke, W., Einarsson, P., White, R. S., and Staples, R. K. (1997). Färoe-Iceland Ridge Experiment 2. Crustal structure of the Krafla central volcano. *Journal of Geophysical Research: Solid Earth*, 102(B4):7867–7886.

Brandsdóttir, B. and Menke, W. H. (1992). Thin low-velocity zone within the krafla caldera, ne-Iceland attributed to a small magma chamber. *Geophysical Research Letters*, 19(24):2381–2384.

Brenguier, F., Shapiro, N. M., Campillo, M., Nercessian, A., and Ferrazzini, V. (2007). 3-D surface wave tomography of the Piton de la Fournaise volcano using seismic noise correlations. *Geophysical Research Letters*, 34(2):L02305.

Brune, J. N., Nafe, J. E., and Oliver, J. E. (1960). A simplified method for the analysis and synthesis of dispersed wave trains. *Journal of Geophysical Research*, 65(1):287–303.

Caricchi, L., Burlini, L., and Ulmer, P. (2008). Propagation of P and S-waves in magmas with different crystal contents: Insights into the crystallinity of magmatic reservoirs. *Journal of Volcanology and Geothermal Research*, 178(4):740–750.

Chang, S.-J., Van Der Lee, S., Matzel, E., and Bedle, H. (2010). Radial anisotropy along the tethyan margin. *Geophysical Journal International*, 182(2):1013–1024.

Chen, M., Huang, H., Yao, H., van der Hilst, R., and Niu, F. (2014). Low wave speed zones in the crust beneath se tibet revealed by ambient noise adjoint tomography. *Geophysical Research Letters*, 41(2):334–340.

Crampin, S. and Taylor, D. B. (1971). The Propagation of Surface Waves in Anisotropic Media. *Geophysical Journal of the Royal Astronomical Society*, 25(1-3):71–87.

Darbyshire, F. A., Bjarnason, I. T., White, R. S., and Flóvenz, Ó. G. (1998). Crustal structure above the Iceland mantle plume imaged by the ICEMELT refraction profile. *Geophysical Journal International*, 135(3):1131–1149.

Darbyshire, F. A., White, R. S., and Priestley, K. F. (2000). Structure of the crust and uppermost mantle of Iceland from a combined seismic and gravity study. *Earth and Planetary Science Letters*, 181(3):409–428.

De Siena, L., Sammarco, C., Cornwell, D. G., La Rocca, M., Bianco, F., Zaccarelli, L., and Nakahara, H. (2018). Ambient Seismic Noise Image of the Structurally Controlled Heat and Fluid Feeder Pathway at Campi Flegrei Caldera. *Geophysical Research Letters*, 45(13):6428–6436.

De Zeeuw-van Dalfsen, E., Pedersen, R., Hooper, A., and Sigmundsson, F. (2012). Subsidence of Askja caldera 2000-2009: Modelling of deformation processes at an extensional plate boundary, constrained by time series InSAR analysis. *Journal of Volcanology and Geothermal Research*, 213:72–82.

Debayle, E., Kennett, B., and Priestley, K. (2005). Global azimuthal seismic anisotropy and the unique plate-motion deformation of Australia. *Nature*, 433(7025):509–512.

DeMets, C., Gordon, R. G., and Argus, D. F. (2010). Geologically current plate motions. *Geophysical Journal International*, 181(1):1–80.

Derode, A., Larose, E., Tanter, M., de Rosny, J., Tourin, A., Campillo, M., and Fink, M. (2003). Recovering the Green's function from field-field correlations in an open scattering medium (L). *The Journal of the Acoustical Society of America*, 113(6):2973–2976.

Ding, P., Di, B., Wang, D., Wei, J., and Li, X. (2017). Measurements of Seismic Anisotropy in Synthetic Rocks with Controlled Crack Geometry and Different Crack Densities. *Pure and Applied Geophysics*, 174(5):1907–1922.

Donaldson, C. G. (2019). *Towards monitoring volcanoes in Iceland and Hawai'i with seismic velocity variations*. PhD thesis, University of Cambridge.

Dreiling, J., Tilmann, F., Yuan, X., Giese, J., Rindraharisaona, E. J., Rümpker, G., and Wysession, M. E. (2018). Crustal Radial Anisotropy and Linkage to Geodynamic Processes: A Study Based on Seismic Ambient Noise in Southern Madagascar. *Journal of Geophysical Research: Solid Earth*, 123(6):5130–5146.

Duennebier, F. K. and Sutton, G. H. (1995). Fidelity of ocean bottom seismic observations. *Marine Geophysical Researches*, 17(6):535–555.

Dunn, R. A. and Toomey, D. R. (2001). Crack-induced seismic anisotropy in the oceanic crust across the East Pacific Rise (9°30'N). *Earth and Planetary Science Letters*, 189(1-2):9–17.

Duret, F., Shapiro, N. M., Cao, Z., Levin, V., Molnar, P., and Roecker, S. (2010). Surface wave dispersion across Tibet: Direct evidence for radial anisotropy in the crust. *Geophysical Research Letters*, 37(16).

Dziewonski, A., Bloch, S., and Landisman, M. (1969). A technique for the analysis of transient seismic signals. *Bulletin of the Seismological Society of America*, 59(1):427–444.

Dziewonski, A. M. and Anderson, D. L. (1981). Preliminary reference Earth model. *Physics of the Earth and Planetary Interiors*, 25(4):297–356.

Einarsson, P. (1978). S-wave shadows in the Krafla Caldera in NE-Iceland, evidence for a magma chamber in the crust. *Bulletin Volcanologique*, 41(3):187–195.

Ekström, G., Abers, G. A., and Webb, S. C. (2009). Determination of surface-wave phase velocities across USArray from noise and Aki's spectral formulation. *Geophysical Research Letters*, 36(18).

Fang, H., Yao, H., Zhang, H., Huang, Y. C., and Van Der Hilst, R. D. (2015). Direct inversion of surface wave dispersion for three-dimensional shallow crustal structure based on ray tracing: Methodology and application. *Geophysical Journal International*, 201(3):1251–1263.

Fichtner, A. (2014). Source and processing effects on noise correlations. *Geophysical Journal International*, 197(3):1527–1531.

Fichtner, A., Bowden, D., and Ermert, L. (2020). Optimal processing for seismic noise correlations. *Geophysical Journal International*, 223(3):1548–1564.

Fishwick, S., Kennett, B. L., and Reading, A. M. (2005). Contrasts in lithospheric structure within the Australian craton - Insights from surface wave tomography. *Earth and Planetary Science Letters*, 231(3-4):163–176.

Flóvenz, Ó. G. and Saemundsson, K. (1993). Heat flow and geothermal processes in Iceland. *Tectonophysics*, 225(1-2):123–138.

Font, Y., Kao, H., Lallemand, S., Liu, C. S., and Chiao, L. Y. (2004). Hypocentre determination offshore of eastern Taiwan using the maximum intersection method. *Geophysical Journal International*, 158(2):655–675.

Foulger, G. R., Pritchard, M. J., Julian, B. R., Evans, J. R., Allen, R. M., Nolet, G., Morgan, W. J., Bergsson, B. H., Erlendsson, P., Jakobsdottir, S., Ragnarsson, S., Stefansson, R., and Vogfjörd, K. (2001). Seismic tomography shows that upwelling beneath Iceland is confined to the upper mantle. *Geophysical Journal International*, 146(2):504–530.

Franzson, H. E. A. (2001). Petrophysical properties of icelandic rocks. In *Proceedings of the 6th Nordic Symposium on Petrophysics, Tronheim, Norway. In: Knut Backe & Ton Loermans (ed), The Norwegian University of Science and Technology. Trondheim, Norway.*

French, S. W. and Romanowicz, B. (2015). Broad plumes rooted at the base of the Earth's mantle beneath major hotspots. *Nature*, 525(7567):95–99.

Geoffroy, L. (2005). Volcanic passive margins. *Comptes Rendus Geoscience*, 337(16):1395–1408.

Green, R. (2016). *The structure and seismicity of Icelandic rifts*. PhD thesis, University of Cambridge.

Green, R. G., Priestley, K. F., and White, R. S. (2017). Ambient noise tomography reveals upper crustal structure of Icelandic rifts. *Earth and Planetary Science Letters*, 466:20–31.

Greenfield, T., White, R. S., and Roecker, S. (2016). The magmatic plumbing system of the Askja central volcano, Iceland, as imaged by seismic tomography. *Journal of Geophysical Research: Solid Earth*, 121(10):7211–7229.

Greenfield, T., White, R. S., Winder, T., and Ágústsdóttir, T. (2020). Seismicity of the Askja and Bárðarbunga volcanic systems of Iceland, 2009–2015. *Journal of Volcanology and Geothermal Research*, 391:106432.

Gudmundsson, Ó. (2003). The dense root of the Iceland crust. *Earth and Planetary Science Letters*, 206(3-4):427–440.

Gudmundsson, O., Brandsdottir, B., Menke, W., and Sigvaldason, G. E. (1994). The crustal magma chamber of the Katla volcano in south Iceland revealed by 2-D seismic undershooting. *Geophysical Journal International*, 119(1):277–296.

Guo, Z., Gao, X., Wang, W., and Yao, Z. (2012). Upper-and mid-crustal radial anisotropy beneath the central himalaya and southern tibet from seismic ambient noise tomography. *Geophysical Journal International*, 189(2):1169–1182.

Hardarson, B. S., Fitton, J. G., Ellam, R. M., and Pringle, M. S. (1997). Rift relocation - A geochemical and geochronological investigation of a palaeo-rift in northwest Iceland. *Earth and Planetary Science Letters*, 153(3-4):181–196.

Helmberger, D. V., Wen, L., and Ding, X. (1998). Seismic evidence that the source of the Iceland hotspot lies at the core-mantle boundary. *Nature*, 396(6708):251–255.

Herrmann, R. B. (2013). Computer Programs in Seismology: An Evolving Tool for Instruction and Research. *Seismological Research Letters*, 84(6):1081–1088.

Hess, H. (1964). Seismic anisotropy of the uppermost mantle under oceans. *Nature*, 203(4945):629–631.

Hillers, G. and Ben-Zion, Y. (2011). Seasonal variations of observed noise amplitudes at 2-18 Hz in southern California. *Geophysical Journal International*, 184(2):860–868.

Hjartardóttir, Á. R., Einarsson, P., and Björgvinsdóttir, S. G. (2016). Fissure swarms and fracture systems within the Western Volcanic Zone, Iceland – Effects of spreading rates. *Journal of Structural Geology*, 91:39–53.

Hjartardóttir, Á. R., Einarsson, P., and Sigurdsson, H. (2009). The fissure swarm of the Askja volcanic system along the divergent plate boundary of N Iceland. *Bulletin of Volcanology*, 71(9):961–975.

Hudson, J. A. (1981). Wave speeds and attenuation of elastic waves in material containing cracks. *Geophysical Journal International*, 64(1):133–150.

Ismaïl, W. B. and Mainprice, D. (1998). An olivine fabric database: An overview of upper mantle fabrics and seismic anisotropy. *Tectonophysics*, 296(1-2):145–157.

Jaxybulatov, K., Shapiro, N. M., Koulakov, I., Mordret, A., Landès, M., and Sens-Schönfelder, C. (2014). A large magmatic sill complex beneath the Toba caldera. *Science*, 346(6209):617–619.

Jenkins, J., Cottaar, S., White, R., and Deuss, A. (2016). Depressed mantle discontinuities beneath Iceland: Evidence of a garnet controlled 660 km discontinuity? *Earth and Planetary Science Letters*, 433:159–168.

Jenkins, J., Maclennan, J., Green, R. G., Cottaar, S., Deuss, A. F., and White, R. S. (2018). Crustal Formation on a Spreading Ridge Above a Mantle Plume: Receiver Function Imaging of the Icelandic Crust. *Journal of Geophysical Research: Solid Earth*, 123(6):5190–5208.

Johnson, J. H., Prejean, S., Savage, M. K., and Townend, J. (2010). Anisotropy, repeating earthquakes, and seismicity associated with the 2008 eruption of Okmok volcano, Alaska. *Journal of Geophysical Research: Solid Earth*, 115(B9).

Jolly, A. D., Lokmer, I., Thun, J., Salichon, J., Fry, B., and Chardot, L. (2017). Insights into fluid transport mechanisms at White Island from analysis of coupled very long-period (VLP), long-period (LP) and high-frequency (HF) earthquakes. *Journal of Volcanology and Geothermal Research*, 343:75–94.

Jones, S. M. and Maclennan, J. (2005). Crustal flow beneath Iceland. *Journal of Geophysical Research: Solid Earth*, 110(B9).

Jousselin, D., Morales, L. F., Nicolle, M., and Stephant, A. (2012). Gabbro layering induced by simple shear in the Oman ophiolite Moho transition zone. *Earth and Planetary Science Letters*, 331-332:55–66.

Keller, W. R., Anderson, D. L., and Clayton, R. W. (2000). Resolution of tomographic models of the mantle beneath Iceland. *Geophysical Research Letters*, 27(24):3993–3996.

Korenaga, J. and Kelemen, P. B. (1998). Melt migration through the oceanic lower crust: A constraint from melt percolation modeling with finite solid diffusion. *Earth and Planetary Science Letters*, 156(1-2):1–11.

Lecocq, T., Caudron, C., and Brenguier, F. (2014). MSNoise, a Python Package for Monitoring Seismic Velocity Changes Using Ambient Seismic Noise. *Seismological Research Letters*, 85(3):715–726.

Lesage, P., Heap, M. J., and Kushnir, A. (2018). A generic model for the shallow velocity structure of volcanoes. *Journal of Volcanology and Geothermal Research*, 356:114–126.

Levshin, A. L. and Ritzwoller, M. H. (2001). Automated Detection, Extraction, and Measurement of Regional Surface Waves. In *Monitoring the Comprehensive Nuclear-Test-Ban Treaty: Surface Waves*, pages 1531–1545. Birkhäuser Basel, Basel.

Li, A. and Detrick, R. S. (2003). Azimuthal anisotropy and phase velocity beneath Iceland: implication for plume–ridge interaction. *Earth and Planetary Science Letters*, 214(1-2):153–165.

Lin, F. C., Moschetti, M. P., and Ritzwoller, M. H. (2008). Surface wave tomography of the western United States from ambient seismic noise: Rayleigh and Love wave phase velocity maps. *Geophysical Journal International*, 173(1):281–298.

Lin, P. Y. P., Gaherty, J. B., Jin, G., Collins, J. A., Lizarralde, D., Evans, R. L., and Hirth, G. (2016). High-resolution seismic constraints on flow dynamics in the oceanic asthenosphere. *Nature*, 535(7613):538–541.

Liu, Y., Niu, F., Chen, M., and Yang, W. (2017). 3-d crustal and uppermost mantle structure beneath ne china revealed by ambient noise adjoint tomography. *Earth and Planetary Science Letters*, 461:20–29.

Lobkis, O. I. and Weaver, R. L. (2001). On the emergence of the Green's function in the correlations of a diffuse field. *The Journal of the Acoustical Society of America*, 110(6):3011–3017.

Lomax, A., Michelini, A., and Curtis, A. (2014). Earthquake Location, Direct, Global-Search Methods. In *Encyclopedia of Complexity and Systems Science*, volume 5. Springer, New York, New York.

Long, M. D. and Becker, T. W. (2010). Mantle dynamics and seismic anisotropy. *Earth and Planetary Science Letters*, 297:341–354.

Love, A. (1892). *A treatise on the mathematical theory of elasticity*. Cambridge Universityy Press, Cambeidge.

Lu, J. (2014). *Seismic tomography and surface deformation in Krýsuvík, SW Iceland*. PhD thesis, Massachusetts Institute of Technology.

Lu, Y., Stehly, L., Brossier, R., Paul, A., and Group, A. W. (2020). Imaging alpine crust using ambient noise wave-equation tomography. *Geophysical Journal International*, 222(1):69–85.

Luo, Y., Yang, Y., Xu, Y., Xu, H., Zhao, K., and Wang, K. (2015). On the limitations of interstation distances in ambient noise tomography. *Geophysical Journal International*, 201(2):652–661.

Mangano, G., D'Alessandro, A., and D'Anna, G. (2011). Long term underwater monitoring of seismic areas: Design of an ocean bottom seismometer with hydrophone and its performance evaluation. In *OCEANS 2011 IEEE - Spain*.

Marquart, G. (1991). Interpretations of geoid anomalies around the Iceland hotspot. *Geophysical Journal International*, 106(1):149–160.

Masterlark, T., Haney, M., Dickinson, H., Fournier, T., and Searcy, C. (2010). Rheologic and structural controls on the deformation of Okmok volcano, Alaska: FEMs, InSAR, and ambient noise tomography. *Journal of Geophysical Research*, 115(B2):B02409.

Mindevalli, O. Y. and Mitchell, B. J. (1989). Crustal structure and possible anisotropy in Turkey from seismic surface wave dispersion. *Geophysical Journal International*, 98(1):93–106.

Mitchell, M. A., White, R. S., Roecker, S., and Greenfield, T. (2013). Tomographic image of melt storage beneath Askja Volcano, Iceland using local microseismicity. *Geophysical Research Letters*, 40(19):5040–5046.

Mogi, K. (1958). Relations between the eruptions of various volcanoes and the deformations of the ground surfaces around them. *Earthq Res Inst*, 36:99–134.

Montagner, J. P. (1986). Regional three-dimensional structures using long-period surface waves. *Annales Geophysicae, Series B*, 4(B3):283–294.

Montagner, J.-P. and Nataf, H.-C. (1986). A simple method for inverting the azimuthal anisotropy of surface waves. *Journal of Geophysical Research: Solid Earth*, 91(B1):511–520.

Mordret, A., Rivet, D., Landès, M., and Shapiro, N. M. (2015). Three-dimensional shear velocity anisotropic model of Piton de la Fournaise Volcano (La Réunion Island) from ambient seismic noise. *Journal of Geophysical Research: Solid Earth*, 120(1):406–427.

Morgan, W. J. (1971). Convection plumes in the lower mantle. *Nature*, 230(5288):42–43.

Mottaghi, A. A., Rezapour, M., and Korn, M. (2013). Ambient noise surface wave tomography of the iranian plateau. *Geophysical Journal International*, 193(1):452–462.

Müller, R. D., Sdrolias, M., Gaina, C., and Roest, W. R. (2008). Age, spreading rates, and spreading asymmetry of the world's ocean crust. *Geochemistry, Geophysics, Geosystems*, 9(4).

Nafe, J. E. and Drake, C. L. (1963). Physical properties of marine sediments. In *The Sea*, pages 794–813.

Nicolson, H., Curtis, A., Baptie, B., and Galetti, E. (2012). Seismic interferometry and ambient noise tomography in the British Isles.

Nishida, K., Montagner, J.-P., and Kawakatsu, H. (2009). Global surface wave tomography using seismic hum. *Science*, 326(5949):112–112.

Nishimura, C. E. and Forsyth, D. W. (1989). The anisotropic structure of the upper mantle in the Pacific. *Geophysical Journal International*, 96(2):203–229.

Obermann, A., Lupi, M., Mordret, A., Jakobsdóttir, S. S., and Miller, S. A. (2016). 3D-ambient noise Rayleigh wave tomography of Snæfellsjökull volcano, Iceland. *Journal of Volcanology and Geothermal Research*, 317:42–52.

Pagli, C., Sigmundsson, F., Árnadóttir, T., Einarsson, P., and Sturkell, E. (2006). Deflation of the Askja volcanic system: Constraints on the deformation source from combined inversion of satellite radar interferograms and GPS measurements. *Journal of Volcanology and Geothermal Research*, 152(1-2):97–108.

Pálmason, G. (1971). Crustal structure of Iceland from explosion seismology. *Societas Scientiarum Islandica*, (40):187.

Pepe, S., De Siena, L., Barone, A., Castaldo, R., D'Auria, L., Manzo, M., Casu, F., Fedi, M., Lanari, R., Bianco, F., et al. (2019). Volcanic structures investigation through sar and seismic interferometric methods: The 2011–2013 campi flegrei unrest episode. *Remote Sensing of Environment*, 234:111440.

Pilia, S., Rawlinson, N., Direen, N. G., Reading, A. M., Cayley, R., Pryer, L., Arroucau, P., and Duffett, M. (2015). Linking mainland Australia and Tasmania using ambient seismic noise tomography: Implications for the tectonic evolution of the east Gondwana margin. *Gondwana Research*, 28(3):1212–1227.

Podvin, P. and Lecomte, I. (1991). Finite difference computation of traveltimes in very contrasted velocity models: a massively parallel approach and its associated tools. *Geophysical Journal International*, 105(1):271–284.

Raitt, R. (1963). Seismic refraction studies of the mendocino fracture zone. *Papers, Int. Assoc. Phys. Oceanogr., 13th General Assembly, Berkeley*, 6:71.

Rawlinson, N., Pilia, S., Young, M., Salmon, M., and Yang, Y. (2016). Crust and upper mantle structure beneath southeast Australia from ambient noise and teleseismic tomography. *Tectonophysics*, 689:143–156.

Rawlinson, N., Pozgay, S., and Fishwick, S. (2010). Seismic tomography: a window into deep earth. *Physics of the Earth and Planetary Interiors*, 178(3-4):101–135.

Rawlinson, N. and Sambridge, M. (2005). The fast marching method: an effective tool for tomographic imaging and tracking multiple phases in complex layered media. *Exploration Geophysics*, 36(4):341.

Rhie, J. and Romanowics, B. (2004). Excitation of Earth's continuous free oscillations by atmosphere-ocean- seafloor coupling. *Nature*, 431(7008):552–556.

Rickers, F., Fichtner, A., and Trampert, J. (2013). The Iceland-Jan Mayen plume system and its impact on mantle dynamics in the North Atlantic region: Evidence from full-waveform inversion. *Earth and Planetary Science Letters*, 367:39–51.

Ritzwoller, M. H., Shapiro, N. M., Barmin, M. P., and Levshin, A. L. (2002). Global surface wave diffraction tomography. *Journal of Geophysical Research: Solid Earth*, 107(B12):ESE–4.

Roux, P., Sabra, K. G., Kuperman, W. A., and Roux, A. (2005). Ambient noise cross correlation in free space: Theoretical approach. *The Journal of the Acoustical Society of America*, 117(1):79–84.

Russell, J. B., Gaherty, J. B., Lin, P. Y. P., Lizarralde, D., Collins, J. A., Hirth, G., and Evans, R. L. (2019). High-Resolution Constraints on Pacific Upper Mantle Petrofabric Inferred From Surface-Wave Anisotropy. *Journal of Geophysical Research: Solid Earth*, 124(1):631–657.

Rymer, H. and Tryggvason, E. (1993). Gravity and elevation changes at Askja, Iceland. *Bulletin of Volcanology*, 55(5):362–371.

Sabra, K. G., Gerstoft, P., Roux, P., Kuperman, W. A., and Fehler, M. C. (2005). Extracting time-domain Green's function estimates from ambient seismic noise. *Geophysical Research Letters*, 32(3).

Sager, K., Boehm, C., Ermert, L., Krischer, L., and Fichtner, A. (2020). Global-Scale Full-Waveform Ambient Noise Inversion. *Journal of Geophysical Research: Solid Earth*, 125(4):e2019JB018644.

Satsukawa, T., Ildefonse, B., Mainprice, D., Morales, L. F., Michibayashi, K., and Barou, F. (2013). A database of plagioclase crystal preferred orientations (CPO) and microstructures-implications for CPO origin, strength, symmetry and seismic anisotropy in gabbroic rocks. *Solid Earth*, 4(2):511–542.

Schimmel, M. (1999). Phase cross-correlations: Design, comparisons, and applications. *Bulletin of the Seismological Society of America*, 89(5):1366–1378.

Schimmel, M., Stutzmann, E., and Gallart, J. (2011). Using instantaneous phase coherence for signal extraction from ambient noise data at a local to a global scale. *Geophysical Journal International*, 184(1):494–506.

Schuler, J., Greenfield, T., White, R. S., Roecker, S. W., Brandsdõttir, B., Stock, J. M., Tarasewicz, J., Martens, H. R., and Pugh, D. (2015). Seismic imaging of the shallow crust beneath the Krafla central volcano, NE Iceland. *Journal of Geophysical Research: Solid Earth*, 120(10):7156–7173.

Shapiro, N. M. and Campillo, M. (2004). Emergence of broadband Rayleigh waves from correlations of the ambient seismic noise. *Geophysical Research Letters*, 31(7).

Shapiro, N. M., Campillo, M., Stehly, L., and Ritzwoller, M. H. (2005). High-resolution surface-wave tomography from ambient seismic noise. *Science*, 307(5715):1615–1618.

Shapiro, N. M., Ritzwoller, M. H., and Bensen, G. D. (2006). Surce location of the 26 sec microseism from cross-correlations of ambient seismic noise. *Geophysical Research Letters*, 33(18).

Shearer, P. M. (1988). Cracked media, poisson's ratio and the structure of the upper oceanic crust. *Geophysical Journal International*, 92(2):357–362.

Shor, G. G. and Pollard, D. D. (1964). Mohole site selection studies north of Maui. *Journal of Geophysical Research*, 69(8):1627–1637.

Shorttle, O. and Maclennan, J. (2011). Compositional trends of Icelandic basalts: Implications for short-length scale lithological heterogeneity in mantle plumes. *Geochemistry, Geophysics, Geosystems*, 12(11).

Sigmundsson, F., Hooper, A., Hreinsdóttir, S., Vogfjörd, K. S., Ófeigsson, B. G., Heimisson, E. R., Dumont, S., Parks, M., Spaans, K., Gudmundsson, G. B., Drouin, V., Árnadóttir, T., Jónsdóttir, K., Gudmundsson, M. T., Högnadóttir, T., Fridriksdóttir, H. M., Hensch, M., Einarsson, P., Magnússon, E., Samsonov, S., Brandsdóttir, B., White, R. S., Ágústsdóttir, T., Greenfield, T., Green, R. G., Hjartardóttir, Á. R., Pedersen, R., Bennett, R. A., Geirsson, H., la Femina, P. C., Björnsson, H., Pálsson, F., Sturkell, E., Bean, C. J., Möllhoff, M., Braiden, A. K., and Eibl, E. P. (2015). Segmented lateral dyke growth in a rifting event at Bárðarbunga volcanic system, Iceland. *Nature*, 517(7533):191–195.

Smith, M. L. and Dahlen, F. A. (1973). The azimuthal dependence of Love and Rayleigh wave propagation in a slightly anisotropic medium. *Journal of Geophysical Research*, 78(17):3321–3333.

Spica, Z., Perton, M., and Legrand, D. (2017). Anatomy of the Colima volcano magmatic system, Mexico. *Earth and Planetary Science Letters*, 459:1–13.

Stankiewicz, J., Ryberg, T., Haberland, C., Fauzi, N., and Natawidjaja, D. (2010). Lake Toba volcano magma chamber imaged by ambient seismic noise tomography. *Geophysical Research Letters*, 37(17).

Staples, R. K., White, R. S., Brandsdóttir, B., Menke, W., Maguire, P. K. H., and McBride, J. H. (1997). Färoe-Iceland Ridge Experiment 1. Crustal structure of northeastern Iceland. *Journal of Geophysical Research: Solid Earth*, 102(B4):7849–7866.

Stephen, R. (1981). Seismic anisotropy observed in upper oceanic crust. *Geophysical Research Letters*, 8(8):865–868.

Sturkell, E. and Sigmundsson, F. (2000). Continuous deflation of the askja caldera, iceland, during the 1983–1998 noneruptive period. *Journal of Geophysical Research: Solid Earth*, 105(B11):25671–25684.

Sturkell, E., Sigmundsson, F., and Slunga, R. (2006). 1983-2003 decaying rate of deflation at Askja caldera: Pressure decrease in an extensive magma plumbing system at a spreading plate boundary. *Bulletin of Volcanology*, 68(7-8):727–735.

Syracuse, E. M., Maceira, M., Zhang, H., and Thurber, C. H. (2015). Seismicity and structure of Akutan and Makushin Volcanoes, Alaska, using joint body and surface wave tomography. *Journal of Geophysical Research: Solid Earth*, 120(2):1036–1052.

Ventosa, S., Schimmel, M., and Stutzmann, E. (2017). Extracting surface waves, hum and normal modes: time-scale phase-weighted stack and beyond. *Geophysical Journal International*, 211(1):30–44.

Ventosa, S., Schimmel, M., and Stutzmann, E. (2019). Towards the processing of large data volumes with phase cross-correlation. *Seismological Research Letters*, 90(4):1663–1669.

Weaver, R. L. and Lobkis, O. I. (2004). Diffuse fields in open systems and the emergence of the Green's function (L). *The Journal of the Acoustical Society of America*, 116(5):2731–2734.

White, R. and McKenzie, D. (1989). Magmatism at rift zones: the generation of volcanic continental margins and flood basalts. *Journal of Geophysical Research*, 94(B6):7685–7729.

White, R. and Whitmarsh, R. (1984). An investigation of seismic anisotropy due to cracks in the upper oceanic crust at 45 n, mid-atlantic ridge. *Geophysical Journal International*, 79(2):439–467.

White, R. S., Drew, J., Martens, H. R., Key, J., Soosalu, H., and Jakobsdóttir, S. S. (2011). Dynamics of dyke intrusion in the mid-crust of Iceland. *Earth and Planetary Science Letters*, 304(3-4):300–312.

White, R. S., McKenzie, D., and O'Nions, R. K. (1992). Oceanic crustal thickness from seismic measurements and rare earth element inversions. *Journal of Geophysical Research*, 97(B13):19683–19715.

Wolfe, C. J. (2002). Assessing the depth resolution of tomographic models of upper mantle structure beneath Iceland. *Geophysical Research Letters*, 29(2):1–4.

Wolfe, C. J., Th. Bjarnason, I., VanDecar, J. C., and Solomon, S. C. (1997). Seismic structure of the Iceland mantle plume. *Nature*, 385(6613):245–247.

Wüstefeld, A., Bokelmann, G., Barruol, G., and Montagner, J.-P. (2009). Identifying global seismic anisotropy patterns by correlating shear-wave splitting and surface-wave data. *Physics of the Earth and Planetary Interiors*, 176(3-4):198–212.

Xie, J., Zeng, X., Chen, W., and Zhan, Z. (2011). Comparison of ground truth location of earthquake from insar and from ambient seismic noise: A case study of the 1998 zhangbei earthquake. *Earthquake science*, 24(2):239–247.

Yao, H. and van der Hilst, R. D. (2009). Analysis of ambient noise energy distribution and phase velocity bias in ambient noise tomography, with application to SE Tibet. *Geophysical Journal International*, 179(2):1113–1132.

Yao, H., van der Hilst, R. D., and de Hoop, M. V. (2006). Surface-wave array tomography in SE Tibet from ambient seismic noise and two-station analysis - I. Phase velocity maps. *Geophysical Journal International*, 166(2):732–744.

Zhang, X., Curtis, A., Galetti, E., and de Ridder, S. (2018). 3-DMonte Carlo surface wave tomography. *Geophysical Journal International*, 215(3):1644–1658.

Zhang, X., Hansteen, F., Curtis, A., and de Ridder, S. (2020). 1-d, 2-d, and 3-d monte carlo ambient noise tomography using a dense passive seismic array installed on the north sea seabed. *Journal of Geophysical Research: Solid Earth*, 125(2):e2019JB018552.

Appendix A

Average Velocity models and dispersion curves

In this appendix I provide the resulting 1D V_{SV} and V_{SH} average velocity models, as well as the average dispersion curves, for Iceland (Chapter 3) and for the Askja region (Chapter 4) of Love and Rayleigh waves from both chapters for the use of future works. The full dataset of noise cross correlations is available at https://figshare.com/s/231cc8a7f72189a9d5f7.

A.1 Iceland

A.1.1 Velocity models

The average velocity models from Fig 3.5 are displayed in the following table

Depth km	V_{SV} km/s	V_{SH} km/s
0 - 5	3.26	2.98
5 - 10	3.35	3.29
10 - 15	3.48	3.69
15 - 20	3.65	3.97
20 - 25	3.8	4.11
25 - 30	3.91	4.16
30 - 35	3.98	4.15
35 - 40	4.01	4.12

A.1.2 Average dispersion curves

The average phase dispersion curves from Fig 3.5 are displayed in the following table

Period s	C_R km/s	C_L km/s
8	3.19	3.41
9	3.22	3.45
10	3.24	3.52
11	3.27	3.56
12	3.29	3.6
13	3.32	3.66
14	3.36	3.69
15	3.39	3.74
16	3.42	3.78
17	3.45	3.81
18	3.48	3.84
19	3.5	3.87
20	3.52	3.89
21	3.54	3.91
22	3.55	3.93
23	3.57	3.94
24	3.57	3.96
25	3.59	3.98
26	3.61	4.0
27	3.63	4.01
28	3.63	4.02
29	3.65	4.04
30	3.66	4.05

A.2 Askja

A.2.1 Velocity models

The average velocity models from Fig 4.5 are displayed in the following table

Depth km	V_{SV} km/s	V_{SH} km/s
-0.8 - 0.0	2.63	2.04
0.0 - 1.0	2.76	2.24
1.0 - 2.0	2.9	2.54
2.0 - 3.0	3.06	2.93
3.0 - 4.0	3.18	3.25
4.0 - 5.0	3.25	3.39
5.0 - 6.0	3.45	3.56

A.2.2 Average dispersion curves

The average group dispersion curves from Fig 4.5 are displayed in the following table

Period s	U_R km/s	U_L km/s
2.0	2.37	1.98
2.5	2.42	1.99
3.0	2.44	2.01
3.5	2.42	2.06
4.0	2.43	2.11
4.5	2.44	2.19
5.0	2.5	2.24
5.5	2.58	2.28
6.0	2.66	2.34
6.5	2.76	2.4
7.0	2.85	2.48
8.0		2.65
9.0		2.85

Appendix B

Supplementary Figures

B.1 Supplementary Figures Chapter 3

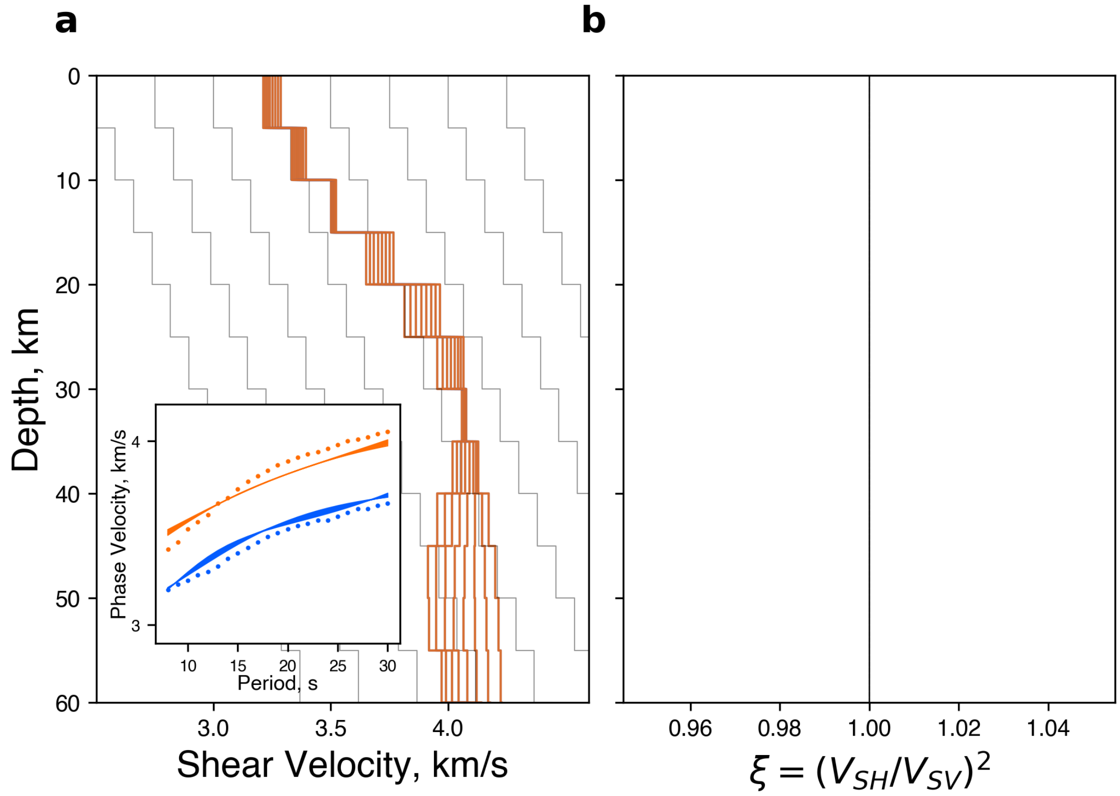

Fig. B.1 Same as 3.5 but assuming $V_{SV} = V_{SH} (\xi = 1)$ and trying to fit both Love and Rayleigh dispersion using a single isotropic 1D model.

B.2 Supplementary Figures Chapter 4

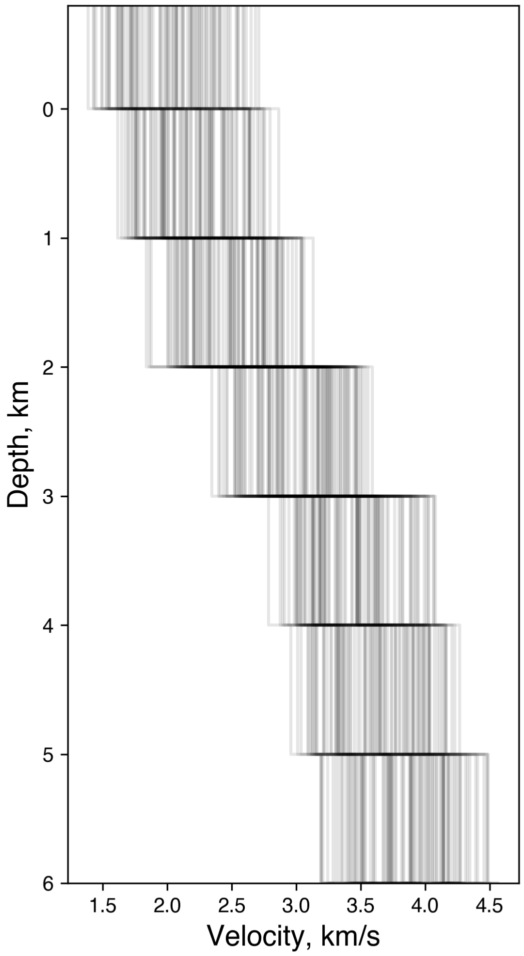

Fig. B.2 The ensemble of starting models used for the 1D inversion in Chapter 4

B.2.1 Vertical cross sections through the pseudo 3D shear velocity model

In chapter 4 we have presented horizontal cross sections through our pseudo 3D shear velocity models together with the lateral location of a modelled magma body. Vertical cross sections through the same models are shown in Fig B.3. In the middle row, where velocities are plotted as absolute values, no slow velocity feature can be seen at the depth of modelled magma

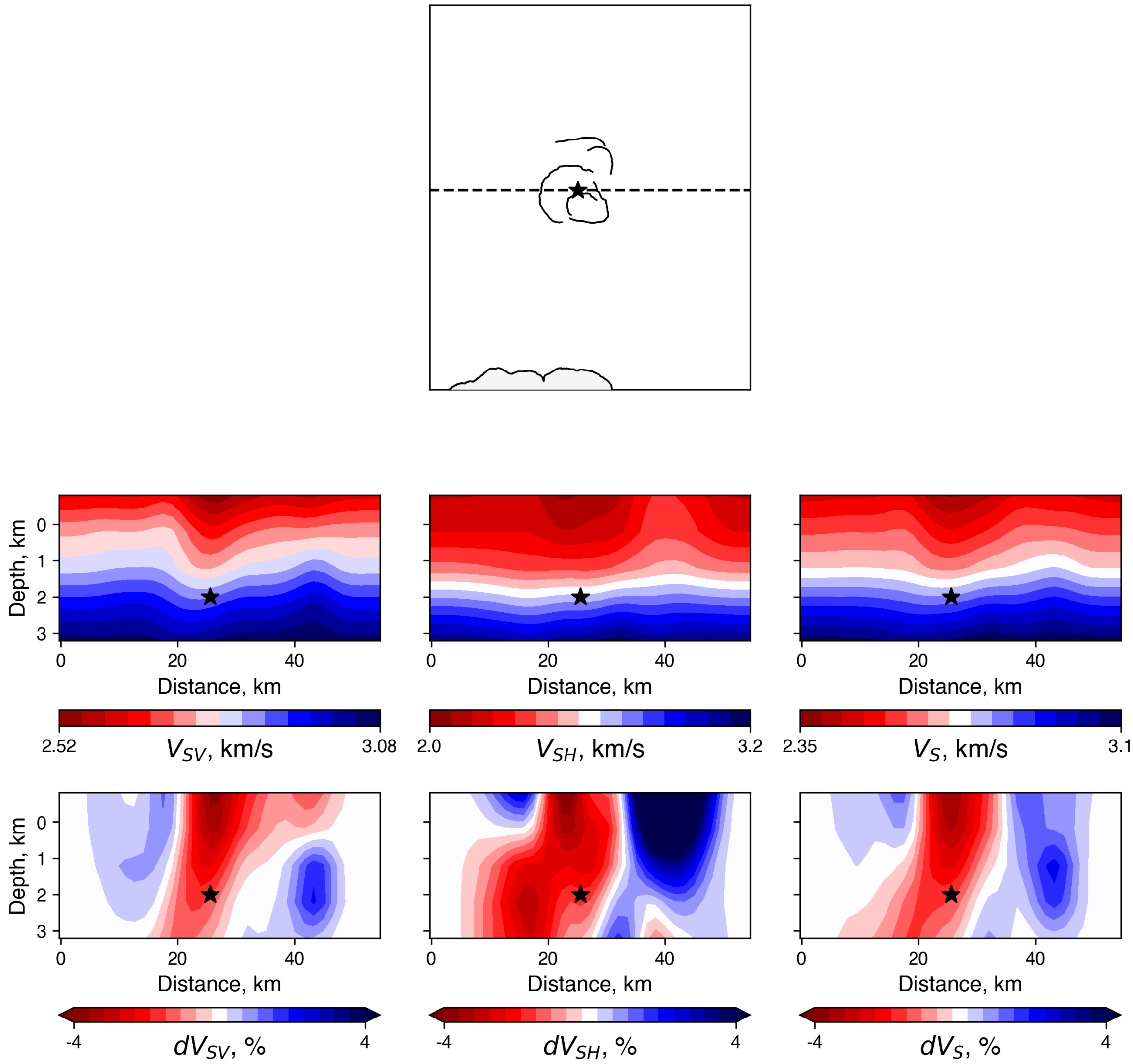

Fig. B.3 Vertical cross sections through the pseudo 3D shear velocity model shown in Fig. 4.13. The top panel displays a map with the location of the cross section denoted using a dashed line. The centre of the modelled deflating body from De Zeeuw-van Dalfsen et al. (2012) is denoted as a black star. The middle row displays cross sections through the V_{SV}, V_{SH} and V_S models coloured as absolute value. the bottom row displays the same cross sections coloured as percent perturbation to the mean of the ensemble of starting models at each depth.

body (black star). In the bottom row, where velocities are plotted as percent perturbation, the V_{SH} model displays a slow anomaly at the same approximate depth as the modelled magma body, but centred 10 km to the west. The V_{SV} model does not display this feature but rather a vertically smooth slow velocity anomaly under the caldera, which appears to be shifting west with increasing depth. In all models, the slowest velocities can be found at the surface directly under the caldera. As mentioned in the main text, surface waves naturally smear vertical structure and we therefore remain cautions about interpreting these cross sections.

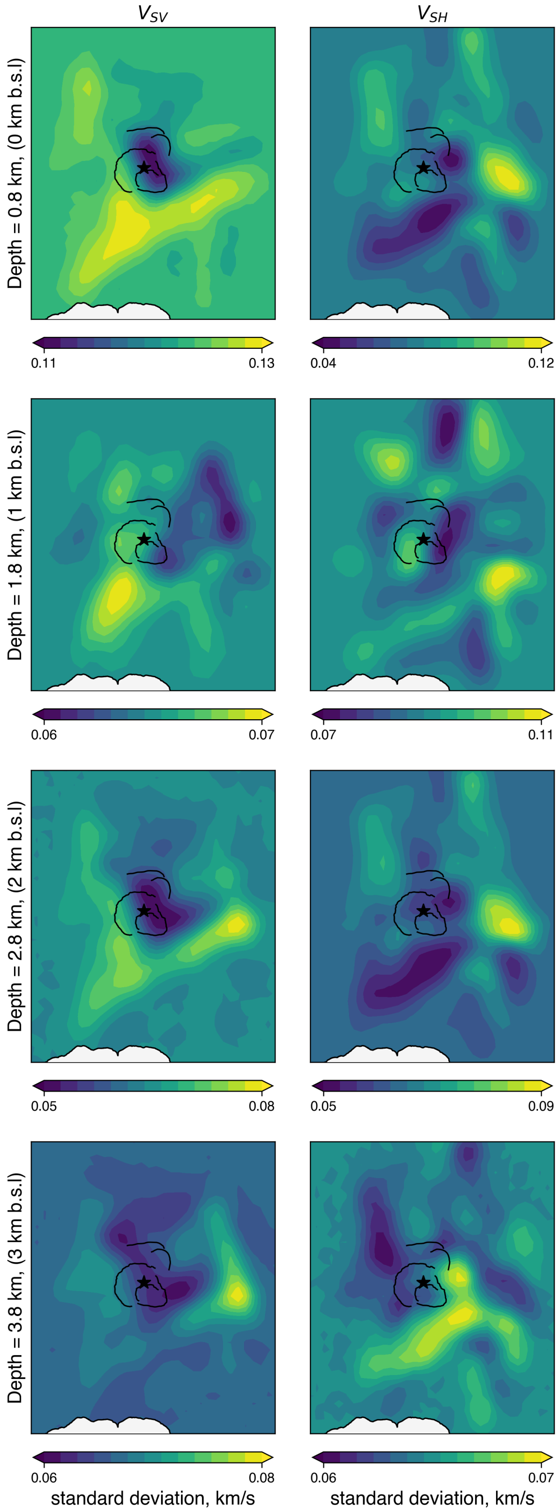

Fig. B.4 Estimated errors for the pseudo 3D V_{SV} and V_{SH} shown in Fig. 4.13. The 1D inversion is repeated 100 times using different starting models and the standard deviation of the results is used to estimate model uncertainty.